Time-lapse microscopy study of noise in development

Gritti, Nicola

DOI
10.4233/uuid:23580f57-9ed1-4fa3-95ad-b8fe7cc8ba05

Publication date
2017

Document Version
Final published version

Citation (APA)
Gritti, N. (2017). *Time-lapse microscopy study of noise in development*. [Dissertation (TU Delft), Delft University of Technology]. https://doi.org/10.4233/uuid:23580f57-9ed1-4fa3-95ad-b8fe7cc8ba05

Time-lapse microscopy study of noise in development

Nicola Gritti

Time-lapse microscopy study of noise in development

Nicola Gritti

TIME-LAPSE MICROSCOPY STUDY OF NOISE IN DEVELOPMENT

Nicola Gritti

PhD Thesis, Technische Universiteit Delft, 13 april 2017
Time-lapse microscopy study of noise in development
Nicola GRITTI

ISBN 978-94-92323-13-2

A digital version of this thesis can be downloaded from http://www.amolf.nl.

TIME-LAPSE MICROSCOPY STUDY OF NOISE IN DEVELOPMENT

PROEFSCHRIFT

ter verkrijging van de graad van doctor
aan de Technische Universiteit Delft,
op gezag van de Rector Magnificus prof. ir. K.C.A.M. Luyben;
voorzitter van het College voor Promoties,
in het openbaar te verdedigen op
donderdag, 13 april 2017 om 12:30 uur

door

Nicola GRITTI

Laurea Magistrale in Fisica
Università degli Studi di Milano-Bicocca, Italië
geboren te Ponte San Pietro, Italië

This dissertation has been approved by the

Promotor:	Prof. dr. ir. S. J. Tans	Technische Universiteit Delft FOM Institute AMOLF
Copromotor:	Dr. J. S. van Zon	FOM Institute AMOLF

Composition of the doctoral committee:

Rector Magnificus	Chairperson
Prof. dr. ir. S. J. Tans	Promotor
Dr. J. S. van Zon	Copromotor

Independent members:

Prof. dr. M. Dogterom	Technische Universiteit Delft
Prof. dr. S. J. L. van den Heuvel	Utrecht University
Prof. dr. ir. E. J. G. Peterman	Vrije Universiteit Amsterdam
Dr. H. O. Youk	Technische Universiteit Delft
Dr. M. Barkoulas	Imperial College, London, United Kingdom
Prof. dr. N. H. Dekker	Technische Universiteit Delft, reserve member

The work described in this thesis is part of the research program of the
Stichting voor Fundamenteel Onderzoek der Materie (FOM)
which is financially supported by the
Nederlandse Organisatie voor Wetenschappelijke Onderzoek (NWO).

This work was carried out at the
FOM Institute AMOLF
Amsterdam
where a limited number of copies of this dissertation is available.

Contents

1

Introduction

The concept of randomness and chance has intrigued human beings since the oldest times. In ancient history, it was thought that events are affected by the choices of the gods, who then were responsible for the variability detected in nature. During the 3rd century BC, however, Greek philosophers argued that randomness has a more natural essence. Democritus, for instance, believed that it is closely related to ignorance. Any unexpected result has a plausible explanation, therefore randomness is due to the inability of humans to fully understand the nature of events [1]. On the other hand, Epicurus suggested that Nature itself is continuously affected by random events at the smallest atomic scales and is therefore intrinsically unpredictable [2].

Since these pioneering works, the concept of randomness has been forgotten for several centuries, in an era in which philosophers were mostly focused on finding a higher meaning to the human lives and struggles. However, by the end of the 18th century, many revolutionary discoveries led to the establishment of classical mechanics, which seemed to suggest that Nature is governed by deterministic laws. Therefore, it was thought that natural events can be predicted upon full knowledge of the initial conditions of the system.

It was only in the late 19th century that findings in electrodynamics and thermodynamics undermined this believe. Since then, many scientific fields, including but not limited to quantum mechanics, statistical physics and particle physics, developed that describe natural events as stochastic, probabilistic and affected by noise. The idea of Epicurus became again widely accepted: natural events are variable, not predictable and partially driven by random events. Since then, the concepts of randomness and noise have played a central role in many disciplines in science, such as mathematics, physics, chemistry, statistics and, last but not least, biology. In this thesis, we aim to contribute to the understanding of the origins, the roles and the effects of noise in biology.

1.1 The role of randomness in biology

Although there are several hypothesis on how life arose on our planet [3], it is widely accepted that the oldest form of life on Earth is at least 4 billion years old [4]. As Darwin hypothesized in 1859 [5], it has been recently found that all living organisms on Earth descend from a universal common ancestor that lived at least 3.5 billion years ago [6]. Such primitive forms of life were very different from the organisms that populate our planet nowadays, as they were often anaerobic, thus did not require presence of oxygen to survive. Instead, they relied on simple chemical reactions to perform nitrogen and carbon dioxide fixation to extract energy. Nevertheless, it has been recently established that part of the biological machinery that keeps all current living organisms alive is relatively similar to that of the primitive organisms populating Earth billion years ago [6].

Even if all living organisms share some traits with their primitive common ancestor, over the course of 4 billion years life has evolved in a wide variety of forms, from sub-micrometer sized bacteria to the honey fungus that stretches over 2.4 km in the Blue Mountains in Oregon. It is estimated that more than one trillion species live on Earth, and that we have only been able to describe 1.2 millions of them, which is a mere 0.0001% [7, 8].

It may not seem surprising that life on our planet shows such a huge variety. After all, over the last 4 billion years, several more or less catastrophic events have happened that forced living organisms to evolve and adapt in order to survive, sometimes causing massive extinctions. Natural selection has worked over billion years to privilege the fittest species and extinguish species that were not able to cope with the ever-changing environment and the predators surrounding them. However, it is surprising the extent at which each of these organisms have been able to optimize their biology to the ecosystem and make the most out of the resources that the surrounding provided them. Each of the living organisms populating our planet can be seen as an almost perfect machine that receives inputs from the surrounding environment and reacts accordingly through a complicated internal machinery. Ultimately, this is what makes bacteria move towards food and antelopes run away from lions.

During the last century, biologists have worked hard trying to elucidate the complex mechanisms that allow all living organisms to survive. Probably the major advances in this respect are the discovery and description of deoxyribuncleic acid (DNA) as carrier of all the genetic information [9, 10] and the definition of the central dogma of molecular biology [11]. DNA is a molecule organized in a double helix structure and contained in every single cell. Each helix is a sequence of single monomers that can occur in four chemically different nucleotides. The combination of such nucleotides defines the genetic information specific to a particular organism. DNA molecules can be contained freely inside the cell wall, in which case we talk about prokaryotic cells, or can be enclosed in a sub-cellular structure, the nucleus, in which case we talk about eukaryotic cells. In most eukaryotic cells, the genetic

information is spread over different substructures called chromosomes. All multicellular organisms consists of such eukaryotic cells.

Despite the differences in its large-scale organization, DNA always contains all the instructions needed to perform the complex biological functions necessary to survive. Such instructions are encoded on the DNA, in the form of genes. The question of how this genetic information is translated into molecules able to perform complex functions is explained by the central dogma of molecular biology. As an approximate and brief version of it, the central dogma of molecular biology states that a single cell is able to replicate its own DNA entirely, translate parts of it into messenger ribonucleic acid (mRNA), and transcribe mRNAs into proteins. While replication of DNA is necessary for reproduction of the cell, the final products of this complex machinery are proteins, highly specialized molecules that are able to perform different tasks. Often multiple proteins combine to create a macromolecule able to perform a complicated task. For example, ribonucleic acid polymerase (RNAp) can bind to a particular site on the DNA and transcribe the gene found downstream into an mRNA. An even more complex molecule is the ribosome, the machine necessary to translate mRNAs into proteins. Many more proteins exists and each of them has a specific functional role in the survival of a cell.

During their entire life, cells need to perform many different tasks, each of them requiring the production of the corresponding proteins. It is therefore evident that not all the proteins must be produced at equal levels. A complex mechanism is exploited to regulate the production of proteins. At the earliest stage, *gene expression* can be tuned in order to produce more or less mRNAs. For instance, some molecules, called *transcription factors*, bind on specific parts of DNA, called *promoters*, to stimulate or inhibit binding of RNAp and therefore regulate the expression of the gene downstream on the DNA. Secondary, *translational regulation* can be used to suppress production of proteins. For instance, single mRNA molecules can be actively degraded.

1.1.1 Cell biology and thermal fluctuations

Considering the discovery of the central dogma of molecular biology and the theory of natural selection, it is natural to assume that all observable variability among living organisms can be fully explained by genetic and/or environmental variability. However, a third element is formed by stochastic variability, which causes random variations even in two genetically identical individuals exposed to exactly the same environmental conditions. To understand the origin of this source of variability, we need to give a closer look to the building blocks of life. The typical dimension of a cell is on the order of a few micrometers, while proteins size is on the nanometers scale. At these scales, thermal fluctuations are omnipresent and have a major effect on the molecular dynamics. Individual molecules move inside the cell by Brownian motion, and the chemical reactions that trigger the basic biological processes happen only when two or more components come into contact. That is the reason why

biochemical processes are *probabilistic*. For instance, one can never predict when a single RNAp will bind to the promoter of a certain gene, but can only estimate a binding rate: the *probability* that this event will happen within a certain amount of time.

Thermal fluctuations are largely ignored when studying a macroscopic system because the number of molecules involved is so large that fluctuations are eventually averaged out. Therefore, a fully deterministic description of macroscopic systems is possible. However, certain molecules are present in the cell with as few as 10-100 copies. When dealing with such low numbers, molecular fluctuations, often referred to as *noise*, cannot be simply averaged out, and the slightest deviation in the motion of a single transcription factor can have a significant effect on the expression level of its target gene. It is therefore easy to imagine that molecular fluctuations have a major impact on many cellular processes such as gene expression, cell signaling and motility.

1.1.2 Gene expression noise

Historically, the first biological process in which stochasticity has been acknowledged is gene expression. Even though stochasticity in gene expression had been previously observed [12, 13], it was not until the late 1990s that scientists started to recognize that gene expression is indeed strongly stochastic [14]. After this preliminary work, many researchers started looking for more experimental evidence of such phenomenon.

In one of the first studies showing stochastic gene expression [16], a synthetic biology approach was used. The authors engineered a *repressilator*: a genetic circuit consisting of three different genes that was designed to generate gene expression oscillations. The network was designed in a circular fashion: each gene expresses a transcription factor able to repress the expression of the consecutive gene in the loop. The authors placed all genes in a plasmid, a small DNA molecule, and inserted it in *E. coli* bacteria. The expected result of such a circular negative feedback loop is an oscillatory system, with expression of each gene cyclically activated over the course of several hours. By tagging one of the genes with the green fluorescent protein (GFP), the authors were able to follow the dynamics of one of the three genes over time and confirm the predicted oscillatory dynamics. Besides showing the power of synthetic biology, with which it is possible to study gene regulatory networks, they reported a noisy behavior of the fluctuations. In particular, they found considerable cell-cell variability both in the amplitude and the period of the oscillations. The authors suggested that such noisy behavior could possibly be explained by stochastic fluctuations of the components of the system.

Shortly after that, two milestone studies explored the causes of stochastic gene expression. In the first study, the concepts of *intrinsic* and *extrinsic* variability were formulated for the first time [15]. The authors inserted two copies of the same promoter in *E. coli* bacteria expressing two different fluorescent proteins (CFP and

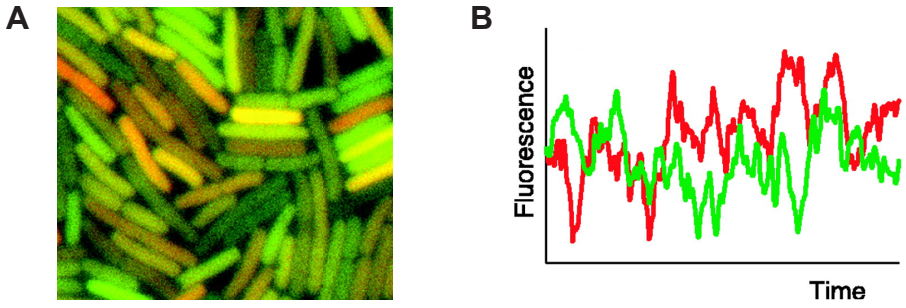

Figure 1.1: Gene expression fluctuations. (**A**) Expression of CFP (green) and YFP (red) in a population of genetically identical *E. coli*. (**B**) Schematic of the time series of CFP (green) and YFP (red) expression levels in a single cell in case of significant intrinsic noise. Figures were taken from [15].

YFP). Fluorescence intensity from bacteria belonging to the same colony was then recorded with dual color time-lapse fluorescence microscopy (Fig. 1.1). Following their description of intrinsic and extrinsic variability, extrinsic fluctuations due to the variability in the abundance of RNAp and ribosomes affect both promoters equally. On the other hand, intrinsic fluctuations due to the stochastic nature of gene expression affects each promoter independently. Therefore, if no intrinsic stochasticity is present, promoter activities in the same cell should perfectly correlate. However, the authors found that the amount of CFP and YFP in the same cell was highly variable, which then resulted in high cell-to-cell variability in the expression of both CFP and YFP (represented as cells with different red (YFP) and green (CFP) intensities in Fig. 1.1A). This shows that both sources of noise are significant, and that the impact of intrinsic variability on a single gene expression is as high as its extrinsic variability. In the second study, evidence arose that intrinsic variability is present also in eukaryotic cells [17], although it has a smaller effect. The authors suggested that this could be due to the larger amount of molecules present in eukaryotic cells, supporting the hypothesis that molecular fluctuations are more relevant when a low number of molecules is involved.

Following the work on gene expression noise, researchers started to intensively study the protein production process as a whole, starting from the expression of the gene to the translation of the mRNA. First, it was observed that the rate of transcription of a gene is not constant, but instead it is often activated in a transient way. This phenomenon is called *transcriptional bursts*, and has been observed both in bacterial and eukaryotic cells [18, 19]. Transcriptional bursts are likely due to a number of different factors. For instance, in eukaryotic cells, the structure of chromosomes is changing constantly, allowing transcription of a gene only when that part of the chromosome is in an open state. In prokaryotic cells, the sources of transcriptional bursts are most likely due to fluctuations in RNAp abundance and

error-correction mechanisms resulting in pauses in the synthesis of mRNAs [20, 21]. Similarly, *translational bursts* were observed [22]. In particular, it was shown that the translational rate is not constant over time, but instead it follows a series of stochastic bursts. This is due to the low number of mRNA molecules and to the fact that a large amount of proteins is produced by a single mRNA before it starts being degraded.

1.1.3 Noise in cellular decision-making

Despite the advances that such models and experiments represent in understanding the dynamics of gene expression, the question remains whether such stochasticity can impact the state and behavior of an entire cell.

As mentioned above, transcription factors regulate the expression of target genes. However, transcription factors themselves are proteins produced via the expression of other genes, which in turn are regulated by different transcription factors. As a consequence, the cell consists of a deeply interconnected *gene regulatory network* (GRN). Within the cell, multiple genes produce the right set of proteins necessary to process input signals and trigger cellular responses. When the network has a particular architecture, small changes in the input can result in massively different responses on the level of the entire cell. Such GRNs are called *genetic switches*.

A classical example of a genetic switch is the λ switch [23]. When the λ bacteriophage, a well-studied virus, infects an *E. coli* bacterium, the viral DNA is typically inserted into the host and starts being replicated together with the bacterial DNA without causing any damage. This state is called the *lysogenic* state. However, the system can also exist in a different state, called the *lytic* state. When the lytic state is triggered, the viral DNA is massively transcribed and hundreds of viruses are synthesized, causing the lysis of the host and allowing the viruses to escape and hunt for another host. The cellular state is light-sensitive: small doses of UV light cause transient upregulation of the expression of a gene, which in turns activates itself in a positive feedback loop and finally results in the induction of the lytic state. This was one of the first examples in which small changes in the input can cause a dramatic effect on the response of an entire cell.

In the previous example different cellular responses are triggered by subtle changes in the input of the GRN. However, intrinsically stochastic switches, i.e. cellular responses that are triggered randomly and are affected by stochastic fluctuations at the gene expression level, also play an important role in biology.

A well-known example of a stochastic switch is found in the soil bacterium *Bacillus subtilis*. When a population of genetically identical *B. subtilis* is exposed to unfavorable environmental conditions, such as starvation, each cell can assume a number of different fates. Some cells decide to lyse and release their genetic material, which can be used by the other cells as food source, therefore increasing the chances of population survival [25]. Other cells develop into spores, a dormant, non-growing and highly resistant state. As soon as environmental conditions improve, the

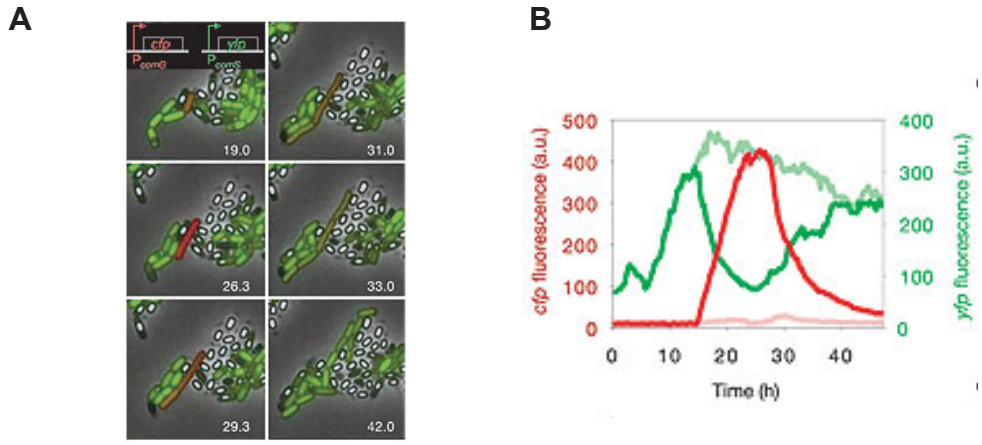

Figure 1.2: Gene expression dynamics during the competence decision in *B. subtilis*. (**A**) Frames from a video of a competence event. A single cell that stochastically enters the competent state expresses CFP (red). Other cells express YFP (green). White cells developed into spores. (**B**) Time-series of both gene expression levels for a cell assuming competence fate (green and red lines) and a cell that did not (faint lines). Figures were taken from [24].

sporulation state is terminated and cells recover their normal growing behavior [26]. Another particular cell fate is *competence*, i.e. the ability to take up extracellular DNA released by lysing cells [24]. External DNA could be used as food source or might be integrated into the genome to try to adapt to the unfavorable conditions [27]. The mechanism driving the competence decision have been extensively studied. First it was shown that the decision to assume the competent fate is governed by a complex gene regulatory network exploiting positive and negative feedback loops, in which a major role is played by a gene called *comK* (Fig. 1.2A) [24, 28]. Next, it was shown that *comK* expression is intrinsically stochastic, and that such stochasticity drives the cell decision, in that large enough fluctuations are amplified by a positive feedback loop and result in the switch of the cell to the competent fate (Fig. 1.2B) [29]. Competence decisions are therefore intrinsically stochastic.

These results represent important evidence showing how noise at the gene expression level can greatly affect the state of an entire cell. Moreover, they show how noise can be beneficial for the survival of a population in an unpredictable environment.

These examples show that noise at the gene expression level can affect gene regulation in bacterial cells. These phenomena can have effects in decision-making processes, leading to stochastic responses of individual cells to the same environmental inputs. It is therefore natural to ask whether such stochasticity also affects the biology of multi-cellular organisms, particularly in the case of multi-cellular development. Intriguingly, significantly different phenotypic traits are commonly found between genetically identical multicellular organisms. For instance, even

identical human twins have different fingerprints and different risks of contracting diseases such as rheumatoid arthritis [30]. In the next section I will discuss recent studies on the role of noise in the biology of multi-cellular organisms.

1.2 Noise in developmental biology

Multi-cellular organisms development is a remarkably reliable and complex program during which, starting from a single-celled embryo, cell divisions and differentiation give rise to a fully developed adult capable of reproduction. During development, cells need to tightly control their positions and coordinate their behavior to be in the right place at the right time to perform their functions in the organism.

However, as we have discussed in the previous section, the most basic biological processes are intrinsically stochastic. All cells of a multi-cellular organism are likely subject to the same sources of stochasticity as for unicellular organisms. However, in contrast to unicellular organisms, in multi-cellular organisms a small number of cells can affect the behavior of several surrounding cells, for instance via cell-cell communication. For this reason, noise at the single cell level can have dramatic consequences for the entire organism.

The fact that such serious mistakes are extremely rare suggests that multi-cellular organisms have developed complex control mechanisms to reliably progress through development [31]. The ability of multi-cellular organisms to reliably develop despite noise is called *robustness*. The intrinsic conflict between stochasticity and developmental robustness raises the fundamental question of how noise is suppressed. In this section, I will discuss examples in which noise is detrimental and needs to be suppressed in order to ensure the correct development of the organism. Even though development is largely robust to noise, interestingly examples exist in which noise might not be detrimental but instead is thought to drive development. In this section, I will also discuss such examples. At the end, I will highlight the fundamental questions that need to be addressed in order to have a deep understanding of the role of stochasticity in developmental biology.

1.2.1 Robustness to developmental noise

Examples that have been extensively studied exist in which multi-cellular organisms have developed complex control mechanisms to suppress noise in order to reliably progress through development.

A classical example in which noise suppression mechanisms are exploited is the morphogenesis of the fruit fly *Drosophila melanogaster* embryos [34]. Morphogenesis is the process by which an organized spatial distribution of cells is generated during embryonic development. During early embryogenesis of *D. melanogaster*, a morphogen protein called Bicoid is produced at the anterior pole, and diffuses into the embryo, thereby generating an exponentially decaying concentration gradient

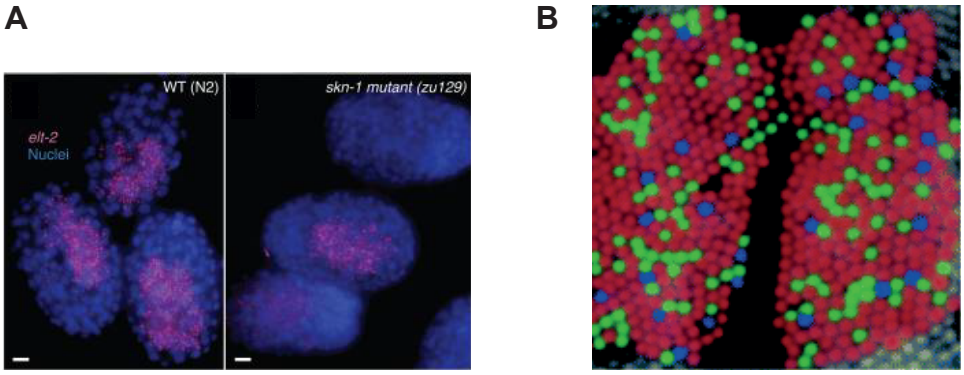

Figure 1.3: Stochasticity in developmental processes. (**A**) Expression of the final target gene responsible for intenstinal cell fate in wild-type (left) and mutant (right) animals. Figure taken from [32] (**B**) Cone cell in a human retina color-coded according to the photopigment chosen (red, green and blue). Figure taken from [33].

along the anteroposterior axis, with a characteristic length of about 100 µm. In order to generate the correct spatial pattern, single cells reliably detect their relative position along the gradient by measuring the local Bicoid concentration. Among other genes, Bicoid triggers the expression of *hunchback*, which then controls the expression of crucial downstream genes. The spatial profile of Hunchback (Hb) is strongly non-linear, with a steep drop in the middle of the embryo. Despite the noise in the Bicoid concentration, the authors found that the Hb profile had extremely low noise levels and that the position of the drop was remarkably precise. This suggests that stochastic cellular decisions due to intrinsic fluctuations are strongly suppressed. In particular, the authors suggested that neighboring cells are able to communicate in order to accurately estimate the Bicoid concentration.

The previous example suggests that gene expression noise and stochastic cell decisions are strongly suppressed during development of multi-cellular organisms. What happens when the fluctuations are not controlled and noise suppression fails? Already in 1925 researchers observed that some genetic mutations in the fruit fly *Drosophila fimebris* result in variable outcomes, with a fraction of individuals showing a wild-type phenotype, while the other part of the population shows a mutant phenotype [35, 36]. Recent studies examined the mechanistic origins of this phenomenon, called *incomplete penetrance*, in the intestinal cell fate specification of the nematode worm *Caenorhabditis elegans* [32]. The intestinal cell fate specification in *C. elegans* is regulated by a simple genetic circuit. By creating a mutant in which a key transcription factor was not expressed, the authors showed that the expression pattern of intermediate genes became highly variable and that the final target gene responsible for the cell fate specification assumed a bimodal distribution (Fig. 1.3A). These results show that the architecture of the GRN underlying intestinal induction is optimized to suppress noise and ensure proper cell specification.

These examples show that mechanisms exist to strongly suppress gene expression noise, leading to highly robust development of multi-cellular organisms.

1.2.2 Stochastic cell fate decisions

Although the robustness of developmental processes is often achieved by suppressing stochasticity, interesting examples exist that show how stochastic gene expression can actually be exploited to perform a specific developmental program. Often these mechanisms result in *stochastic cell fate decisions*, a process in which a cell differentiates in a random manner, by choosing one cell fate out of a repertoire of different fates [37].

One example of stochastic cell fate decisions is the photoreceptor selection in primates [33, 38]. Each of the 4 million cone cells in the human retina, for instance, chooses one type of photoreceptor out of three possible choices: red, green and blue, in what appears to be a random, cell-autonomous decision. The result is a random pattern of cell fates in the retina (Fig. 1.3B). Another example of cell-autonomous cell fate decision is olfactory receptor selection in mice [39]. In this much more complicated system, each olfactory neuron randomly expresses one gene out of ~1300 possible genes, exploiting a stochastic mechanism similar to the cone cells specification in the human retina.

Interestingly, some stochastic cell fate decisions also involve cell-cell communication. In these cases, the stochastic process in one cell impacts that in the neighboring cells, and vice versa. For instance, in the fruit fly *D. melanogaster*, neuronal cells exploit signaling and feedback mechanisms to specify their fate [40]. This cell-cell interaction process results in a mutually exclusive and highly reliable cell fate assignment: when one particular cell randomly assumes a neuronal fate, all neighboring cells become epidermal cells.

These examples suggest that random fluctuations at the gene expression level are not detrimental, but instead can be exploited to drive development.

Taken together, these results suggest that multi-cellular organisms are subject to molecular fluctuations and that they have developed different mechanisms to reach robustness. In some cases, noise is efficiently suppressed, making the outcome of the developmental process almost deterministic. In other cases, organisms exploit noise to reach a variable but robust developmental outcome.

The intrinsic stochastic nature of the molecular players involved in the regulatory network underlying developmental processes raises a number of fundamental questions:

- What are the sources of noise that impact development? How strong are their fluctuations?
- How can such fluctuations be suppressed in deterministic developmental processes to achieve a robust outcome?

- Do developmental processes exist that rely on and are driven by molecular noise? If so, how are molecular fluctuations amplified to impact the behavior of entire cells in the developing organism?

While a molecular biology approach will reveal the key components of the underlying regulatory network, the intrinsic fluctuations at the molecular level require a quantitative approach in order to address these questions. Moreover, to study a process as highly dynamic as development, an approach is needed to follow developmental processes over time. To this end, one needs to follow developing organisms with enough spatial and temporal resolution to detect the dynamics of the process at the single-cell level. However, most of the model systems for multi-cellular organisms, such as fruit flies, zebrafish and mice, have a large body size and a relatively slow development. Therefore, there are currently no techniques able to follow their development with enough spatial resolution and for more than few hours. In the next section, I will discuss an alternative model system that is extensively used for developmental studies: the nematode worm *Caenorhabditis elegans*. Moreover, I will argue that *C. elegans* represents an ideal model system to study the role of noise in development.

1.3 The role of *C. elegans* in developmental biology

In the early 1970s, with the pioneering work of Sydney Brenner, the nematode *C. elegans* has emerged as a model system in many fields in biology [41]. *C. elegans* is a soil nematode consisting of ~1000 cells. The full development from single-celled embryo to adult organism is ~48 hours long, and allows a 50 µm long egg to develop into a 1 mm adult organism. After 12 hours of embryonic development, a newly hatched larva grows for 36 hours into an adult organism. The post-embryonic development is divided in four larval stages (L1-L4), and at the end of each larval stage the animal enters a lethargus stage of 2 hours (Fig. 1.4). During this period, motility is strongly reduced and feeding stops. Eventually, a new cuticle is synthesized and the old one shed, an event called ecdysis, which then marks the start of the next larval stage.

Typically animals exist as hermaphrodite, which reproduce by self-fertilization. The progeny is therefore genetically identical to the mother except for rare random mutations. A single adult hermaphrodite can produce up to 350 offspring. At the same time, males are produced at low frequency (~0.1%), allowing for cross progeny. The simple genetics involved made *C. elegans* the first multi-cellular organism with a complete genome sequenced, revealing more than 19000 genes of which at least 40% code for proteins with homologous in higher organisms [42]. Many key regulatory genes in developmental and cell biology processes have so far been identified.

Thanks to its simple genetics, short life cycle, ease of maintenance and simple body plan, *C. elegans* is an ideal model system to perform developmental studies. In particular, all cells in the body can be imaged and identified using differential

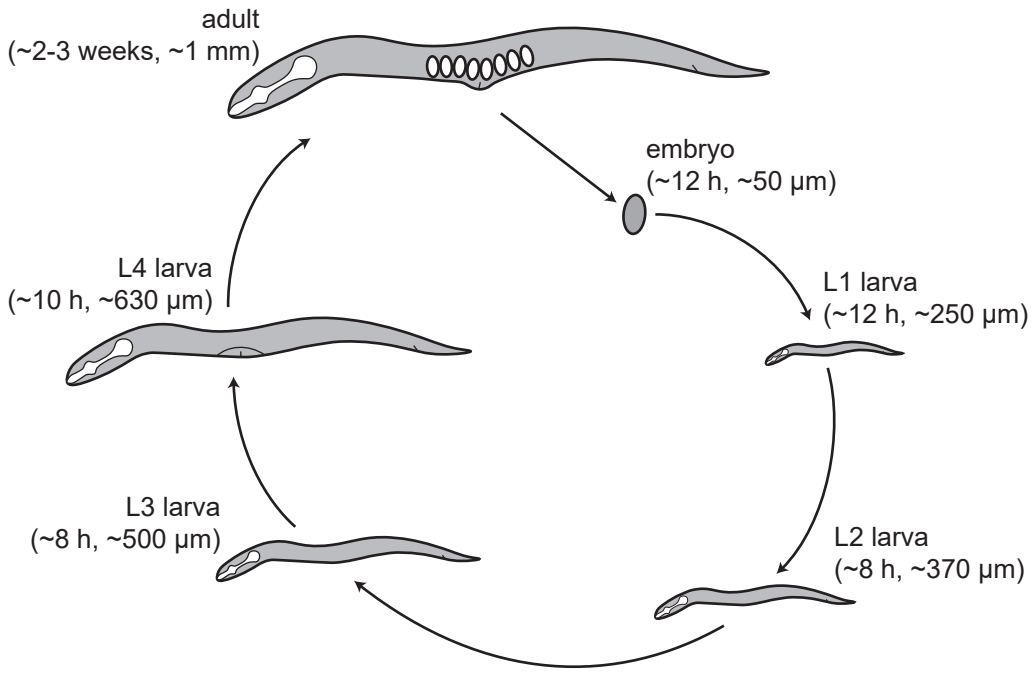

Figure 1.4: Schematic of *C. elegans* life cycle at $22°C$**.** Embryos are laid approximately 3 hours after fertilization and continue developing for about 9 hours until hatching occurs. Numbers next to each animal indicate the length of each larval stage and the approximate length right after each ecdysis event. Figure adapted from *Introduction to C. elegans anatomy* chapter (WormAtlas).

interference contrast microscopy (DIC). As a result, all cell divisions have been detected and the full lineage from single-celled embryo to adult organism has been reconstructed [43].

Surprisingly, this study revealed that *C. elegans* development is largely invariant, in that cells divide and differentiate in a stereotypical manner. This suggests that *C. elegans* development, because of its extraordinary robustness, must be optimized to strongly suppress noise. For this reason, *C. elegans* is an ideal model system to study how deterministic developmental processes efficiently suppress molecular fluctuations. In this thesis, we did not directly examine mechanisms of noise suppression, but, as a starting point, we characterized the degree of variability in two developmental processes that show an invariant outcome: stem-cell like division patterns (Chapter 3) and gene expression oscillations during development (Chapter 4).

Even though *C. elegans* development is largely invariant, a few examples exist in which cells undergo stochastic cell fate decisions [44, 45]. The fact that these stochastic cell fate decisions take place within an environment inside the animal which is otherwise invariant, could potentially make it easier to pinpoint the sources of noise driving the cell fate decision. In Chapter 5 of this thesis, we perform a

quantitative analysis aimed to elucidate the sources of noise and the mechanisms underlying one of the best-understood stochastic cell fate decisions in *C. elegans*: the so-called AC/VU decision [37].

Because of the highly dynamic behavior and long duration of these processes, an approach able to follow single *C. elegans* larvae over the full post-embryonic development is an essential requirement. Moreover, because these developmental processes often involve a small number of cells, this approach should provide enough spatial resolution to follow single cells. In the next section, I will review a number of techniques currently used to perform time-lapse microscopy of *C. elegans* development and argue that none of them are suitable for the experiments we aim to perform.

1.4 Time-lapse microscopy of *C. elegans*

A first basic time-lapse microscopy protocol has been established in 1988 to follow *C. elegans* larvae during development [46]. This technique is meant to aid the lineage analysis during the post-embryonic development of the animal [47], and requires manual loading of a single larva on a standard microscopy slide together with a small amount of *E. coli* bacteria as food source. Standard DIC microscopy techniques then allows researchers to image single nuclei and detect cell divisions.

Despite the technical simplicity of this technique, it is an inefficient way of imaging live animals, and presents several disadvantages. First, the whole process is manual, therefore extremely time-consuming and laborious. Second, only a single animal can be imaged at a time, thus severely limiting its throughput. This is in particular a problem when multiple animals in parallel need to be followed.

As an improved version of the previous technique, some paralysis-inducing drugs such as levamisole or sodium azide can be used to follow many animals in parallel by preventing them from moving [48]. However, such drugs also prevent the animal from feeding, leading to developmental arrest within a few hours. Therefore, a technique that combines the ability to follow many animals in parallel and to perform imaging over developmental time-scales is required. In order to tackle these challenges, several approaches have been recently developed that rely on microfluidic devices.

1.4.1 Microfluidic devices to study *C. elegans*

Microfluidics recently emerged as an important tool to perform microscopy analysis of *C. elegans* animals. In the last decade, microfluidic devices have been successfully used to study single bacterial cells [49], yeasts [50] and fruit fly embryos [51]. One of the great advantages of microfluidic devices is that environmental conditions can be controlled, possibly allowing for diffusion of chemicals at a specific time. Typically, a master mold with the desired pattern is created with soft-lithography

techniques. The mold is then used to create the inverse pattern in a soft material. PDMS (polydimethylsiloxane) is often the favorite material as it is transparent, permeable and biocompatible [52].

As many other biological fields, the *C. elegans* research field has been impacted by the advent of microfluidics, and a large variety of microfluidic devices has been recently designed [53, 54]. One typical application is worm handling, in which individual animals are loaded into narrow channels using an external flow [55]. Similarly, immobilization techniques can be used to perform high resolution imaging of sub-cellular structures. Immobilization can be achieved by flowing a cooling liquid in a separate channel [56], by deforming a flexible layer to compress the animal in a loading channel [57] or by reversibly gelating the surrounding fluid [58]. When immobilization is not necessary, animals can be placed in chambers or droplets, where food is provided and biological waste is removed through fluidic channels [59].

The majority of these techniques is geared towards the handling of adult animals, and they have been successfully used to perform behavioral studies, mutant screening and laser microsurgery [60–62]. However, as food is not provided to the animals, these techniques are not designed to sustain the full post-embryonic development. In the very few cases in which normal larval growth was supported, the techniques lacked the required spatial resolution to study sub-cellular processes [63, 64]. Moreover, the technological complexity of such techniques, consisting of multiple layers channels, liquid flow controls and surface treatments is a technological barrier for many *C. elegans* biology laboratories.

In this thesis, I present an approach in which larvae are confined in small microfabricated chambers that have minimal impact on the animals in terms of mechanical stress (Chapter 2). At the same time, animals are able to freely move and feed in order to progress through the full post-embryonic development. Moreover, the minimal technological investments make our approach highly accessible to standard biology laboratories.

1.4.2 Microscopy techniques to image developmental processes

In addition to a device able to handle individual animals, a microscopy technique able to image developmental processes in live *C. elegans* larvae is needed. Development of multi-cellular organisms is driven by a variety of processes, such as tissue formation, cell division and gene expression. Thus, the main challenge in imaging developmental processes is to follow processes that occur simultaneously and at very different length scales. Specifically, this requires an imaging technique with a field of view large enough to image the whole animal, but still with enough spatial resolution to image sub-cellular events.

Many recent approaches try to match a large field of view with high spatial resolution. In fluorescence microscopy, axial resolution can be improved by optical

sectioning, a way to reject fluorescence light coming from out of focus focal planes [65]. Such techniques include confocal microscopy and two photon microscopy. Despite the high spatial resolution, these techniques require scanning of the incident beam over the area to be imaged. Therefore, there is a trade-off between field of view and acquisition speed. Often, high frame rate is achieved by illuminating only a small area, therefore limiting the field of view.

Techniques that are capable of large field of view imaging and high spatial resolution are limited. Recently, light sheet fluorescence microscopy (LSFM) proved to be an important technique capable of imaging large samples with high frame rate and medium resolution [66, 67]. With LSFM two objectives are used. An illumination objective shapes the laser beam in a thin sheet. A detection objective oriented in the orthogonal direction is used to collect the fluorescence light emitted from the sample. The main advantage of this technique is that phototoxicity, i.e. the toxicity damage caused in the sample by illuminating with high intensity light, is reduced compared to standard confocal techniques. That is because a single plane is illuminated at the time. Moreover, imaging can be fast, as no laser scanning is required, as in confocal microscopy. Light sheet fluorescence microscopy has been applied successfully to the study of embryonic development of *Drosophila*, *Zebrafish* and *C. elegans* [68, 69]. However, these techniques are not suited for imaging of *C. elegans* larvae, as they require a peculiar sample loading, in which the organism is embedded in a cylinder made of agarose gel and placed vertically in the microscope [70]. Few alternative configurations exist in which sample loading is more conventional, but these come at the cost of increased complexity in the design and have never been tested for developmental studies [71–73].

A novel and recent development of optical sectioning techniques is multifocal temporal focusing [74, 75]. This technique has the typical diffraction limited resolution of a two-photon imaging system and is able to image large field of views at high speed. The microscope design is completely equivalent to a standard confocal microscope, so that the sample can be loaded on the stage with a standard microscope slide. Temporal focusing has been used to perform whole brain calcium imaging at high spatial and temporal resolution in *C. elegans* and mice [76, 77], and it represents the most promising technique for fast, large field of view, high resolution imaging of freely moving animals. However, this technique is geared towards the imaging of thick opaque samples such as brain tissues. Therefore, when studying a simple transparent organism such as *C. elegans*, this technique is unnecessarily complicated. In fact, while optical sectioning is essential for thick samples imaging, it is often unnecessary for *C. elegans* imaging [78]. Instead, in order to image freely moving animals, we chose to develop a simpler technique that is optimized for acquisition of large field of views at high speed with high enough spatial resolution to follow single cells.

In this thesis, I present a technique to perform long-term fluorescence time-lapse microscopy of live *C. elegans* (Chapter 2). Our approach uses an imaging system

that is capable of acquiring large field of views at high frame rate but, at the same time, that is able to resolve single cells and sub-cellular structures. We use bright epi-fluorescence laser illumination to provide sharp and highly resolved fluorescence images with high temporal resolution in freely moving animals.

1.5 Thesis outline

In Chapter 2, I describe our fluorescence time-lapse microscopy technique: a combination of microfabricated chambers, wide-field fluorescence microscopy and image analysis. I provide the protocols used to perform the microfabrication, a detail description of our imaging system and a characterization of the performance of the setup in terms of single cell localization and fluorescence intensity quantification. Next, I test whether *C. elegans* larvae develop normally in our microfabricated chambers. In particular, I elaborate on the effects of microchamber dimensions and food availability on the development of *C. elegans* larvae. I find that individual animals develop normally in our microchambers as long as food is available.

In Chapter 3, I test the capability of our approach to follow single cells, by performing a quantitative lineaging study of cell divisions during development. In particular, I perform lineage analysis of seam cells, a model system for stem cell-like behavior, in multiple animals over the full post-embryonic development. To this end, I use fluorescence time-lapse microscopy of animals in which seam cell nuclei are fluorescently labeled. First, I perform a quantitative analysis of the time of division of all the seam cells in multiple wild-type animals. I find that some seam cells divide on average before others, suggesting that stage- and lineage-dependent temporal cues are responsible for the temporal regulation of seam cell divisions. Next, I characterize the variability in timing of divisions in this otherwise invariant developmental process. Moreover, by repeating the lineage analysis in mutant animals in which these cells do not follow the stereotypical division pattern, I show that stage- and lineage-dependent mechanisms are responsible for the correct execution of the stem-cell like divisions.

In Chapter 4, I prove that our setup is capable of quantifying gene expression levels, even in single cells, using fluorescence transcriptional reporter strains. To do so, I quantify the dynamics of expression of two genes which show an oscillatory behavior over the course of development. The first gene is expressed in the whole body of the animal, while the second is exclusively expressed in a number of cell nuclei. I find that expression of these two genes peaks once every larval stage. Next, I characterize the noise levels in the dynamics of these oscillations, and find that the times of the oscillation peaks show significant animal-to-animal variability. However, these times strongly correlate with the times of the closest molt, suggesting that a noise generated by a common source equally impacts the times of oscillations peaks and the times of ecdysis.

In Chapter 5, I show that our approach contributes to the understanding of a simple stochastic cell fate decision, the AC/VU decision, which relies on the

communication between two cells, referred to as α cells. Thanks to the well-known underlying gene regulatory network, we can use our time-lapse microscopy technique to study, for the first time, the dynamics of expression of the key molecular players involved in the decision. To this end, I use our fluorescence time-lapse microscopy technique on transcriptional reporter strains. Here, I aim to elucidate the sources of noise responsible for the AC/VU cell fate decision process. I show that, as previously reported, the birth order of the α cells biases the outcome of the process. However, I also show that other sources of noise must be responsible for the cell fate determination when the two α cells are born at similar times. Next, I explore whether the stochastic expression of *lag-2*, one of the key components of the underlying gene regulatory network, before the time of births of the α cells, i.e. in their mother cells, could form this additional source of noise and, hence, bias the decision when the α cells are born at similar times. However, our results are not conclusive, leaving the identification of additional sources of noise an open question. At the end, I comment on future directions to address this open question.

2

Experimental method and *C. elegans* development in microfabricated chambers

This chapter is part of the following publication:
"N. Gritti, S. Kienle, O. Filina and J. S. van Zon,
Long-term time-lapse microscopy
of *C. elegans* post-embryonic development.
Nat. Commun. 7:12500 doi: 10.1038/ncomms12500 (2016)."

Thanks to its simple body plan, short life cycle and transparency, *C. elegans* is an ideal model system to perform quantitative studies of developmental processes. Despite these advantages, there is currently no technique available to study the full post-embryonic development of individual living *C. elegans* with high spatial and temporal resolution. This limitation is due to the high motility of *C. elegans* larvae and their need to feed in order to properly develop. The standard time-lapse microscopy technique consists on imaging freely moving animals on a nematode growth medium (NGM) agar plate or on a microscope slide. Although this technique has been successfully used to perform neuronal and optogenetic studies [79, 80], it does not allow to image multiple animals in parallel, a key requirement when studying stochastic processes.

Current microfluidic devices designed to perform time-lapse microscopy of *C. elegans* are optimized to temporarily immobilize the animal, allowing high resolution imaging. Immobilization is accomplished using various strategies, including clamping [81, 82], compression [83, 84], cooling [85], nanometer size

beads [86] and gelation of the environment [87]. However, approaches based on microfluidics to immobilize animals have two major disadvantages. First, they are not designed to sustain imaging over developmental timescales. Second, their complicated designs often have undesired impacts on the animals during imaging. For instance, immobilization techniques have the potential to damage the cuticle of the larvae or to cause stress responses. In fact, previous works confirmed that physiological changes occur as a response to chemicals, mechanical stimulations and temperature changes [88–91].

In order to perform time-lapse microscopy over developmental timescales, single animals should be kept confined in an area that contains enough food to ensure proper development. Recently, solutions have been proposed that sustain larval development. Such systems use wells filled with agar gel and nutrients [63], growth chambers with inlet and outlet channels [64] and water-in-oil droplets filled with an aqueous solution containing nutrients [92]. This techniques have been successfully used to study motility of *C. elegans* larvae when exposed to different chemicals [93] and to quantify some markers of developmental progression such as growth rate and timing of larval stage transitions [64]. However, due to the large size of the compartments, these techniques are not compatible with high resolution imaging. Therefore, they do not provide sufficient spatial resolution to study developmental processes at the single-cell level.

We aimed to design a technique in which the impact of the device and imaging system on the development of the larvae is minimal. Ideally, this technique should be sufficiently simple as to be used by *C. elegans* biology laboratories, while at the same time allowing to perform time-lapse microscopy of post-embryonic *C. elegans* development with high spatial and temporal resolution over multiple animals in a parallel fashion.

Inspired by previous works [94], we explored the possibility of confining individual larvae in microfabricated compartments. First, we confine individual larvae in hydrogel-based microcompartments filled with *E. coli* bacteria as food source. The microfabricated chambers are large enough to provide sufficient food to sustain development for the full duration of the experiment, while small enough to fit in the field of view of the camera chip when using high magnification objectives to capture single-cell processes. Second, we use an imaging acquisition setup capable of acquiring images of larvae as they move inside the chamber. A combination of fast camera and bright illumination allows us to acquire sharp transmission and fluorescence images at different focal planes for each chamber even when animals are highly motile. Third, we use image analysis to reconstruct the dynamics of developmental processes between images at different time-points, such as cell divisions. This is a crucial part of our technique: instead of mechanically modifying the body shape and constraining the animal in a narrow channel, we image freely moving animals and exploit image processing techniques to obtain results that are independent of the body shape of the animal. For instance, we computationally straighten the animal body to define a convenient anteroposterior reference system.

This aids the analysis of the developmental processes we are interested in, including cell division detection and gene expression quantification, both in the whole animal and in single cells. One great advantage of our technique is the ease of use compared to previous microfluidics approaches: no multiple layers channels or liquid flows are required. Even though the idea of using microcompartments to confine individual animals is not new [94], it has only been used to study behavior over a limited time period and not to follow cellular dynamics over the full duration of development. Moreover, for reasons to be discussed in the next section, we propose to use an alternative material, polyacrylamide hydrogel, to the one previously used, agarose hydrogel.

In this chapter, I describe in detail our technique and show that it can sustain normal development. In Section 2.1, I describe how to fabricate microchambers in polyacrylamide hydrogel and how to confine *C. elegans* in such chambers. Next, I introduce the fast acquisition setup to perform volumetric imaging at ~100 fps in an automated fashion (Section 2.2). In the same section, I characterize the ability of our setup to quantify fluorescence signals and I briefly comment on the amount of data generated by our technique. Finally, in Section 2.3, I test whether wild-type *C. elegans* larvae develop normally when confined in microchambers by quantifying several markers of developmental progression.

This chapter shows that we have developed a powerful new technique to perform time-lapse microscopy of freely moving and feeding *C. elegans* larvae in a parallel fashion and with high spatial and temporal resolution. In addition, our findings show that microchambers are able to sustain the full post-embryonic development of *C. elegans* larvae.

2.1 Microfabrication of polyacrylamide hydrogel chambers and sample preparation

Due to their tunable mechanical properties [95], hydrogels are the most common choice for the creation of microenvironments to study micro-organisms. In particular, agarose hydrogel has been succesfully used to confine bacteria for single cell studies [96–98]. The great advantage of this hydrogel is its permeability to chemicals, which provides control and uniformity of the microenvironment without the need of complicated flow systems. Recent experiments showed that agarose hydrogel microcompartments can be created to confine live nematode larvae for behavioral studies [94]. However, agarose is fragile and difficult to handle, especially in the thin layers required to create the microcompartments. Moreover, agarose consists mainly of water and galactase, which is easily metabolized by micro-organisms [99]. Therefore, the microenvironment to which single animals are exposed is subject to degradation.

A good alternative to agarose is polyacrylamide. Polyacrylamide hydrogel

has many practical advantages that make it an ideal material to create microenvironments to confine biological samples. Polyacrylamide is widely used for DNA and protein electrophoresis, and thus it is easily accessible to biology laboratories. Polyacrylamide gels are ideal for microfabrication because they have highly tunable elastic properties and their micropatterning is easily accomplished by cost-effective techniques [100–102]. Thanks to its versatile mechanical properties, polyacrylamide is less brittle and easier to handle (fracture energy G ~10 - 50 $J \cdot m^{-2}$) than agarose (G ~0.1 - 6 $J \cdot m^{-2}$) [103]. Moreover, in contrast to agarose, the polymers that compose the gel are not metabolized, making it an ideal material to study biological samples in a stable microenvironment. Despite the fact that residual monomers in the gel are toxic, polyacrylamide is fully biocompatible when proper washing steps are used to remove the monomers [100]. Polyacrylamide hydrogel has been successfully used to fabricate highly controllable microenvironments to observe bacteria, yeast and, for short time periods, *C. elegans* [104].

Considering its ease of use and tunable mechanical properties, we chose polyacrylamide hydrogel to create microfabricated chambers to confine larvae in a small area. Chambers are filled with food to sustain development over the course of the experiment. Therefore, chamber dimensions should be chosen based on the duration of the biological process of interest. The shape of the chambers should also be optimized: considering that most cameras have a squared chip, we designed squared microchambers to maximize the relevant area that is imaged. The depth of the chambers is also optimized. On the one hand, they are shallow enough to prevent *C. elegans* larvae from moving in the axial direction, therefore minimizing the number of focal planes to be imaged. On the other hand, chambers are deep enough to prevent larger animals from being damaged by mechanical compression. To this end, the tunable mechanical properties of the hydrogel are beneficial, as we can optimize polyacrylamide stiffness such that it deforms to accomodate larger animals with modest compression in the axial direction.

2.1.1 Microfabrication

In our approach, we created a master mold with standard soft-litography techniques [105]. To pattern a 4 inch silicon wafer, the following protocol was used:

- The 4 inch silicon wafer was cleaned with isopropanol and cleared of dust particles before heating it on a hotplate at 150°C and cooling it with nitrogen air (N_2). Next, the silicon wafer was spin-coated with an epoxy resin (SU-8, MicroChem, Fig. 2.1A). The viscosity of the epoxy resin was chosen and the speed of the coating was tuned to obtain homogeneous layers of 10 or 20 µm (Table 2.1).

- The silicon wafer was placed on a hotplate at 65°C for 3 minutes and transferred to a 95°C hotplate for 5 minutes. The silicon wafer was then allowed to cool down at room temperature for about 30 minutes. This process, called soft

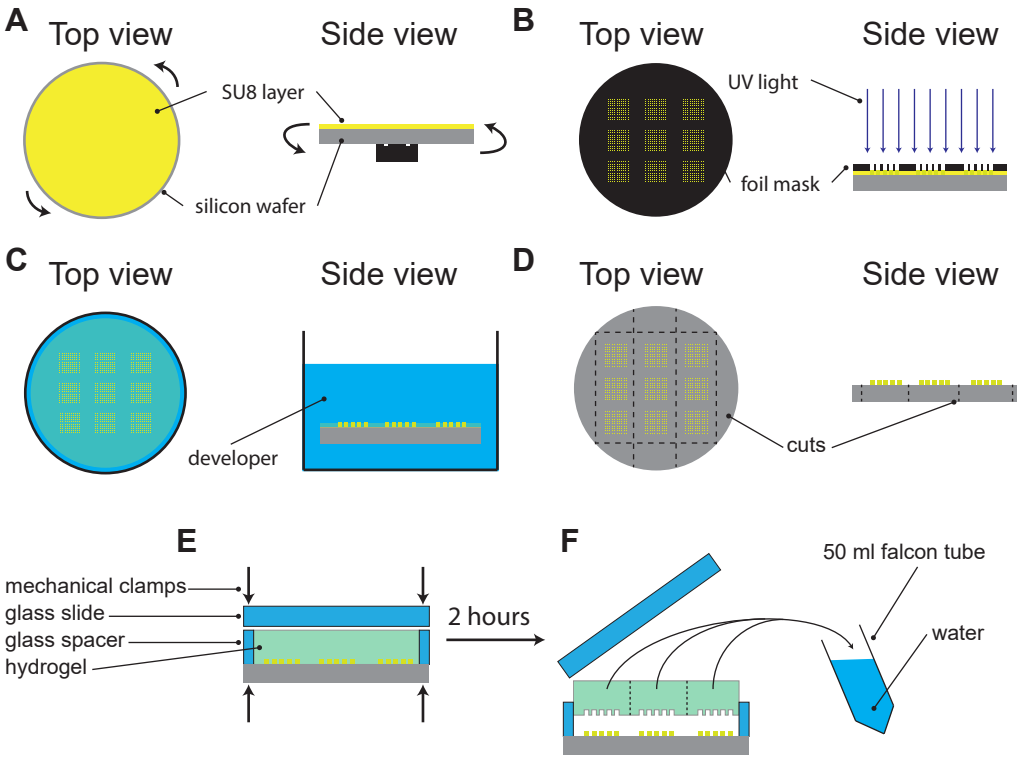

Figure 2.1: Fabrication of microchambers. (**A**) A thin layer (10-20 µm) is spin coated on a 4 inch silicon wafer. The maximum speed is reached in two steps: first, to homogeneously spread the SU-8, 500 rpm speed is reached with an acceleration of 100 rpm/s, and it is maintained for 15 seconds. Then, the desired speed is reached with an acceleration of 500 rpm/s and maintained for 45 seconds (Table 2.1). (**B**) The silicon wafer is exposed to UV light. A foil mask is used to pattern the SU8. Exposure time used was 20 s. (**C**) The silicon wafer is immersed in SU-8 developer (Mr. Dev 600) for approximately 3 minutes to remove the SU-8 in excess. (**D**) The patterned silicon wafer is cut in 3 molds with the same size as a glass slide (26 mm x 76 mm). (**E**) Preparation of the polyacrylamide chambers. One mold is glued to a glass spacer with high vacuum grease. A 29:1 solution of polyacrylamide-bisacrylamide is poured in the cavity. A silanized glass slide is lowered on the solution and mechanically clamped. (**F**) After approximately 2 hours, the glass slide is removed. Each array of chambers is cut and washed in distilled water.

bake step, was needed to improve the adherence of the SU-8 to the surface of the wafer.

- Epoxy resins are negative photoresists, i.e. light-sensitive materials that cross-link when exposed to ultraviolet light ($\lambda \leq 400$ nm). We then used a foil mask and exposed the image to UV light, such that only part of the SU-8 layer cross-linked (Fig. 2.1B). The time the mask is exposed depends on the power of the illumination source, and in our case we used a 20 second exposure time at 25

	Thickness (μm)	
Speed (rpm)	SU-8 3010	SU-8 3025
3000	12	26
3500	10	22.5
4000	9.5	19.5

Table 2.1: Thickness of SU8 photoresist. The thickness of the photoresist depends on the maximum speed and on the viscosity of the SU-8 used. SU-8 3025 is more viscous than SU-8 3010. Thickness is in μm.

mW. The foil masks contained the desired pattern, in our case consisting of 9 arrays of 10x10 squared chambers. Final dimensions of the microchambers are equal to the dimensions of the structures on the mask.

- A post bake step was used to help adhesion of the cross-linked SU-8 to the silicon surface. The silicon wafer was treated at 65°C for 1 minute and at 95°C for 6 minutes. Subsequently, it was let to cool down at room temperature.

- To remove the SU-8 in excess, we immersed the full silicon wafer in a chemical solvent (Mr. Dev 600) for about 3 minutes, a process called development (Fig. 2.1C). The wafer was immersed for 10 seconds in another beaker with fresh developer and for another 10 seconds in isopropanol to stop the development. The patterned wafer was then dried with N_2 air.

- Once the silicon wafer was dry, it was hard baked at high temperature (200°C) for 30 minutes on a hot plate to further cross-link the SU-8. This step also greatly improves the hardness of the micropattern, therefore preventing usage damage.

- The silicon wafer was then cropped with a diamond cutter to create the three final master molds, each containing 3 arrays of 10x10 structures (Fig. 2.1D).

Once the patterned silicon wafer is ready, the fabricated mold can be used many times to create microfabricated chambers in polyacrylamide hydrogel. To prepare the polyacrylamide, we used a 29:1 ratio of acrylamide/bis-acrylamide solution (Bio-Rad) diluted to a final 10% concentration. Ammonium persulfate (Sigma, 0.1% of the volume) and TEMED (Sigma, 0.01% of the volume) were added to trigger the polymerization. The solution was poured in a cavity created by a hollowed standard microscope slide glued to the micropatterned silicon wafer with high vacuum grease. The polymerization reaction starts immediately upon addition of TEMED, therefore the solution must be poured in the cavity within 3-5 minutes. The cavity was then closed with a silanized glass slide and sealed by mechanical clamping (Fig. 2.1E). The solution was left to polymerize for at least 2 hours. When the gel was ready, the three arrays were cut with a scalpel from each cavity (Fig. 2.1F). After

polymerization, acrylamide monomers might still be present in the resulting gel. Acrylamide monomers are known to be a powerful neurotoxin, thus with the potential to negatively impact development of *C. elegans* larvae. To remove the monomers, at least 3 washing steps in distilled water of at least 3 hours each were necessary. When using fewer or shorter washing steps, we found that *C. elegans* larvae development was arrested during the first or second larval stage. Polyacrylamide gels could be stored in distilled water for at least 15 days without any visible degradation.

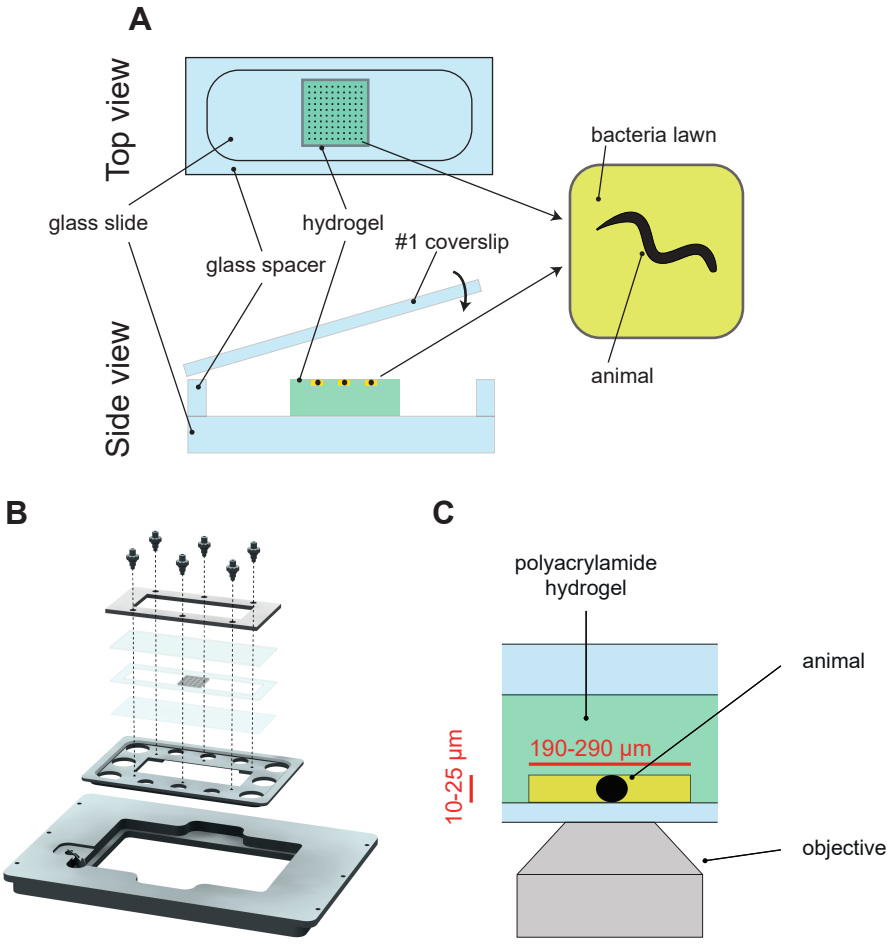

Figure 2.2: Sample preparation. (**A**) Schematic of the sample. A glass spacer is glued to a glass slide. The microchamber array is placed in the center of the cavity and single animals are transferred together with bacteria in the microchambers. The sample is closed with a coverslip ~100 µm thick. (**B**) The sample is mechanically clamped and sealed in a custom fabricated sample holder to prevent liquid evaporation. (**C**) The sample is placed upside down on the microscope to perform epi-fluorescence microscopy.

2.1.2 Sample preparation

To prepare the sample, we first transferred a microchamber array in M9 buffer for about 4 hours. *C. elegans* larvae were synchronized as follow: 15-20 adults were transferred on a fresh NGM agar plate spotted with *E. coli* bacteria (OP50) and allowed to lay eggs. After about 2 hours, the adults were transferred back to the original plate, so that the eggs left on the fresh plate were synchronized within a 2 hours period. The eggs on the fresh plate are then ready to be immediately transferred into the microfabricated chambers. A glass spacer with the same height as the polyacrylamide gel was glued to a glass slide using high vacuum grease (Fig. 2.2A). A single microchamber array was positioned on the glass slide, with the microchambers facing up. Excess liquid was removed with a tissue. The required time to transfer around 25-30 embryos is about 15 minutes. This is already long enough for the liquid to evaporate, causing the polyacrylamide gel to bend. To prevent this, a ~40 µl drop of M9 buffer was placed on the side and on the surface of the microchamber array, taking care to not let the liquid fill the chambers. Under a dissection microscope, a drop of bacterial suspension containing a single embryo was collected with an eyelash and transferred from the NGM agar plate into a single microchamber. To facilitate the release of the bacteria and embryo into the chamber, the eyelash was briefly dipped into the M9 drop prior to touching the microchamber. Ideally, the microchamber was already filled with enough OP50 bacteria after this step. However, if necessary, more bacteria were transferred to fill it completely. Subsequently, excess liquid was removed with tissue paper and the sample was closed with a #1 coverslip. The coverslip was lowered slow enough to avoid the formation of large air bubbles in between the polyacrylamide and the coverslip. The sample was then placed on a holder fabricated by the AMOLF mechanical workshop. The holder is optimized to minimize weight, thus allowing for rapid sample scanning along the axial direction. Moreover, the holder contains mechanical clamps to prevent liquid evaporation from the sample during the full duration of the experiment (Fig. 2.2B, C). Our design allowed us to load up to 50 chambers in a single sample.

2.2 Time-lapse microscopy setup

In order to study developmental processes with single cell resolution, we need to image individual chambers with high magnification and high numerical aperture (N.A.) objectives. However, *C. elegans* larvae can be highly motile. Therefore, in order to avoid motion blur due to the animal movement during a single image acquisition, we used an imaging system that provides bright illumination to reduce exposure time as much as possible. Moreover, to minimize movement between images acquired at different Z positions, we optimized our imaging system to quickly scan the sample along the Z direction.

Typically, cell lineages, migration and differentiation in *C. elegans* span many

hours of the post-embryonic development. Therefore, images typically need to be acquired on a timescale of minutes in order to resolve the dynamics of the developmental process. However, fluorescence microscopy causes phototoxicity in biological samples, especially when bright illumination (e.g. lasers) is used with long exposure times. A trade-off between exposure time, illumination power and time interval had to be determined for every experiment, but we generally found that 5-20 minutes time resolution and 1-10 ms exposure time do not lead to detectable phototoxicity. Moreover, as we want to perform parallel imaging of multiple animals, an automated system able to move through different chambers and acquire volumetric images is necessary.

2.2.1 Imaging setup

Instead of designing a completely new imaging system, we decided to optimize a commercially available inverted wide field microscope (Nikon Ti-E) to our needs (Fig.2.3A). We opted for a standard epi-fluorescence microscope with limited optical sectioning capability in favor of bright illumination and fast volumetric imaging. For all the experiments performed, the optical sectioning of our imaging setup was enough to resolve single cells and sub-cellular features. In fact, while optical sectioning techniques are essential for thick samples like vertebrates, they are often unnecessary for *C. elegans* imaging [78].

In our setup we used high magnification objectives (40X and 60X) and a camera with the largest possible chip (2048 x 2048 pixels Hamamatsu sCMOS Orca v2). The high numerical aperture of both objectives (N.A. = 1.3 for 40X, 1.4 for 60X) provides high spatial resolution, allowing to resolve sub-cellular structures (<1 μm). At the same time, the field of view of the camera was large enough to accommodate an entire chamber. In order to minimize the amount of UV light in the sample, which causes *C. elegans* larvae to move faster [106], transmission imaging was performed using a red LED (CoolLED p-100 615 nm).

In addition, we equipped our setup with two lasers for excitation of green (Coherent OBIS LS 488-100) and red fluorophores (Coherent OBIS LS 561-100). In contrast to standard lamp illumination systems, lasers have a much narrower bandwidth and a much higher intensity (80-100 mW). With these lasers, even very short exposure times (1-10 ms) were enough to have a high signal-to-noise ratio for all the strains studied. Moreover, as *C. elegans* larvae are highly motile even in absence of UV light (peaking at 50 μm s^{-1} for reversals), short exposure times minimize or even eliminate motion blur of fluorescently-labeled cells during acquisition. The two laser beams were combined in a single optical path with a dichroic mirror (Semrock LM01-503-25). In order to illuminate the microfabricated chambers as homogeneously as possible, we expanded the original laser beam from 0.7 mm to 36 mm with a telescope composed of two achromatic lenses of 10 and 500 mm focal length (Thorlabs), respectively. The expanded beam was then aligned through dielectric mirrors (Thorlabs) to enter the back aperture of our Nikon Ti-E inverted

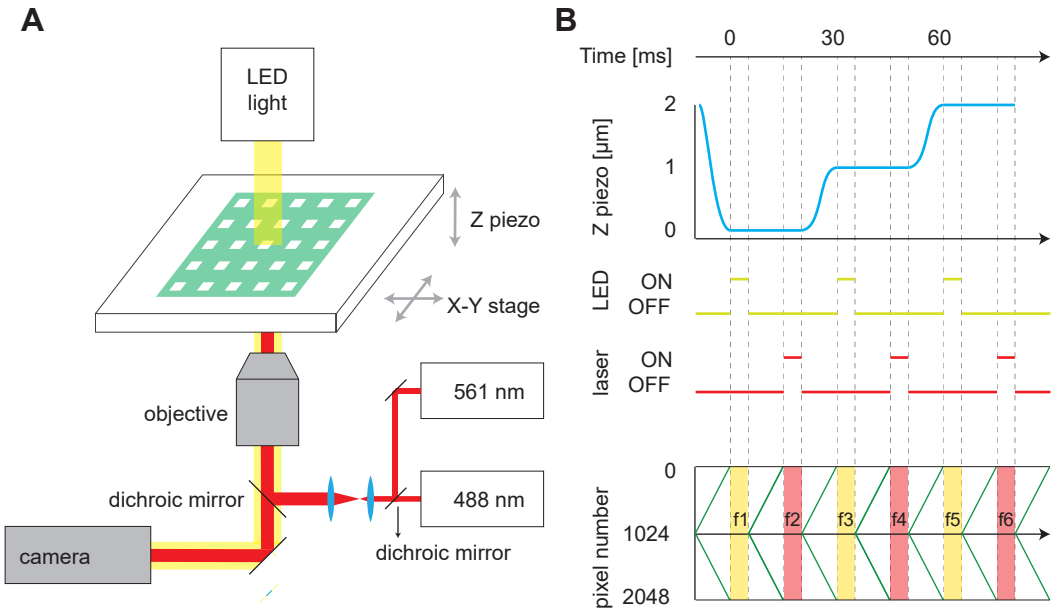

Figure 2.3: Imaging system. (**A**) Schematic of the optical setup. (**B**) Representation of the synchronization of the devices during volumetric imaging of a single chamber with two imaging channels (transmission LED and one of the two lasers). The camera is operated in rolling shutter mode: every line of the camera chip is active at slightly different times (green lines, bottom part). The delay between the first and the last lines is about 10 ms. In our case we synchronized the laser and LED (yellow and red lines, middle part) to switch ON only when all the pixels of the camera chip are active in order to perform a global exposure (yellow and red rectangles, bottom part). We synchronized the piezo to move to the next position only when both channels have been imaged and when the camera is not in global exposure (blue curve, top part). In this way, while the camera is reading out the pixel values, the sample is positioned to the next focal plane. In this configuration, two channels with 5 ms exposure times can be image in 30 ms. A full stack of 20 images is acquired in 600 ms.

microscope. A tube lens of 300 mm focal length (Thorlabs) was used to focus the beam in the back focal plane of the objective. We used a dual band filter set (Chroma #59904) to perform fluorescence imaging with both 488 nm and 561 nm excitation without the need to mechanically move between two different filter sets.

In designing the depth of the chambers, there is a trade-off between the amount of food available and the degree of compression in the axial direction: chamber depth (10-20 µm) was optimized to provide enough food to the animals to develop during the full duration of the experiment, while being able to confine the animals as much as possible in the axial direction. In particular, the depth of our chambers ensure that young larvae are slightly compressed in the axial direction, while older larvae are not mechanically damaged by excessive compression. Most of the developmental processes we intend to study are happening in different focal planes, so 3D imaging

is necessary. In most of our experiments, we scanned the full depth of the chambers with 1-2 µm spacing, resulting in a full stack of about 15-20 images. In order to minimize larval movement over the acquisition of a full stack, we used a Z piezo stage (Nano Drive 85, Mad City Labs) to move the sample between two subsequent focal planes within 10 ms.

Accurate synchronization between the laser, the camera and the piezo stage is necessary to make sure that images are acquired at the right focal plane only when the sample is illuminated. The sCMOS camera operates in rolling shutter mode, meaning that the lines on the chip are not active all at the same time, but there is a delay (10 µs) in between the activation of two consecutive rows. Our camera has 2048 rows, and the read out of the chip starts from the row in the center and moves in the two opposite directions, such that two rows are read out simultaneously. Therefore, the delay between the first line in the center of the chip and the last two lines at the edges is about 10 ms (Fig. 2.3B). During the time in which all the lines were simultaneously active and collecting light for the same frame, the laser or the LED was switched ON (rise time 3 µs). When the first line started to be read out, the illumination was turned OFF. This procedure was repeated for all the preselected channels. During the 10 ms in which the image was being transferred from the chip to the internal memory of the camera, the fast Z piezo stage moved the sample to the next Z position (Fig. 2.3B). In this way, acquiring a single imaging volume, consisting of 20 slices in two channels, with 5 ms exposure times and 10 ms readout time, took 20x2x15 = 600 ms.

Since our microfabrication technique allows for confinement of multiple animals in the same sample, we also equipped our setup with a motorized XY stage (MicroDrive, Mad City Labs) to move between different chambers. Because of the long duration of our experiments, the sample may experience significant drift along the axial direction. If the position of the objective is not corrected by the drift of the sample, the distance between the objective and the sample would change over time, and the images would eventually be out of focus. To avoid this, we defined a *home* position in the sample where no chambers are present, and used the Perfect Focus System (PFS) provided by the microscope to correct for sample drift in the Z direction. In particular, the PFS adjusts the position of the objective so that the distance between the objective and the closest glass surface of the sample is constant. As the position of each chamber is defined by the piezo stage, the drift correction did not actually change the position of each chamber, but only the position of the objective relative to the sample. At the end of the waiting time, PFS was switched OFF and images were acquired for all the chambers. After all chambers were imaged, the objective was moved back to the *home* position and the PFS was switched ON again, therefore correcting the position of the objective for the drift of the sample until the next acquisition starts.

Overall, the total time it takes to acquire a full stack of a single chambers (600 ms) was given by the exposure time of a single image and by the readout time of the camera chip. With these exposure and readout times, for all the experiments

performed, we found that larval motility was negligible and that single images were not affected by motion blur. On the other hand, the interval between subsequent time points was instead limited both by the slower XY movement between different chambers and by the data transfer to the computer drive. We found that we could image 30 animals in parallel every 10-20 minutes, which was a sufficient time interval to capture the relevant dynamics of all the developmental processes analyzed in this thesis. While shorter time intervals could be reached in order to capture the dynamics of faster developmental processes, for instance using faster data transfer tools, phototoxicity represents an unavoidable limiting factor on the time interval between subsequent time points. Even though we have observed developmental arrest for short time intervals (3-5 minutes), we did not find any detectable effect on the development of the animals when imaging every 10 minutes, even when using the maximum laser power (100 mW).

2.2.2 Characterization of the setup

Since we designed our setup to perform fluorescence microscopy to follow individual cells and to quantify fluorescence intensity, we first decided to measure the performance of our setup, both in terms of illumination pattern and reliability.

In order to quantify the homogeneity of the excitation beam, we used autofluorescent plastic slides (Chroma) and acquired ~50 images using the PFS to make sure that the same focal plane was imaged. We will refer to such images as flat field images (Fig. 2.4). Because our microscope is designed to expand the beam 50 times, the beam assumed a broad Gaussian profile. This is reflected by the measured pixel intensity distribution, with outer pixels showing ~80% of the central peak intensity. Nevertheless, since many of our experiments were designed to quantify gene expression in single cells with appropriate fluorescence reporter constructs, we acquired this average flat field image after every experiment and used it to apply a flat field correction according to the equation:

$$C = \frac{I - D}{F - D} \cdot \langle F - D \rangle = (I - D) \cdot G \tag{2.1}$$

where C is the corrected image, I is the raw image, F is the flat field image and D is the dark field image. The dark field image is acquired under no light conditions, i.e. when the camera shutter is closed. Brackets represent the pixel intensity averaged over the full image. For each pixel in the position (i, j), the quantity $\frac{\langle F-D \rangle}{(F-D)_{(i,j)}}$ is the gain value G to be applied to correct for the inhomogeneous illumination. This correction factor is particularly important when the same cell is imaged over time, as it will be found in different positions within the field of view over the course of the experiment.

In fluorescence microscopy, every image is affected by blurring. In principle, the acquired image is a convolution of the true object with the blurred image of a point source, known as point spread function (PSF). When imaging conditions

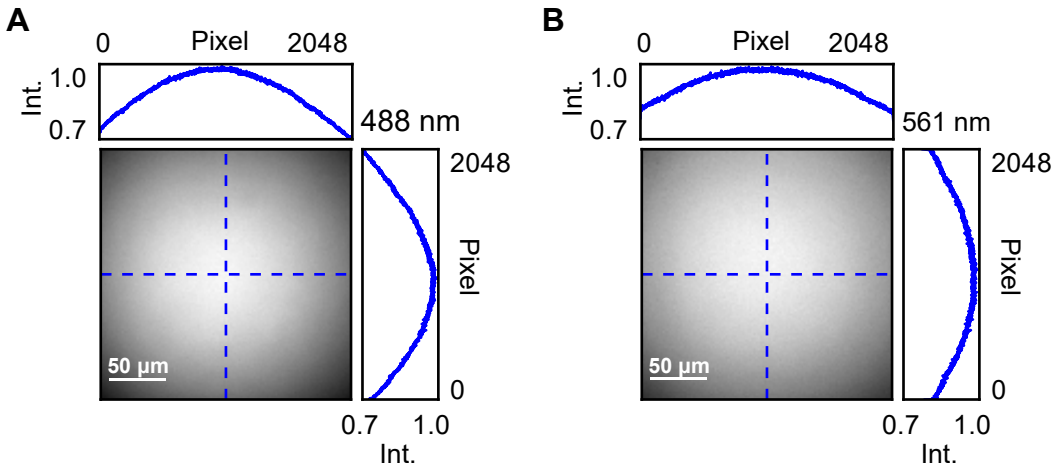

Figure 2.4: Flat Field illumination. An average over 50 images of the excitation profile for both (**A**) 488nm and (**B**) 561nm excitations with the 60X magnification objective. On the right and on top of each image, the plot profile for pixels along the corresponding blue dashed line. Intensities are normalized to the highest pixel value along the dashed line.

are optimal, it is sometimes possible to estimate such function and deconvolve the raw images to recover a sharp representation of the object of interest [107]. This is possible and easily implemented when objects are in a single focal plane, as no out of focus effects need to be considered, and when fluorescence light is not affected by heavy scattering through the sample. Unfortunately, our imaging design involves many components that can cause scattering, including the polyacrylamide itself, the bacteria floating in the microchambers and the tissues in the animal body. Therefore, it is technically impossible to estimate a PSF in all the different conditions of the sample. We therefore decided to estimate how fluorescence quantification is affected by these optical disturbances. To this end, we imaged (i) autofluorescent slides, (ii) beads coated with fluorescent molecules and (iii) fluorescently labeled animals in chambers. We then compared the noise obtained when quantifying fluorescence coming from these different samples (Fig. 2.5).

Autofluorescent slides were imaged under the same experimental conditions as in Fig. 2.4. We then quantified the fluorescence intensity in small regions about 4 µm wide. The time series are shown in Fig. 2.5A (bottom panels). When imaging fluorescent beads, we embedded them in polyacrylamide hydrogel to emulate experimental conditions. Because of the small mesh size of the gel and the large bead diameter (0.7 µm), we assumed that beads are immobilized in the gel, and we imaged a single focal plane with 3-4 seconds time interval (Fig. 2.5B). Position of the beads were annotated manually and fluorescence intensity was computed by applying the Otsu segmentation algorithm [108]. Briefly, this algorithm finds a threshold value that maximizes the difference between pixel values inside and outside the mask. The

mask was applied to a subregion including the bead of interest, and the fluorescence intensity was computed by summing all the pixel values inside the mask. Time traces are normalized by the mean value of each trace.

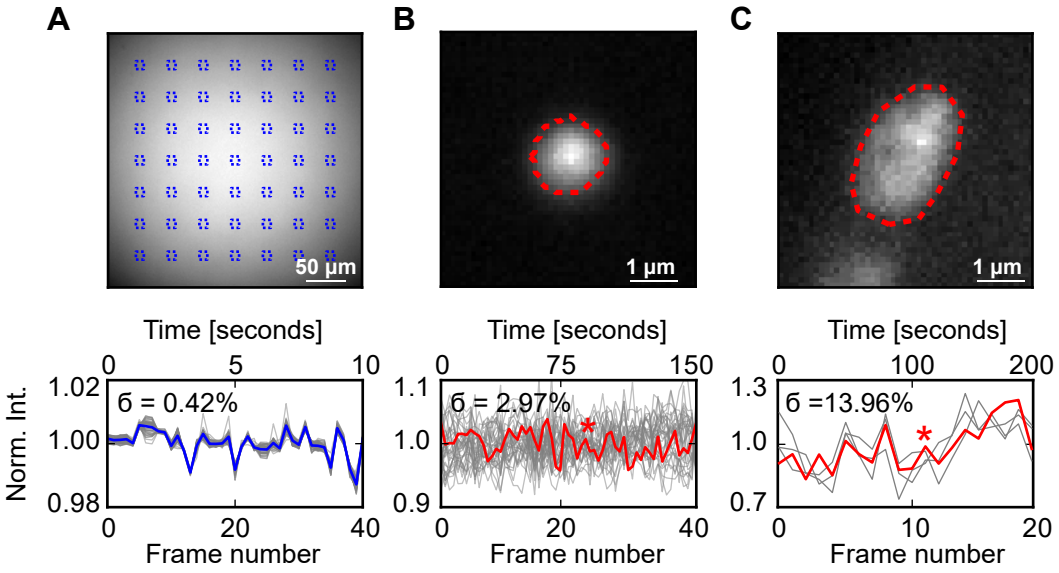

Figure 2.5: Noise characterization. (**A**) Image of an autofluorescent slide (top). Time series (bottom) of regions of interest highlighted with dashed boxes (top). (**B**) Cropped image containing a fluorescent bead immobilized in polyacrylamide hydrogel (top). Time series of the fluorescence intensity (bottom) for all the beads in the original image. The red time series corresponds to the bead shown on top. Red asterisk correspond to the image on top. (**C**) Image of a vulva precursor cell labeled with *hist::mCherry* marker. In red the mask drawn manually. Timetraces for 6 different cells are shown in the bottom. Red asterisk corresponds to the image on top. In all the panels, to facilitate comparisons, time series have been normalized by the mean value of the trace. Standard deviation of the time series is indicated in each panel.

We found that time series of different regions in the autofluorescent slides are highly correlated. This global effect is likely due to the fact that laser power is not constant between different exposures. Nevertheless, such variability, measured as the standard deviation of the time series, is less than 1% when compared to the mean intensity (Fig. 2.5A). Fluorescence intensity collected from the beads is instead highly dynamic, and single traces are not correlated. We found that fluorescence quantification is affected by a 3% error (Fig. 2.5B). This is only partially due to the laser power fluctuation. Instead, we speculate that quantification is highly dependent on the exact position of the imaging plane and on the bead position along the axial direction. This can vary due to small fluctuation in the relative position between the sample and the objective and possibly due to small drifts in the position of single beads in the gel.

So far we have focused on homogeneously fluorescent and immobile objects. However, the final aim of our technique is to image single cells in an otherwise freely moving larva. Therefore, we analyzed the fluorescence intensity of single cells in the *C. elegans* strain *stIs10226[his-72p::HIS-24::mCherry]*, in which a histone promoter directly drives production of mCherry fluorescent protein in all cell nuclei. This is a very convenient strain, as the nuclear marker expression is constant over time. In our case, we used this strain to quantify the nuclear fluorescence of manually selected cells. We imaged single animals in microchambers acquiring a full stack every 10 seconds. We manually created the mask for each analyzed cell in every timepoint. Because cells are mobile in the sample and can be found in different positions, we performed the flat field correction as discussed previously in this section, and quantified the fluorescence intensity of each cell (Fig. 2.4C). We found that the variability of the time series is consistently higher (~14%) than the variability found in the beads. Considering that the time series were acquired in ~3 minutes, and that time series from different cells in the same animal seem to correlate, it is unlikely that the measured variability is due to gene expression noise. Instead, we speculate that such variability is due to some other biological aspects. For instance, the degree of compression of *C. elegans* body is highly variable due to the ~30 seconds defecation cycle. Therefore, nuclei can change their shape and deform, thus affecting the quantification of the fluorescence intensity. Moreover, the bacterial suspension might not be homogeneously distributed in the microchambers and therefore the scattering properties of the sample might be dependent on the cell position in all three dimensions. To prevent our quantification from being strongly dependent on a single noisy image, we occasionally used data filtering approaches, such as Gaussian filtering, to capture only the relevant dynamics of the time traces. When used, I will discuss the filtering techniques in the relevant section for each experiment.

2.2.3 Data handling

Because our camera produces 4 Mp images (2048x2048) with 16 bit depth, every image is 8 Mb in size. Thus, as we typically acquire images in 15-20 different focal planes, a full stack sums up to approximately 160 Mb per imaging channel. Assuming two imaging channels are acquired (e.g. transmitted light and 488 nm fluorescence), a single time point occupies about 320 Mb on the computer hard drive. All together, the amount of data collected for a single animal imaged every 20 min for 48 hours is 50 Gb. Therefore, within a single experiment, the amount of collected data is easily scaling up to hundreds of GB or around a TB, depending on the number of animals imaged in parallel.

A main challenge of the image analysis is to extract the correct quantitative data from the raw imaging data. This requires several non-trivial steps, from loading of large image stacks, to recognition of single cells and quantification of variables such as fluorescence intensity. For each experiment presented in this thesis, a detailed

description of the image processing techniques used to perform these tasks will be given in the relevant section.

2.3 Larval development in microfabricated chambers

In this section I characterize the development of wild-type animals confined in the microfabricated chambers. In addition to show that the microfabricated chambers and the imaging setup are suitable to perform long-term imaging of *C. elegans* larvae, we found that such measurements have the potential to provide new insights in the control of growth and response to food availability during development.

2.3.1 Experimental design and data analysis

To characterize development of wild-type animals in the microfabricated chambers, we performed time-lapse microscopy using red light-emitting diode (LED) trans-illumination. Each experiment was performed until the food source was exhausted or until adulthood. Because no laser illumination was used, we could acquire images with a short time interval (typically 5 minutes). For each animal, we performed an average-projection along the Z-axis of the slices from a single stack. Images at different timepoints were then combined to create a movie of a single animal developing in a microchamber, such that the full ~30 Gb of data for a single animal are compressed in a series of images of ~100 Mb (~350 frames).

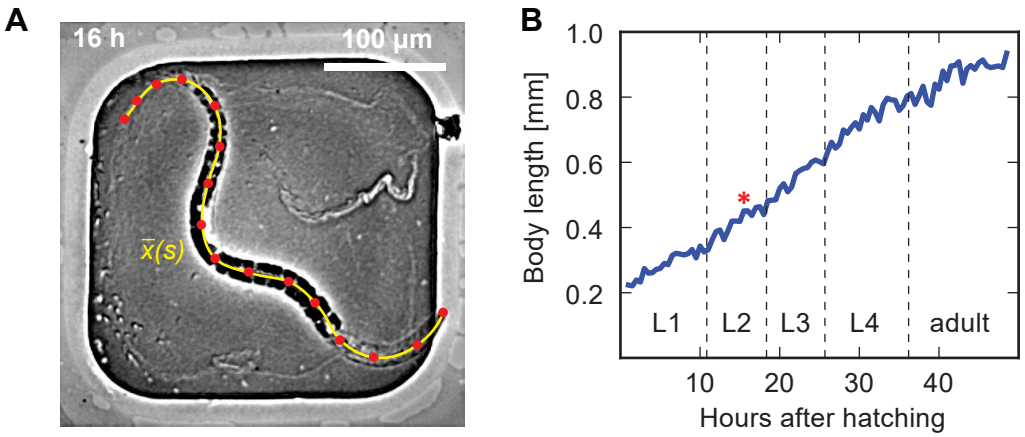

Figure 2.6: Data analysis schematic and body elongation curve. (**A**) Example of a single spline curve $\overline{x}(s)$ (yellow line) fitted over manually selected points along the body axis (red dots). Time stamp represents hours after hatching (**B**) Example of body elongation curve (blue line) over time for a single animal. Red asterisk represents the length of the timepoint shown in panel A. Dashed vertical lines represent the timing of each ecdysis events.

We then used this data set to directly measure two markers of developmental progression. We first annotated the times of hatching, marked by the emergence of the L1 larva from the egg, and ecdysis, evident by the appearance of the old cuticle inside the chambers. Due to the short time interval used, we could detect ecdysis events with 5 minutes accuracy. Second, we measured the body length extension as a function of time (Fig. 2.6A) using a custom graphical user interface implemented in Python. For each timepoint, we manually selected 10-20 points on the animal's center line and subsequently fitted a spline curve $\overline{x}(s)$ to these points, with s being the arc length of the spline curve along the anteroposterior axes. Body length in a single timepoint was given by the length of the spline curve $\overline{x}(s)$ (Fig. 2.6B).

2.3.2 Wild-type larval development

In order to test whether food availability can affect *C. elegans* development, we created microfabricated chambers with different dimensions that can contain a variable amount of OP50 bacteria. I will refer to these chambers as *small* (190x190x10 μm^3), *medium* (250x250x20 μm^3) and *large* (290x290x25 μm^3) chambers (Fig. 2.7A). We observed that, independent of chamber dimensions, newly hatched larvae remained constrained in the chambers over the course of the experiment (Fig. 2.7B).

As chambers of different dimensions can contain different amounts of OP50 bacteria, smaller chambers might not contain enough food to sustain development over all four larval stages. Indeed, only when using medium or large chambers, did larvae develop into adults and were eventually able to lay eggs inside the chambers (Fig. 2.7B, last image). In contrast, we observed developmental arrest of animals confined in the small chambers. This is likely a consequence of the limited food supply.

To test whether body elongation agrees well with standard *C. elegans* culture conditions, we compared body length of animals grown in microchambers with body length of animals cultured on standard NGM agar plates. Our setup is not temperature-controlled and, instead, we kept the temperature in the room at 20°C during all the experiments. However, when we measured the temperature in close proximity to the sample on the microscope, we found that the local temperature was 22°C. As *C. elegans* development is strongly dependent on temperature, we therefore performed the experiment on standard NGM agar plates in an incubator at 22°C. Briefly, adult animals were transferred on a large NGM agar plate. After about 2 hours, each of the laid eggs was transferred on a single small NGM agar plate spotted with OP50 bacteria. Hatching time was detected by visual inspection of the plates every 10 minutes. Animals were then manually tracked and imaged every 12 hours, and body elongation was measured as previously described.

We found that body elongation of animals grown in medium and large chambers is comparable to that of animals grown on NGM agar plates (white dots in Fig. 2.8A,B). Moreover, the body length at the start of each larval stage agreed well with previous measurements [109] (Fig. 2.8D), suggesting that *C. elegans* larvae develop normally

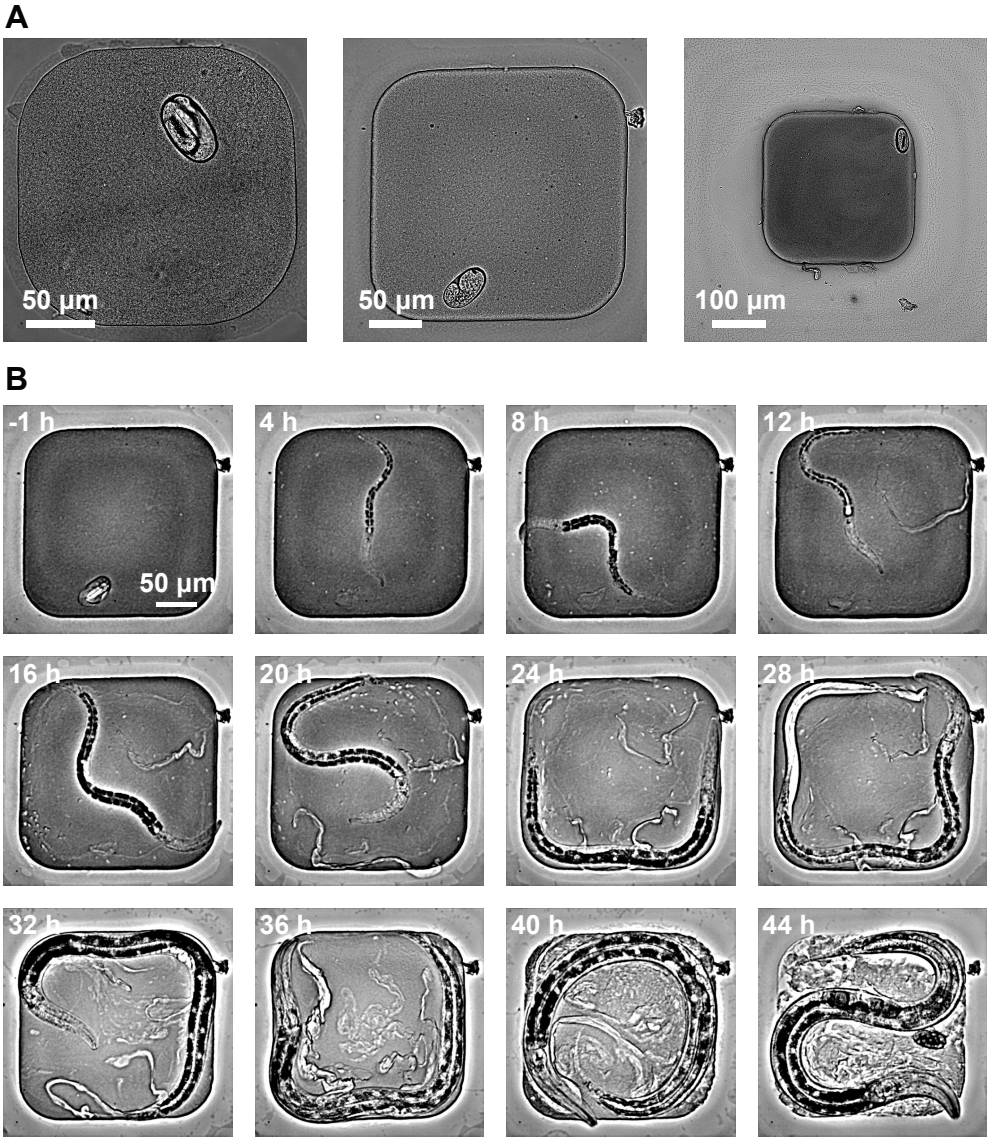

Figure 2.7: Example of a typical data set. (**A**) Comparison between the different chamber size used in this chapter. Left: *small* chambers (60X magnification), center: *medium* chambers (40X magnification), right: *large* chambers (20X magnification). Compare main text for actual dimensions. (**B**) Collection of frames from a movie of a single animal imaged in medium chambers. Time stamps represent hours after hatching.

over the full post-embryonic development inside the medium and large chambers. Therefore, we conclude that these chambers can be used to study developmental processes spanning all four larval stages (Chapters 3, 4). However, to perform such experiments we chose medium chambers instead of the large chambers because they fit in the field of view of the camera when imaged with a 40X magnification objective, which has a higher N.A. (1.30) compared to the 20X objective (N.A = 0.45) needed

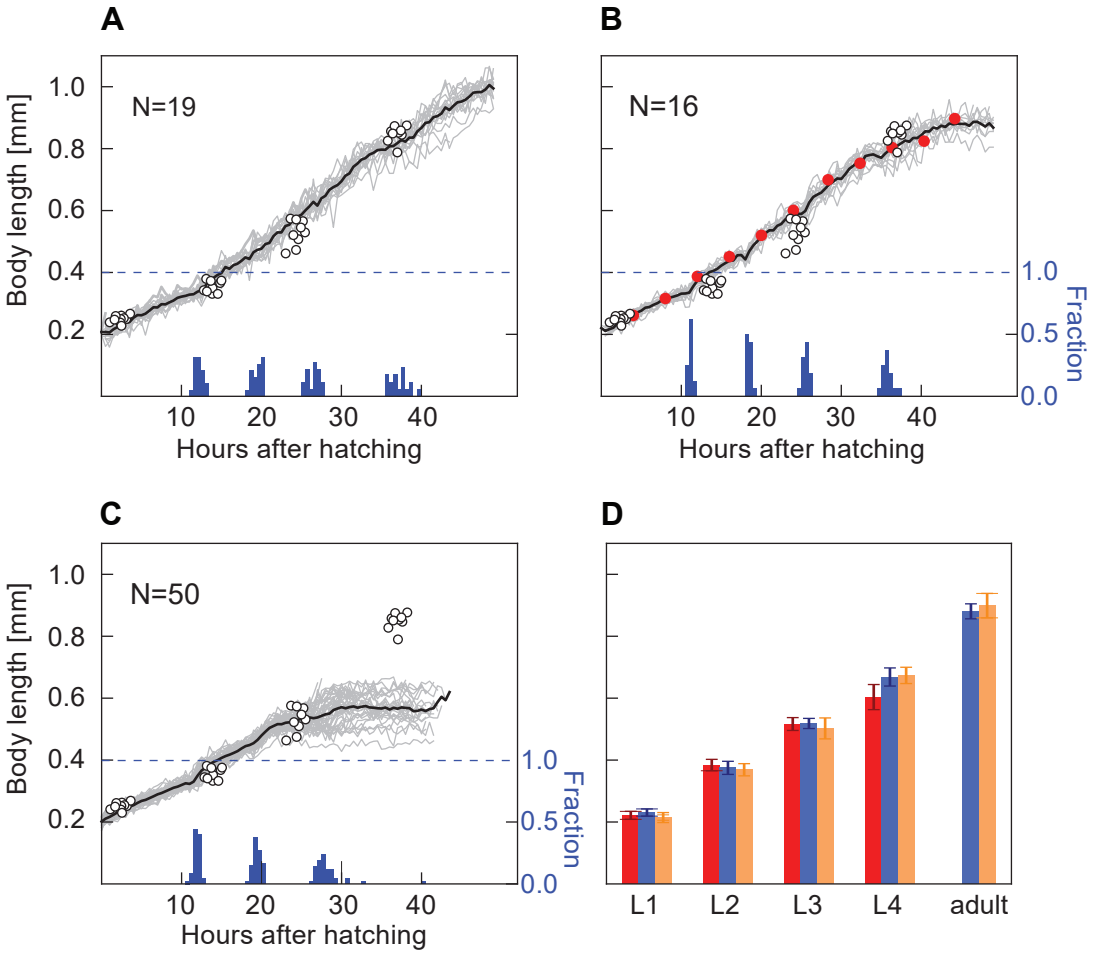

Figure 2.8: Development of wild-type *C. elegans* in microchambers. Body elongation curve as a function of time for individual animals (grey curves) and population average (black curve) for animals confined in large (**A**), medium (**B**) and small (**C**) chambers. Blue histograms show the fraction of animals undergoing ecdysis event at a particular time. In all panels, white dots represent body elongation of animals grown on standard NGM agar plates. Red dots in panel B represent the images shown in Fig. 2.7B. (**D**) Population average of body length at the beginning of each larval stage for the small (red bars), medium (blue bars) and large (yellow bars) chambers. Error bar respresents standard deviation. Animals in the small chambers failed to complete L4, therefore no body length could be measured for young adults.

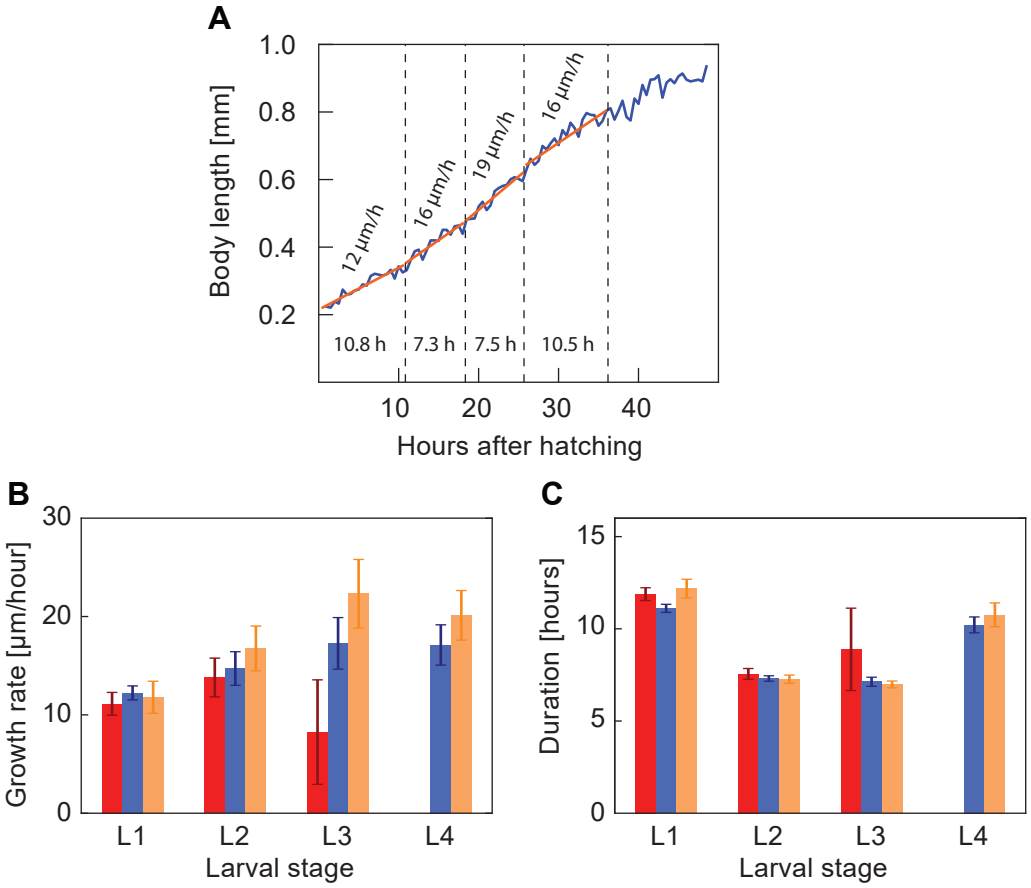

Figure 2.9: Growth rate and larval duration analysis. (**A**) Larval-dependent linear fit (red line) of the body elongation curve shown in Fig. 2.8. Vertical dashed lines represent the times of each ecdysis event. Numbers next to the linear fit represent the growth rate for each larval stage. Numbers along the X axis represent larval stage durations. Population average of growth rate (**B**) and larval stage duration (**C**) for each larval stage for the small (red bars), medium (blue bars) and large (yellow bars) chambers. Error bar represents standard deviation. Animals in the small chambers failed to complete L4, therefore no growth rate and L4 duration could be measured.

to image large chambers, and therefore higher resolution can be achieved.

When analyzing development in the small chambers, we observed that not all the animals were able to develop into L4 larvae, suggesting that at this stage of development food in the small chambers is limited. However, when comparing the body length of animals grown in the small chambers for the first three larval stages, we found that this agrees well with data obtained from animals grown on NGM agar plates and with previous results [109] (Fig. 2.8C). Moreover, body elongation curves showed only minor quantitative difference compared to the large and medium chambers (Fig. 2.8D). The ability of *C. elegans* larvae to grow normally in the

small chambers during the first two larval stages can be used to study developmental processes at higher resolution because these chambers fit in the field of view of the camera even when imaged with higher magnification and higher N.A. objectives (60X, N.A.=1.40, Fig. 2.7A). Specifically, we used the small chambers to study the stochastic AC/VU decision process (Chapter 5).

None of the animals grown in the small chambers completed the forth larval stage, therefore we were not able to detect body elongation of young adult animals grown in these chambers (Fig. 2.8 C,D). The observations that under limited food conditions only a fraction of animals developed into L4 and none of them developed into young adults are in agreement with previous studies [110, 111] that showed how animals tend to arrest development directly after an ecdysis event if no food is available: when *C. elegans* larvae enter a new larval stage, they stop growing if no food is available. As, for most of the animals, food is still available in the small chambers at the beginning of the L3 stage, the developmental program continues and animals grow into L4 animals. However, when animals enter L4, the small chambers are completely depleted of OP50 bacteria, and the animals undergo developmental arrest.

The analysis suggested that our setup also has the potential to study how growth depends on food availability. Therefore, we decided to quantitatively test how the growth rate of individual larvae in the small chambers is affected by the limited food supply. Even though we have already shown that body length of animals in small chambers at beginning of each larval stage agrees with previous studies and with data from larger chambers, it is still possible that food availability affects the growth rate of *C. elegans* larvae. Studies on development in liquid culture using variable bacterial concentrations were previously performed, and it was found that growth rate indeed depends on bacterial concentration [64]. To test whether this is the case in our microfabricated chambers, we performed a linear fit to the body elongation curve at each larval stage (Fig. 2.9A). The slope of the fitted line represents the larval stage-dependent growth rate of individual animals, here measured in micrometers per hour. When comparing the population average of the growth rate and of the duration of each larval stage for the different chamber dimensions we observed that, for the first two larval stages, there is no significant difference between the different chambers (Fig. 2.9B,C). This finding suggests that bacterial concentration in microchambers of different dimensions is similar during the first two larval stages. However, we found that animals grown in small chambers show lower growth rate compared to animals grown in medium and large chambers in the third larval stage (Fig. 2.9B). Moreover, the duration of the third larval stage in small chambers is on average longer than that in medium and large chambers (Fig. 2.9C). Therefore, small chambers affect growth rate and larval stage duration in an opposite manner, which results in the normal body length at the beginning of the fourth larval stage (Fig. 2.7D). This observations suggest that developmental transitions between larval stages are triggered by body size rather than by the duration of the larval stages, as was shown in previous studies [64].

2.3.3 Animal-to-animal variability

We found significant animal-to-animal variability, both in timing of ecdysis and body length extension rate (Table 2.2). Similar variability in timing of ecdysis was observed recently in *C. elegans* larvae development in liquid culture [64]. Such variability is not dependent on the chamber size, suggesting that, until food is exhausted, development is not affected by the amount of food available at the hatching time. However, it remains unclear whether the source of such variability we measured is intrinsic to *C. elegans* development or is due to some extrinsic factors, such as local temperature changes between different chambers. To test whether food availability is responsible for the animal-to-animal variability, it would be interesting in the future to perform time-lapse microscopy of animals grown in fluorescently labeled bacteria. In this way, the bacterial concentration could be directly measured by fluorescence microscopy. On the other hand, to avoid temperature-dependent variability, an obvious solution would be to implement a system to more precisely control the temperature in close proximity of the sample.

		L1	L2	L3	L4
Duration [hours]	average	12.18	7.27	6.98	10.76
	standard deviation	0.51	0.22	0.18	0.64
Growth rate [μm hour^{-1}]	average	11.80	16.75	22.31	20.12
	standard deviation	1.63	2.28	3.49	2.52

Table 2.2: Animal-to-animal variability. Average and standard deviation of growth rate and larval stage duration for all the wild-type animals.

2.4 Conclusions

In this chapter, we have presented a novel technique to perform time-lapse microscopy of motile *C. elegans* larvae. The main advantage of this technique is the ability to follow freely moving and feeding animals over developmental time scales.

The silicon mold we used to prepare microchambers in polyacrylamide hydrogel can be re-used many times, making it a cost-efficient tool. Moreover, our microfabricated chambers in polyacrylamide hydrogel could be expanded with an additional channel in PDMS on top. This channel can be used to control temperature by flowing cooling liquid or to rapidly exchange chemicals, for instance to induce gene expression. In addition, the design of our microfabricated chambers is easily adaptable to imaging of other nematode strains.

Our optical setup relies on a commercial microscope and only few optical components to expand and guide the laser beam. The illumination system allows us to acquire sharp images at high signal-to-noise ratio even with short exposure times, in the order of 1-5 ms. The imaging system, and specifically the synchronization between camera, piezo stage and lasers, ensures that the acquisition of a full volumetric image is efficiently performed in approximately half a second. Therefore, in most of the cases, larvae motility is typically negligible when comparing different images in the same stack. Although the transparency of *C. elegans* body does not require a optical sectioning technique, the use of wide-field illumination affects the theoretical resolution along the axial direction. In particular, higher axial resolution might be needed in conditions of significant out of focus light, for instance when fluorescently labeled cells are in close contact to each other. In fact, it is in principle possible to extend our setup and use optical sectioning techniques capable of imaging a large field of view with high frame rate. For instance, the temporal focusing approach discussed in Section 1.4 [74] is the most promising technique for fast, large field of view, high resolution imaging. It would be interesting to test the applicability of such technique to our setup.

Our results on wild-type animals suggest that development of *C. elegans* larvae is normal as it agrees well with previous results on body length and growth rate. We conclude that the medium chambers (250x250x20 μm^3) can be used to study developmental processes spanning all four larval stages (Chapters 3, 4), while small chambers (190x190x10 μm^3) can be used to study processes happening during the first two larval stages (Chapter 5). While larger chambers can fit in the field of view of the camera using a 40X magnification objective, a 60X magnification objective can be used to image smaller chambers. Therefore, as higher magnification objectives typically have higher N.A., we can use the small chambers to improve light collection when fluorescently labeled cells are particularly dim (Chapter 5).

Moreover, our results on body elongation and larval stage duration of animals grown in small chambers suggest that larval stage transitions are triggered by body size rather than by larval stage duration. The ability of our technique to image animal growth in a controlled environment could be used to study the effect of food availability on development in a quantitative manner. In addition, as our technique is also capable of high resolution imaging, it represents a unique tool to study the same effects on single cells within the animal body. For instance, in the future it would be interesting to analyze the effect of food availability both at the whole-organism and at the single cells levels within the same animal.

3

Lineaging of stem-cell-like divisions

This chapter is part of the following publication:
"N. Gritti, S. Kienle, O. Filina and J. S. van Zon,
Long-term time-lapse microscopy
of *C. elegans* post-embryonic development.
Nat. Commun. 7:12500 doi: 10.1038/ncomms12500 (2016)."

Cell division and differentiation are the hallmark of developmental progression. During the development of multi-cellular organisms, the ability of undifferentiated stem cells to generate differentiated cells is crucial to populate tissues and organs. To achieve this, stem cells have to remain in a proliferative state over the course of development and the number of differentiated cells and stem cells must be precisely balanced throughout development. How the required tight coordination between cell division and differentiation is achieved, is an active area of research. It is of paramount importance to understand how stem cells divide, renew themselves and differentiate as these processes are closely related to many relevant medical topics, such as tissue repair and regeneration, aging and cancer [112].

Proliferation and differentiation of stem cells are ensured by two types of division. During a symmetric division, a mother stem cell gives rise to either two identical undifferentiated cells, therefore increasing the number of stem cells in the organism, or to two differentiated cells, therefore decreasing the number of stem cells. Asymmetric divisions instead result in one stem cell and one differentiated cell. Therefore, when an asymmetric division occurs, the number of stem cells in the organism remains constant. Two distinct mechanisms of differentiations have been

proposed for the regulation of stem cell differentiation. In some cases, stem cells lay in a niche that provides environmental cues to keep cells undifferentiated. In this case, it is only upon migration outside the niche that cells start the differentiation program [113, 114]. In other cases, asymmetric divisions result in the inhomogeneous partitioning of the cellular components, therefore one of the new born daughter cells lacks the stem cell potential and is capable of differentiation without the need of additional external cues [115].

Stem cell dynamics has been studied in many different organisms, from the fruit fly *D. melanogaster* to mammals [116, 117]. However, due to the large number of cells involved, it is often difficult to identify single cells and investigate their behavior. Thanks to its simple body plan, transparency and invariant lineage, *C. elegans* is an ideal system to study stem cell biology. Moreover, the easy genetics of *C. elegans* makes the identification of the key regulators of division and differentiation simpler compared to larger organisms. There are two main examples of stem cell systems in *C. elegans*: germline cells and seam cells. While the germline is a complex system in which cells continously proliferate in a niche throughout the entire life of the animal [118, 119], seam cells represent a simplified model to study stem cell behavior. During development, seam cells resemble the stem cell behavior, as they both maintain and expand the seam cell pool through asymmetric and symmetric divisions. However, after development is complete, seam cells terminally differentiate. Therefore seam cells are not true stem cells, but they nevertheless represent a convenient model system to study stem cell-like division patterns [120].

The 20 seam cells of a newly hatched animal are arranged in 2 rows on the opposite sides of the body along the longitudinal axis (Fig. 3.1A). Seam cells divide and differentiate in a stem-cell like manner over the ~48 hours of development and are important for the formation of hypodermal cells and neurons. Divisions of seam cells can be symmetric or asymmetric and follow a stereotypical lineage (Fig. 3.1B). In most cases, during an asymmetric division, the posterior daughter remains a seam cell while the anterior daughter fuses to the hypodermal syncytium, the skin of the animal [121]. This pattern of asymmetric divisions repeats itself during each larval stage. However, in the second larval stage some of the seam cells undergo a symmetric division resulting in two seam cells, thereby increasing the number of seam cells in the larva. After the last larval stage, the remaining seam cells terminally differentiate to become hypodermal cells. The seam cell lineages are invariant and have been determined when the full post-embryonic lineage of *C. elegans* was first reconstructed [122].

Recent studies have started to elucidate the molecular mechanisms that control seam cell division and differentiation. The division cycle and terminal differentiation are regulated by micro RNAs (miRNAs). Mutations of these miRNAs cause errors in the temporal regulation of division and differentiation. For instance, certain mutations cause the symmetric divisions to already occur in the first larval stage while others cause the first asymmetric division to be repeated identically for all the

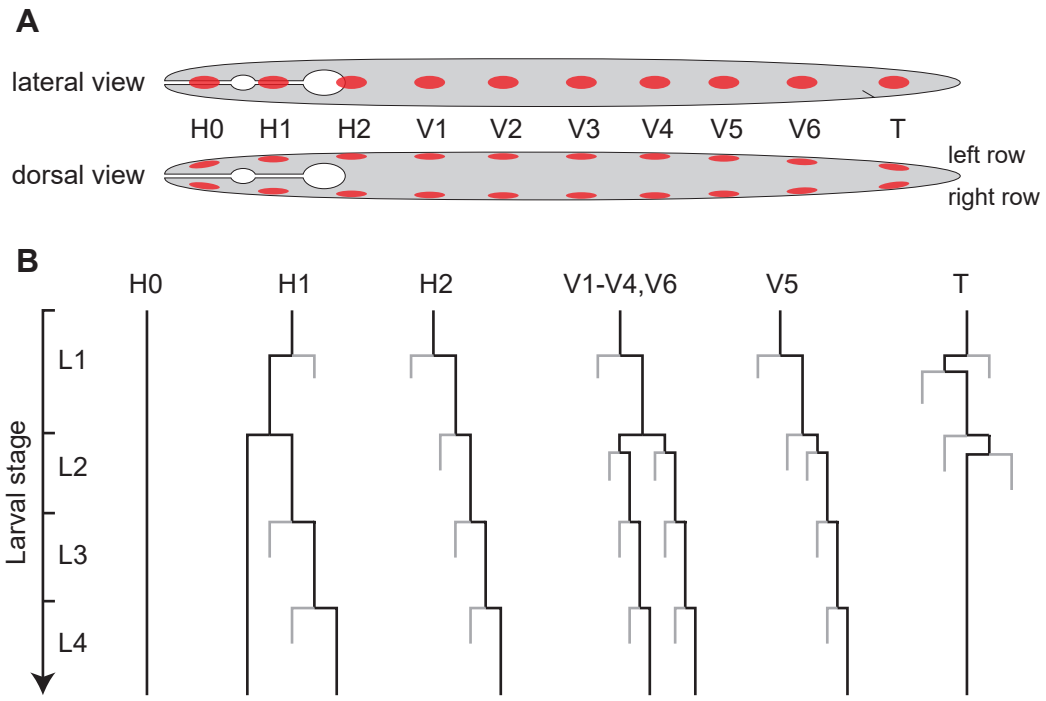

Figure 3.1: Schematic of *C. elegans* seam cells. (**A**) Location of seam cells (red dots) in a newly hatched *C. elegans* larvae. (**B**) Stereotypical lineage of seam cells (black lines) during larval development. Grey lines represent differentiated cells resulting from an asymmetric division.

larval stages [123]. Wnt signaling also plays an important role in the execution of asymmetric divisions, as mutations in the Wnt signaling pathway affect the final number of seam cells [124, 125].

Despite these recent advances, many aspects of the seam cell division process still need to be elucidated in order to reach a comprehensive understanding of this developmental process. On the one hand, the molecular mechanisms that regulate and execute seam cell divisions remain poorly understood. To elucidate these mechanisms, full lineage analysis in mutant animals is necessary to provide a better understanding of the effect of genetic mutations on the seam cell division pattern. On the other hand, seam cell division and differentiation are important to progress through development, as differentiated cells form the skin of the animal at the end of each lethargus stage. Therefore, the seam cells need to divide at the correct developmental time. However, even though the overall lineage is known, the exact timing of divisions, as well as any animal-to-animal variability in timing, has never been measured at high temporal resolution. That is due to the fact that, because of its long duration, the full lineage of seam cells has never been imaged in an individual animal.

With our time-lapse technique, however, it is possible to image single live

animals over the full post-embryonic development. We therefore examined whether it was possible to follow the cell division and differentiation dynamics of all the seam cells in individual animals using fluorescent reporters to follow individual cells.

In this chapter, I first introduce the experimental design and the data analysis technique used to identify single cells and to extract division timing (Section 3.1). Then, I analyze the temporal sequence of seam cell divisions (Section 3.2). We find that seam cells follow a particular division sequence with a difference in the timing of division between different seam cell lineages. In Section 3.3, to further demonstrate the power of our approach, we use our technique to perform the seam cell lineage analysis in a mutant strain. In particular, we study a mutant that exhibits a variable number of seam cells in the adult stage. In this mutant, we find that errors in the symmetry of the seam cell divisions are more likely to happen in specific lineages and larval stages. This result shows that stage- and lineage-specific differences exist in the regulation of the seam cell division and differentiation.

3.1 Experimental design and data analysis

To visualize seam cells in living animals, we used a strain, *wIs51[SCMp::GFP]*, that carries a fluorescent seam cell marker. This marker is convenient for single seam cell detection, as it is expressed only in the nuclei and is seam cell-specific. *C. elegans* animals were synchronized as described in Section 2.1.2. We used 250 x 250 x 20 μm^3 microchambers with a 40X magnification objective (N.A.= 1.30) and imaged animals with a 20 minutes time interval during the full post-embryonic development. We used 100 mW laser power with 5 ms exposure time, which resulted in high signal-to-noise ratio.

We acquired images in two different channels (red LED and 488 nm laser), which resulted, as already mentioned in Chapter 2, in ~50 Gb of data for a single animal. We therefore needed to develop custom written Python software to deal with such a considerable amount of data. We used the trans-illumination images to exactly locate the animal within the microchamber and to detect ecdyses events. For each timepoint, we obtained an average projection of the trans-illumination stack. We used these average projections to manually select 10-20 points along the anteroposterior (A-P) axis of the animal and we fitted a spline curve $\overline{x}(s)$ to those points, similar to the method discussed in Chapter 2 (Fig. 3.2A). The spline curve was then used to obtain a computationally straightened stack for both the trans-illumination and fluorescence channels. To do so, orthogonal segments with 25 µm length were drawn from each pixel belonging to the spline curve (Fig. 3.2B). In this way, for each point of interest with coordinates $\overline{r} = (x, y)$ in the original image, the A-P position s' was given by the value of the minimum distance to the spline curve

$$s' = \min_{s} \|\overline{x}(s) - \overline{r}\| \tag{3.1}$$

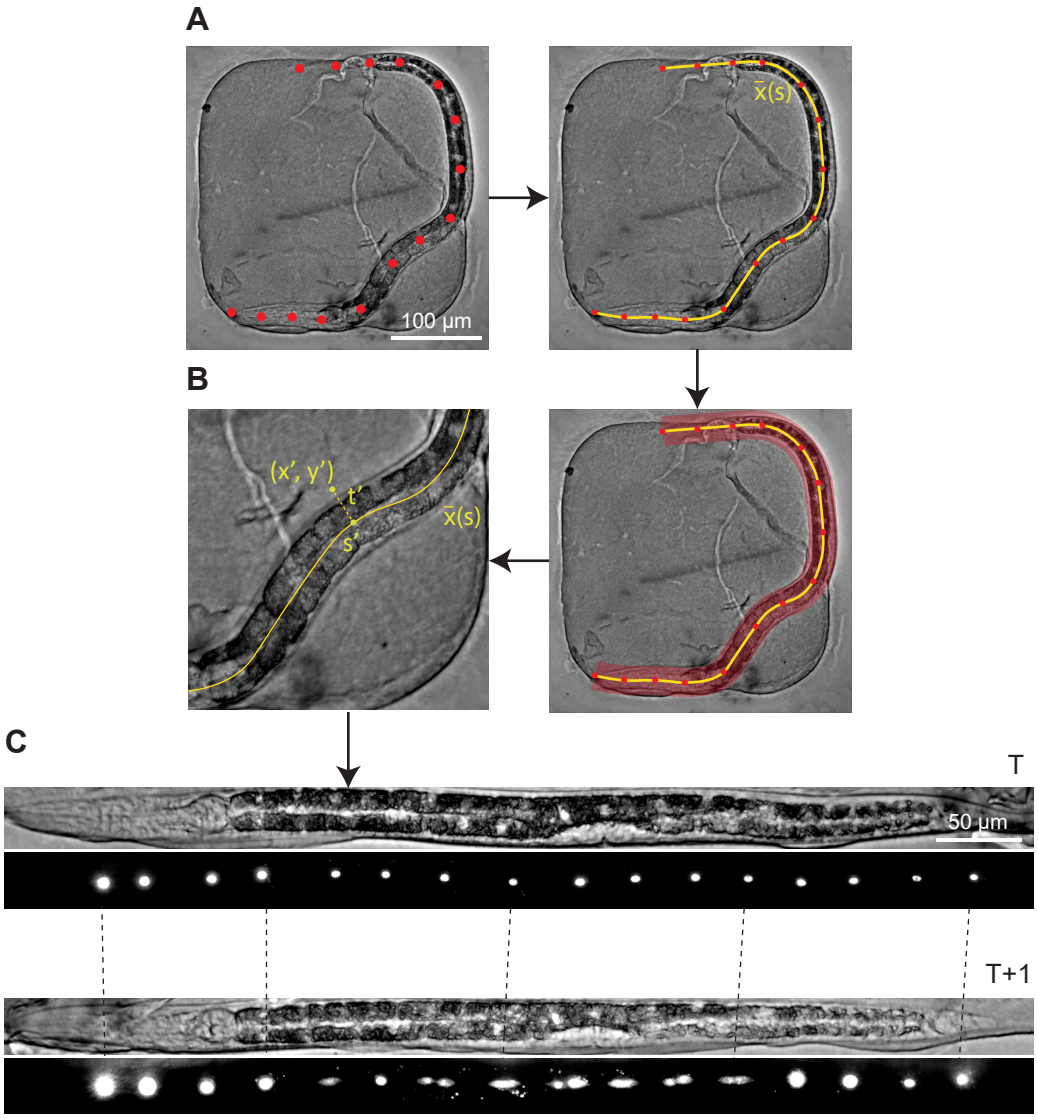

Figure 3.2: Data analysis of seam cell marker strain. . (**A**) Example of a single frame from a time-lapse movie. Red dots are manually selected along the A-P axis of the animal, a spline interpolation is computed (yellow curve). (**B**) A 50 µm wide area around the spline curve is defined (red band). The A-P and D-V position of each pixel in the red area is computed. Values of the pixels in the straightened image are computed using 2D linear interpolation. For detail refer to main text and Section 4.1. (**C**) Computationally straightened images of both trans-illumination and fluorescence channels of a single animal for two subsequent timepoints. Dashed lines connects individual cells between the two timepoints in the fluorescence channel.

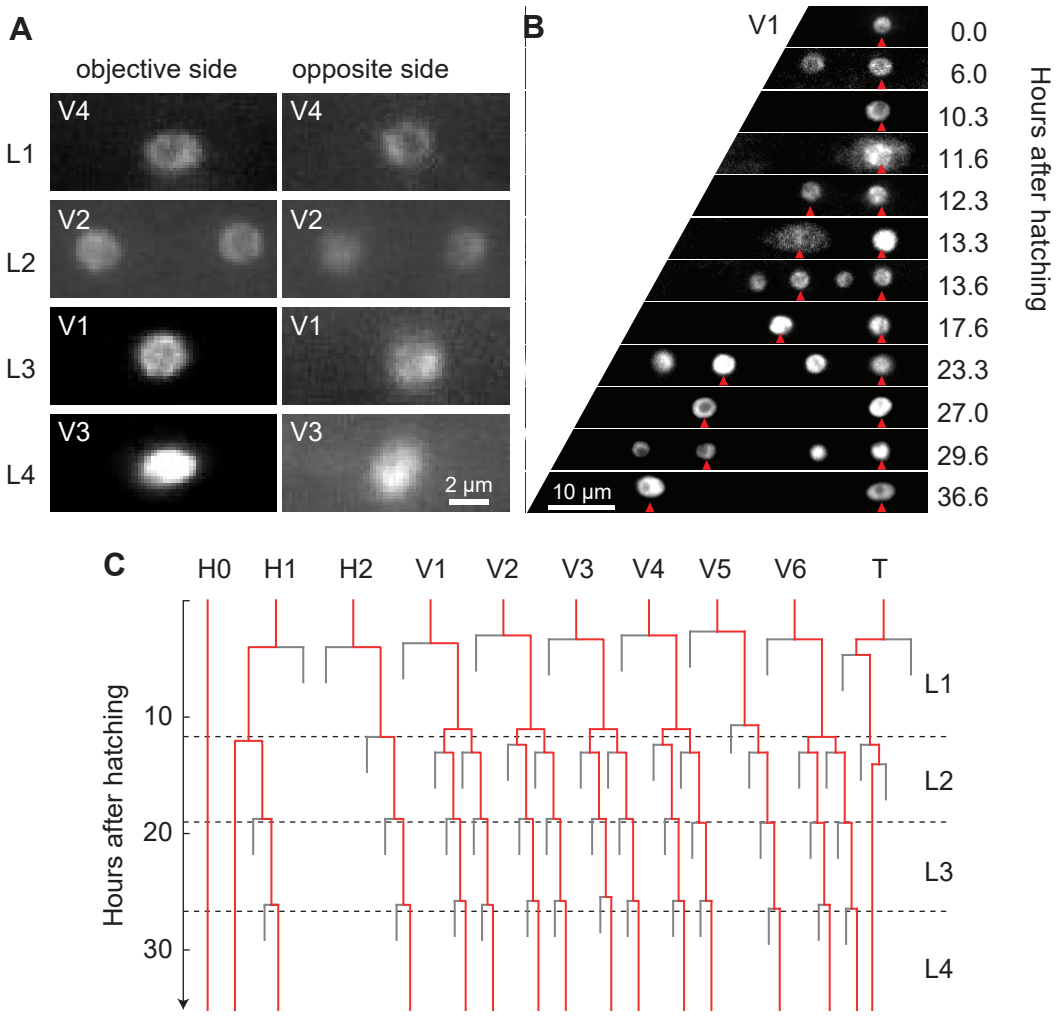

Figure 3.3: Imaging of single seam cells. (**A**) Example of single seam cells laying on the side closest to the objective (left column) and on the opposite side (right column) at different larval stages. (**B**) Image sequence of the V1 lineage in a single animal carrying the *wIs51 [SCMp::GFP]* nuclear seam cell marker. Seam cell nuclei are indicated by red arrows. Other nuclei belong to hypodermal cells. Images were computationally straightened and aligned to the posterior-most seam cell. (**C**) Example of seam cell lineages measured in a single animal. Red lines represent seam cells and grey lines differentiated cells. Dashed lines indicate time of ecdysis, separating the different larval stages, L1-L4. Divisions are indicated at the exact time of occurrence, with 20 min resolution.

while the dorsal-ventral (D-V) position t' was given by

$$t' = \pm \|\overline{x}(s') - \overline{r}\| \tag{3.2}$$

where the sign of t' is defined such that the D-V position of the anus is negative. The pixel value in the position (s', t') was then given by 2D linear interpolation with all neighboring pixels, which will be described in detail in the next chapter (Section 4.1). Animals were aligned with anterior to the left and posterior to the right. The straightening of each animal is not strictly necessary but makes cell identification much more convenient, especially to recognize cells between two consecutive timepoints (Fig. 3.2C). Moreover, using cropped and straightened images drastically reduced the amount of data to be handled during the cell annotation procedure.

Straightened fluorescence images were used to detect single seam cells and cell divisions. Starting from the first mother cell in the lineage, for instance V5, daughters were labeled with names V5.a and V5.p, according to the position along the A-P axis. Data were collected in a Python compatible format, and additional Python scripts were used to draw cell lineages. The first appearance of two daughter cells, for instance V5.a and V5.p, was recognized as the timing of division of the correspondent mother cell.

Because *C. elegans* larvae usually lay on their side, one row of seam cells is close to the glass surface, while the other is located deep inside the sample, i.e. far from the objective. Therefore, the fluorescence signal emitted by the seam cells far from the objective is degraded by light scattering in the animal's tissue. Nevertheless, the marker was bright enough to visualize cells on both sides of the body over all four larval stages (Fig. 3.3A).

From the straightened images of a single animal, it was possible to build single cell movies and follow the seam cells as they go through the cell division cycles. At particular timepoints, we could identify cells in different stages of the cell cycle. Cells in the G_1 and S phases showed bright nuclear fluorescence (Fig. 3.2C and Fig. 3.3B). Cells in the M phase were recognized by the diffused fluorescence in the whole cell (Fig. 3.3B, 13.3 hours after hatching), likely due to the breakdown of the nuclear envelope, which allows the fluorescent proteins to diffuse into the cytoplasm. Finally, cell differentiation was recognized thanks to the seam cell-specific property of the fluorescent marker used: whenever a seam cell undergoes an asymmetric division, the marker in the differentiated cell is lost within a few hour, while the new seam cell retains nuclear fluorescence (Fig. 3.3B). Therefore, we could unambiguously assign the fate of each daughter cell. In this way, we could reconstruct the full lineage for all the seam cells. We measured the timing of division in hours after hatching (Fig. 3.3C).

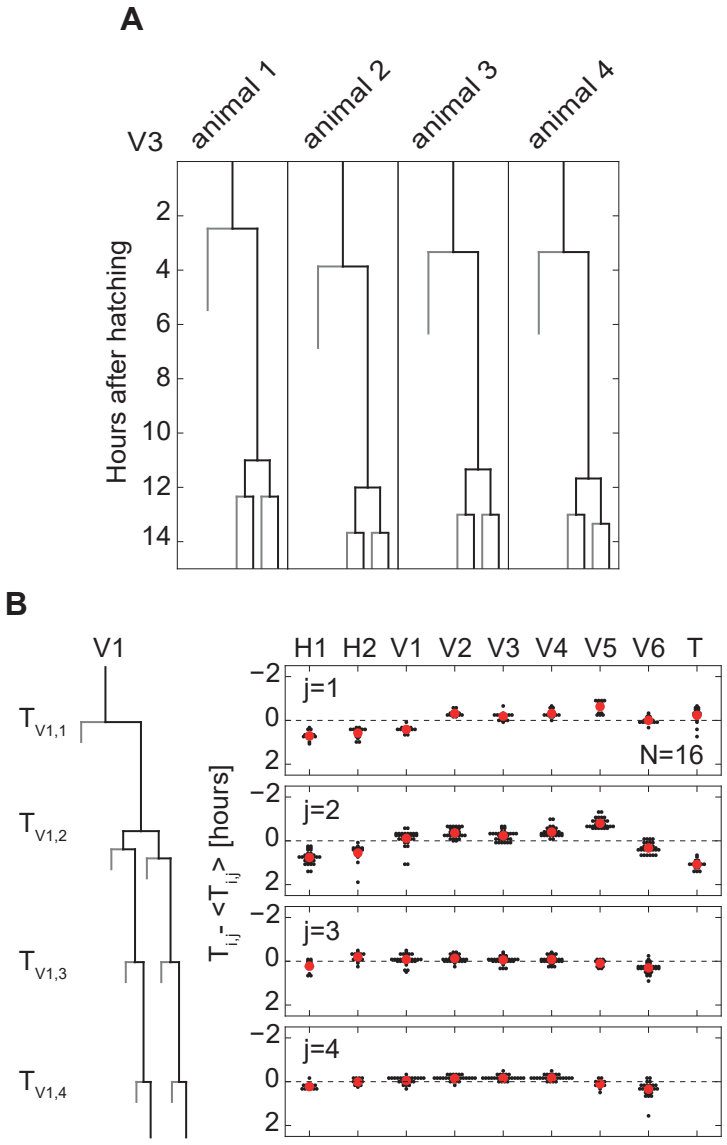

Figure 3.4: Analysis of seam cell division timing. (**A**) Animal-to-animal variability in cell division time in the first three divisions of the V3 lineage. (**B**) Analysis of cell division timing. For each seam cell division i, we plot the relative division time $T_{i,j} - \langle T_{i,j} \rangle$ (black markers), where $T_{i,j}$ is the cell division time and $\langle T_{i,j} \rangle$ is the division time averaged over all nine lineages, H1-T, on both sides of the animal. Also shown is the relative division time averaged over all animals (red markers).

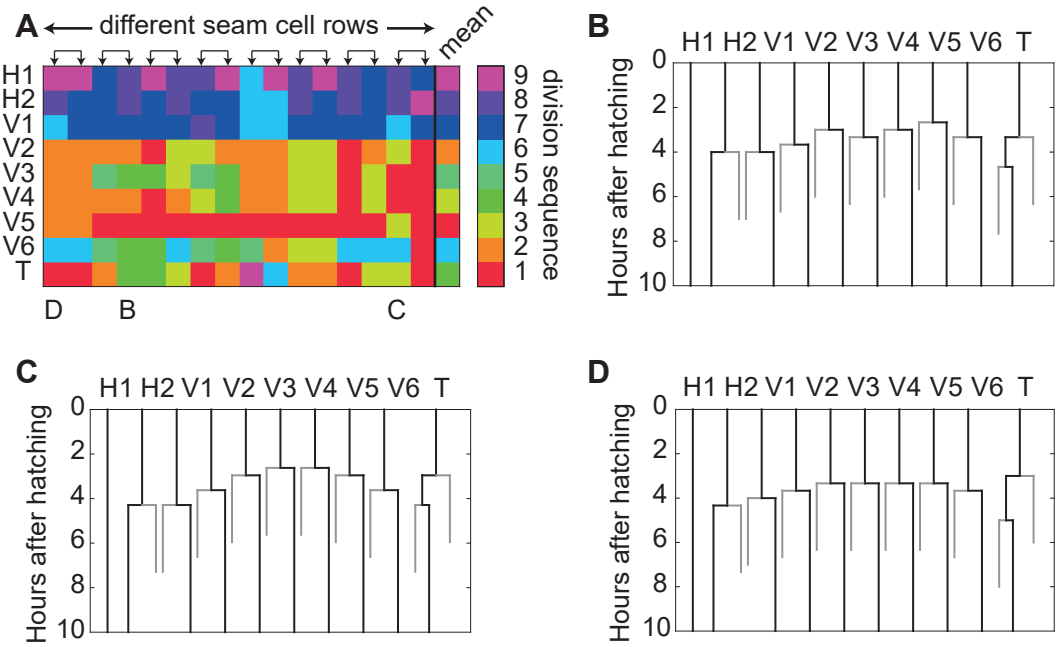

Figure 3.5: Variability in the sequence of seam cell divisions. (**A**) Colormap showing the sequence of seam cell divisions in the L1 larval stage, for two sides (left/right) in N=8 animals. Seam cell rows belonging to the same animal are connected by black solid arrows. Cells are color-coded according to the division sequence. The last column represents the mean division sequence. The columns labeled with (B), (C) or (D) correspond to the lineages shown in the corresponding panels. (**B**), (**C**), (**D**) Examples of animals with a typical (B) and atypical sequence (C,D) of seam cell divisions in the L1 larval stage. In Panel (B), V5 divides first. In Panel (C), V3 and V4 divide simultaneously 20 minutes before V5. In Panel (D), T divides first.

3.2 Timing of seam cell divisions

The ability to detect the exact time of division relative to the hatching time allows us to study both systematic differences in timing between seam cell lineages and variability within each lineage between different animals. To study the animal-to-animal variability, we performed our lineage analysis for multiple animals. We measured the division time variability of each cell lineage and found a typical standard deviation of ~30 minutes, with largest differences in timing of division of ~2 hours (Fig. 3.4A).

To study the cell-to-cell variability, we measured, at each division cycle, the division time of each individual seam cell with respect to the average division time of all the seam cells within the same animal, according to the equation:

$$\Delta T_{i,j} = T_{i,j} - \langle T_{i,j} \rangle \tag{3.3}$$

where $T_{i,j}$ is the actual time of division of the seam cell i at the division cycle j and

$\langle T_{i,j} \rangle$ is the average time of division of all the seam cells at the division cycle j:

$$\langle T_{i,j} \rangle = \frac{\sum T_{i,j}}{N_j} \tag{3.4}$$

where N_j represents the number of mother seam cells in the division cycle j. A negative or positive value of $\Delta T_{i,j}$ corresponds to a cell that divided earlier or later than the average time of division within the same animal, respectively. For the second larval stage, we considered the first symmetric division.

We found systematic cell-to-cell variation, with seam cells of different lineages following a specific division sequence (Fig. 3.4B). In particular, the seam cells at the center of the body, i.e. V2, V3 and V4, divided on average earlier than cells on the outer parts, i.e. H1, H2, V6 and T. We also found that such a systematic variability is more pronounced in the first two division cycle, while at later stages seam cell divisions are more synchronized. The fact that cell divisions are more synchronized during the third and fourth larval stages compared to earlier stages is, to our knowledge, a novel observation. This suggests that there are stage-dependent differences in the temporal regulation of the seam cell divisions.

The main deviation from the stereotypical division sequence is V5, which typically divided first in the L1 larval stage (Fig. 3.5A). This suggests that the temporal regulation of V5, at least in the first division cycle, is different from that of the other seam cells. However, we observed significant variability around the mean division timing, leading to deviations from the average division sequence. In 3 cases out of the 16 lineages analyzed, we observed another seam cell dividing before V5 in the L1 stage (Fig. 3.5B,C,D).

In conclusion, our technique improves the classical lineage analysis technique, making it semi-automated and more high-throughput. The ability to precisely detect the timing of division and quantitatively measure its variability can contribute towards understanding the temporal cues that trigger seam cell divisions.

3.3 Mutant with variable seam cell lineage

In the previous section, we showed that our technique improves lineage analysis of wild type animals and allows the quantification of animal-to-animal and cell-to-cell variability. Next, we tested whether our technique could aid the analysis of mutations that impact the seam cell lineage. Mutants in which the seam cell lineage deviates from the stereotypical lineage are important to examine the regulatory mechanisms that drive the proper division of the seam cells. However, lineage analysis of mutant strains is challenging due to the laborious manual work that the standard approach requires [122]. This represents a bottleneck already for the analysis of mutant strains with an invariant phenotype, i.e. strains in which cell division errors occur in a reproducible manner. However, lineage analysis of mutants in which cell lineages are impacted in a variable manner is virtually impossible because the exact cell

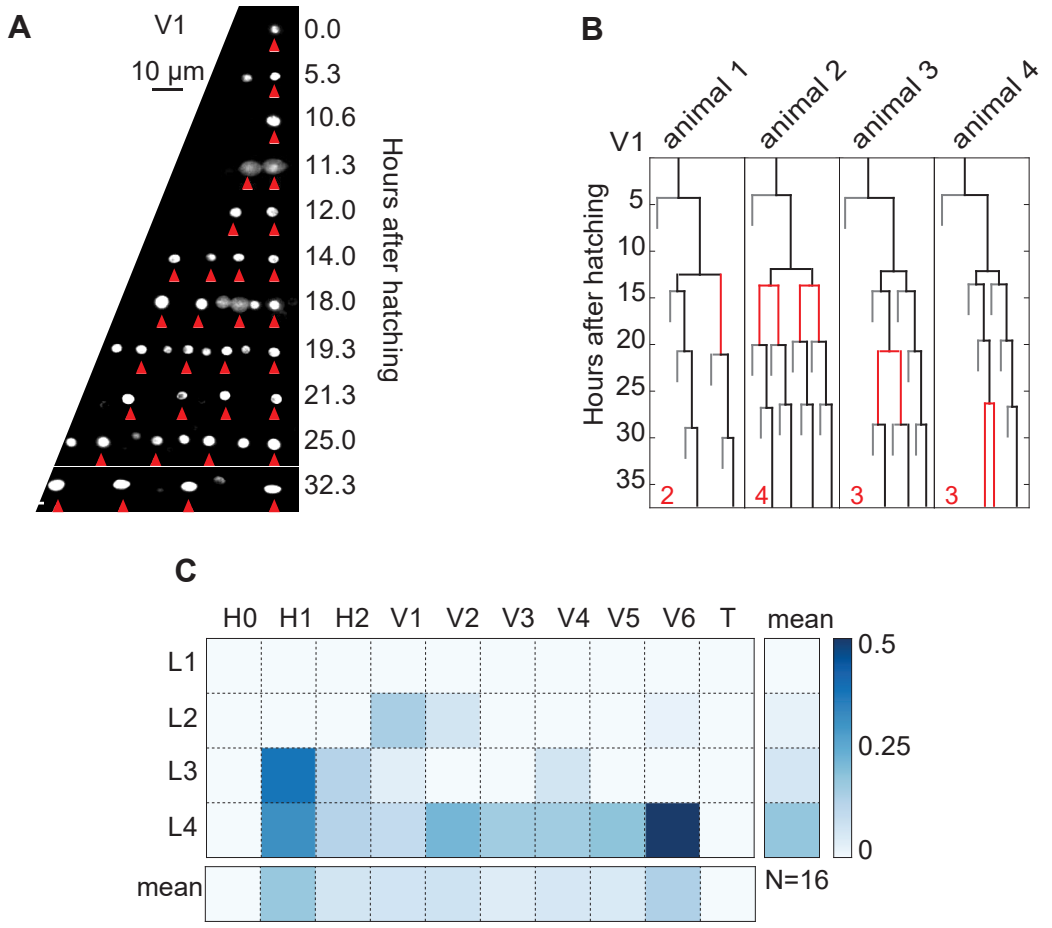

Figure 3.6: Seam cell lineaging in mutant animals. (**A**) Errors in the V1 lineage in the MBA48 seam cell lineage mutant carrying a *wIs51[SCMp::GFP]* nuclear seam cell marker. Time is indicated in hours after hatching. Red markers indicate the seam cells in the lineage. The third division (14 hours after hatching) is symmetric instead of asymmetric for both seam cells, resulting in four seam cells at the L4 stage. (**B**) Representation of the division errors observed. Red lines represent lineage errors. The final number of seam cells is indicated for each lineage in red. The lineage for animal 2 corresponds to the images shown in Panel (A). (**C**) Occurrence of lineage errors. For each lineage and larval stage, color represents the probability of errors. Also shown are the mean probability of errors for each larval stage (right-most column) and each lineage (bottom row).

lineages are different between animals and therefore many animals need to be analyzed in order to obtain a full understanding of the effects of such mutations. In this section we show that, with our technique, variable lineage mutants can be analyzed and therefore the effect of these mutations on the seam cell lineages can be determined.

In collaboration with the group of Michalis Barkoulas (Imperial College London),

we focused on an uncharacterized mutant strain, MBA48. Previous analysis showed that this mutant exhibits variable seam cell numbers in young adult animals. Indeed, we found that the number of seam cells in young adults was always higher than expected (average and standard deviation of 19.8±2.0), suggesting that symmetric divisions are more frequent than in wild type animals (Fig. 3.6A).

To determine the origin of variability in MBA48 mutants, we reconstructed the full seam cell lineage for multiple animals and compared it with its wild type counterpart. We found that mistakes can be grouped in two distinct categories: seam cells (i) often perform a symmetric division instead of an asymmetric division (62 times out of 456 divisions) and (ii) instead of performing an asymmetric division, occasionally seam cells do not divide (9 times out of 456 cell divisions) (Fig. 3.6B). The first error has a clear effect on the seam cell lineage outcome: the number of seam cells is doubled and this can be observed with the screening technique previously used by an increase of the number of seam cells in young adult animals. However, the second error, i.e. the case in which a seam cell does not divide when it is supposed to, does not affect the number of seam cells and therefore cannot be observed by counting the number of seam cells in a particular larval stage (Fig. 3.6B).

In order to study the spatial and temporal distribution of such errors, we scored the probability of a single error as a function of larval stage and seam cell lineage. To do so, we defined a lineage error as the first point at which the (sub-)lineage deviated from the wild-type lineage. For instance, if an additional seam cell was erroneously generated, we did not score for errors in the sublineage produced by that seam cell. To achieve that, we calculated the probability $P(l,s)$ of a lineage error occurring in seam cell lineage l at larval stage s as follows. For each seam cell i, for example V2.pp, in animal w, we assigned a division class $d_i = 0,1,2$ for no division, symmetric division and asymmetric division, respectively. We did so for all seam cells in wild-type (WT) and mutant (M) animals. The error probability is then given by

$$P(l,s) = \frac{\sum_w \sum_{i \in C_{l,s}} (1 - \delta_{d_i^{WT}, d_i^M})}{\sum_w \sum_{i \in C_{l,s}} 1} \tag{3.5}$$

where $\delta_{n,m}$ is the Kronecker delta and $C_{l,s} = C_{l,s}^{WT} \cap C_{l,s}^{M}$ is the list of seam cells that are present in both the wild-type lineage and the mutant animal w.

We found that division errors occurred randomly, but predominantly in the L3 and L4 larval stages and were distributed unequally over the different lineages, most strongly impacting the H1 and V6 lineages (Fig. 3.6C). These results show that the regulation of seam cell divisions is stage- and lineage-dependent. The sort of analysis used in this section can help elucidate the role of specific genes in the stage- and lineage-dependent regulation of the seam cells.

3.4 Conclusions

Here, we have shown that our time-lapse microscopy technique can aid the study of cell lineage regulation in *C. elegans*. We have shown that our technique greatly improves the standard cell lineaging approach, which relies on the manual observation of single larvae, in two crucial aspects. First, our technique improves the throughput, as multiple animals can be followed in parallel. Second, while with the standard technique cells are typically followed for few hours due to the laborious manual imaging, with our automated imaging technique it is possible to follow the lineage during the full post-embryonic development. This makes it possible for the first time to study a variety of aspects related to cell division and differentiation processes. Such studies include, but are not limited to, the analysis of the mechanisms by which temporal cues coordinate cell divisions, the quantification of the robustness of these mechanisms, and the analysis of the regulation of symmetric and asymmetric divisions in stem cell lineages.

In this chapter, we applied our technique to the analysis of the seam cell lineage, a simplified model system for the study of stem cell behavior. First, we performed full seam cell lineage analysis of multiple wild-type animals. We found that, while each seam cell follows a stereotypical division pattern, the timing of each division shows high animal-to-animal variability. This result suggests that, while robust mechanisms have evolved that ensure a reliable overall outcome of the seam cell lineages, the timing of each seam cell division is subject to variability. It would be interesting in the future to examine whether this variability is intrinsic to the seam cell lineages or whether a global and noisy temporal cue is responsible for the variability in the timing of division of each seam cell. Despite the high cell-to-cell variability, we found that cells in the same animal follow a stereotypical division sequence, with some seam cells dividing on average earlier than others. Such systematic differences are more pronounced during the first 2 larval stages, while at later stages all seam cell divisions are more synchronized. These observations suggest that there are stage- and lineage-dependent differences in the temporal regulation of the seam cell divisions. It would be interesting to study the underlying mechanisms responsible for such systematic variability, and elucidate whether each seam cell is subject to a different temporal cues or whether each seam cell responds in a slightly different way to the same global temporal cue.

Finally, we applied our technique to the analysis of mutants in which random division errors occur in the seam cell lineages. The fact that mutations exist which cause random errors in the lineage of the seam cells, suggests that single seam cells are subject to noise and that wild-type animals developed a mechanisms to suppress it in order to reach a robust and stereotypical lineage. Therefore, the lineage analysis of variable lineage mutants can provide insights on the robustness of stem-cell like division patterns. We found that, for the particular mutant we chose, only two kinds of errors can happen: either a seam cell does not divide at a particular division cycle, or a seam cell performs a symmetric division instead of an asymmetric one. Using

the ability of our approach to pinpoint when and in which lineage errors occur, we found that errors are not randomly distributed, but instead are more likely to happen at late larval stages and in particular seam cell lineages. This result suggests that there are stage- and lineage-dependent differences in the regulation of the seam cell division and differentiation. In collaboration with the group of Michalis Barkoulas (Imperial College London), we aim to apply our technique to other mutants and therefore elucidate the role of some key regulators in the seam cell division and differentiation processes.

4

Quantitative analysis of oscillatory gene expression

This chapter is part of the following publication:
"N. Gritti, S. Kienle, O. Filina and J. S. van Zon,
Long-term time-lapse microscopy
of *C. elegans* post-embryonic development.
Nat. Commun. 7:12500 doi: 10.1038/ncomms12500 (2016)."

In the context of multicellular organisms, dynamic gene expression is often exploited by single cells to perform a variety of different actions in a coordinated manner. Such actions can be performed once during the entire life of the organisms, or can be repeated multiple times. An example of the first class is metamorphosis of insects, that is regulated by specific hormones and a complex signaling cascade [126]. Examples of repeated events span over a wide range of length and time scales, from the cyclic heart beat to the sequence of cell divisions in a developing organism.

When a particular task has to be repeated multiple times, a natural way to provide a temporal cue is to exploit oscillatory gene expressions with a period correspondent to the time interval between two consecutive events. A classical example of such a biological timer is the circadian clock, a widespread mechanism designed to adjust the behavior and metabolism of many organisms to the day and night cycle [127, 128].

Gene expression oscillations not only control rhythmic behavior of cells, tissues and organs in adult organisms, but are also exploited in the context of development.

For example, gene expression oscillations are used to regulate the interactions between different components of the Notch and Wnt signaling pathway to control the segmentation clock of many organisms. The segmentation clock in most vertebrates species, for instance, is regulated by spatial waves of gene expression travelling from head to tail which lead to the periodic formation of the somites in the spinal cord [129].

The correct timing of these cellular events is important to ensure proper development. Therefore, a control mechanism capable of synchronizing the gene expression in multiple cells is necessary. As these developmental events are so important for the survival of the organism, such molecular mechanisms are designed to strongly suppress molecular noise. Some biological timers, such as the circadian clock, have been extensively studied, resulting in a detailed understanding of the control mechanisms involved [130]. However, how timing in development is regulated is still open questions.

C. elegans development is a highly dynamic and remarkably robust process which involves a variety of events. Thanks to its fast development, simple body plan, body transparency and availability of mutants with abnormal timing of development, *C. elegans* is an ideal model system to study developmental timing. In particular, the effect of genetic mutations on single-cell events have been subject of extensive studies. For example, certain mutations cause seam cells to skip larval stage-dependent divisions, or to repeat divisions occuring in early larval stages also in later larval stages. Because of their atypical developmental progression, such mutants were termed *heterochronic* [131].

A striking characteristic of *C. elegans* development is its cyclical nature. At the end of each of the four larval stages, animals enter the lethargus stage, during which the molting occurs. At the end of the lethargus stage, animals undergo an ecdysis event, i.e. they shed the old cuticle, and enter the next larval stage. The mechanisms that regulate these developmental events have been subject of extensive studies. Since a larval stage starts at the moment of ecdysis, one expects that proper temporal cues instruct the relevant cells to execute the molt. Moreover, a molting clock has to be coordinated between different cells in the animal's body in order to undergo ecdysis events at the right developmental time, i.e. when all cells are ready to execute the next larval stage program. Recently, some genes have been recognized that are responsible for the correct coordination of the developmental clock controlling the molting cycle [132]. Such genes are called *molting cycle genes*. For instance, it has been shown that *lin-42*, a gene related to the circadian clock gene PERIOD, has an oscillatory expression dynamics and the deletion of this gene causes molts to occur in an arrythmic manner [133]. Moreover, it has been shown that the activation of this gene is important for many aspects of seam cell divisions, from the timing of divisions, to their spatial arrangement and fate determination [134, 135].

Recent studies showed that ~20% of all detectable genes oscillate during development [136, 137]. It was found that most of these genes showed an oscillation

period of ~8 hours, compatible with a molting cycle function. Moreover, expression dynamics could be characterized using their phase, i.e. at what point in each larval stage the expression peak occurs. Hendriks et al. found that genes oscillate at all possible phases, suggesting that oscillations have multiple roles during larval stage development, rather than only in regulating the molt. Many questions regarding the origin and the functional role of these oscillatory gene expressions during development remain unanswered. In particular, what are the mechanisms responsible to generate and maintain these oscillations? Are the mechanisms involved in the circadian clock similar to those involved in the gene expression oscillations during *C. elegans* development? In particular, this question is motivated by the observation that the *C. elegans* gene *lin-42* is related to the circadian clock gene PERIOD.

Another interesting aspect is related to the dynamics of single genes. In particular, what is the variability in the time of the expression peak? Moreover, how uniform is the expression in the animal's body? In order to answer this question, the first necessary step is the characterization of individual gene expression oscillations. To this end, one needs (i) to quantify the variability in the period and amplitude of the oscillations in single live animals with high temporal resolution and (ii) to quantify the animal-to-animal variability by studying the expression dynamics in multiple animals. However, so far, expression levels were quantified by measuring the fluorescence expression of transcriptional reporter strains, or by RNA-sequencing and quantitative PCR of a large number of developmentally synchronized animals.

In this chapter, we show that our new technique is capable of measuring gene expression levels by quantifying fluorescence intensity in single animals throughout the full post-embryonic development. Therefore our technique represents an ideal tool to quantify the dynamics of such oscillations. For instance, it is possible to measure the period, the level of synchronization throughout the whole body and the animal-to-animal variability of oscillatory gene expressions. We apply our technique to two different genes that have been previously shown to oscillate: *mlt-10* and *wrt-2*.

First, we analyze the expression dynamics of *mlt-10*, a nematode-specific gene required for proper molting, as well as for body shape determination, locomotion and reproduction [138]. The protein MLT-10 is broadly expressed in the hypodermis during the molt. We characterize the dynamics of *mlt-10* expression using a transcriptional reporter and we quantify the animal-to-animal variability in the timing of the oscillation peaks. We find that *mlt-10* oscillations in the posterior part of the animal's body are slightly delayed compared to the anterior part. Moreover, we find high variability in the timing of the expression peak relative to hatching. However, the timings of such peaks are highly correlated with the closest ecdysis events.

Next, we focus on the expression dynamics of another oscillatory gene, *wrt-2*. The protein WRT-2 is required for proper molting, normal growth and locomotion [139]. *wrt-2* is exclusively expressed in the seam cells, and hence it represents a great opportunity to test whether our technique is capable of fluorescence quantification

in single cells. Recently, *wrt-2* expression was found to oscillate during the third and fourth larval stages [136]. To test whether oscillations occur at all four larval stages, we analyze the dynamics of *wrt-2* expression in individual animals using a transcriptional reporter in which green fluorescent protein is targeted both to the seam cell nuclei and membranes. Measuring the total fluorescence intensity in the nuclei, we confirm that oscillations occur in all the larval stages and are synchronized between all the seam cell lineages. Similar to the dynamics of *mlt-10*, we find that the timing of oscillations are highly variable but also strongly correlated with the ecdysis events. These results suggest that the developmental timing is affected by noise, and that the timing of *mlt-10* expression, *wrt-2* expression and ecdysis are impacted by a common noise source.

4.1 Experimental design and data analysis

To visualize gene expression levels of both *mlt-10* and *wrt-2*, we used transcriptional reporter strains. To study *mlt-10* expression we used the strain *mgIs49[mlt-10p::GFP-PEST]*, previously used to characterize *mlt-10* expression dynamics at the population level [140], in which GFP is broadly expressed in the hypodermis. To study *wrt-2* expression we used the strain *heIs63[wrt-2p::H2B::GFP, wrt-2p::PH::GFP]*, in which GFP is targeted to both the seam cell nucleus and membrane [141]. Since we want to quantify expression during the full post-embryonic development, we used medium chambers (250 µm x 250 µm x 20 µm) to provide enough food to sustain development until adulthood. We used a 40X magnification objective (N.A. 1.3) and imaged animals with a 20 min time interval until few hours after the last ecdysis event.

We used fluorescence time-lapse microscopy to image the fluorescence signal in the animal's body at each time point. We computationally treated our images to quantify the fluorescence intensity along the anteroposterior (A-P) and dorsal-ventral (D-V) axis of the animal and in single cells. This step of the data analysis was common for both strains and similar to the analysis described in Section 3.1. I will now describe in detail the algorithm used to obtain images that are independent of the body shape of the animal at each particular time-point.

To obtain images that are independent of the body shape of the animal, we performed an average projection of the transmission stacks, and manually selected 10-20 points along the A-P axis of the animal (Fig. 4.1A). As described in the previous chapter, the manually selected points were fitted to obtain a spline curve $\overline{x}(s)$, which then represented the A-P axis. At each point along the A-P axis, the D-V axis was defined by orthogonal segments 50 µm long (Fig. 4.1B). The (x', y') coordinates of each point P' in the original image are then converted into the (s', t') coordinates in the A-P and D-V reference system. The A-P position s' of each point P' was given by

$$s' = \min_s \|\overline{x}(s) - \overline{r}\| \tag{4.1}$$

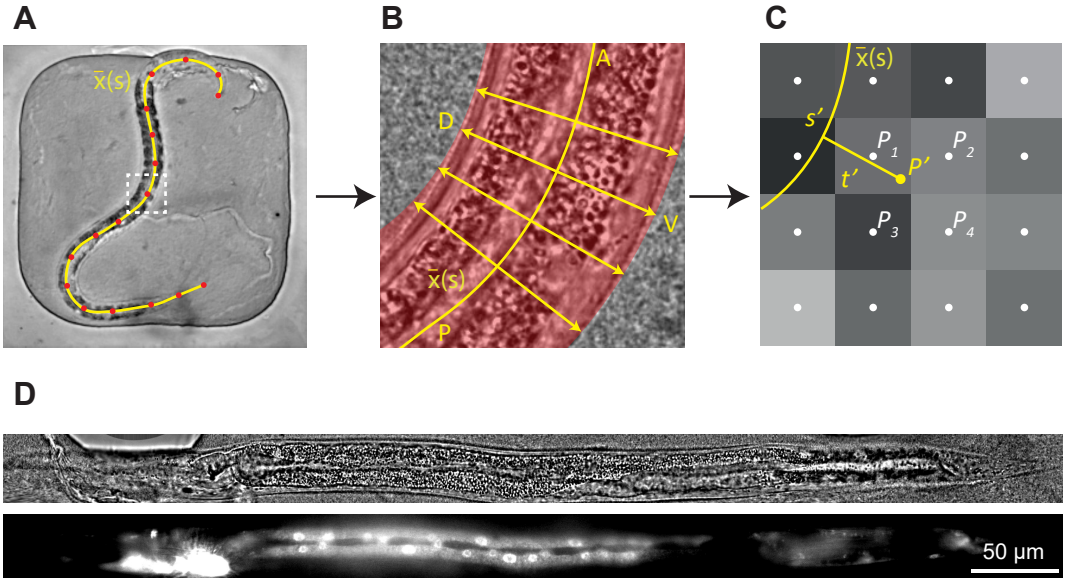

Figure 4.1: Straightening algorithm. (**A**) Average projection of a single transmission stack of a *mgIs49[mlt-10p::GFP-PEST]* animal. Red dots indicate manually selected points, yellow line indicates the spline curve fitted to the red dots. (**B**) Detailed view of the image enclosed by white dashed square in Panel A. Orange region indicates the part of the image containing the animal. Yellow arrows in the orthogonal direction to the spline curve indicate the dorsal-ventral (D-V) direction of the animal's body at different anteroposterior (A-P) positions. (**C**) Schematic overview of the interpolation algorithm. P_i indicates pixels in the (x, y) coordinate system. P' indicates the pixel in the (s, t) coordinate system. As P' does not coincide exactly with any of the pixels P_i, the value of P' was determined by 2D interpolation of the neighboring pixels P_i. (**D**) Single computationally treated image corresponding to the animal shown in Panel A. Top image: transmission illumination, bottom image: fluorescence intensity.

while the dorsal-ventral (D-V) position t' was given by

$$t' = \pm \|\overline{x}(s') - \overline{r}\| \tag{4.2}$$

where $\overline{r}$ represents the coordinates (x', y') of the point P' and the sign of t' is defined such that the D-V position of the anus is negative. In this way, all the post-processed images will result with the anterior side to the left and the ventral side in the bottom of the image. In order to maintain the same pixel size between the original image and the post-processed image, we sampled the spline curve and the orthogonal segments in such a way that the distance between each consecutive point is exactly the dimension of one pixel in the original image.

The collection of points obtained was then used as a grid for all the images in the original stack. The original coordinates (x', y') of point P' are not integers, therefore we assessed the pixel value in the position P' using the values in the neighboring pixels $P_1(x_1, y_1)$, $P_2(x_1, y_2)$, $P_3(x_2, y_1)$, $P_4(x_2, y_2)$ (Fig. 4.1C). To this

end, we performed a 2D linear interpolation according to the equation:

$$I(P') = \frac{1}{(x_2 - x_1) \cdot (y_2 - y_1)} [x_2 - x', x' - x_1] \begin{bmatrix} I(P_1) & I(P_2) \\ I(P_3) & I(P_4) \end{bmatrix} \begin{bmatrix} y_2 - y' \\ y' - y_1 \end{bmatrix} \tag{4.3}$$

where $I(P)$ represents the value of the image I at the position P. The obtained value $I(P')$ was then used as pixel value in the position (s', t') of the corresponding image in the post-processed stack. In this way, we could reconstruct a stack independent on the body shape of the animal and in which the value of each pixel is a reliable approximation of the fluorescence intensity of the body of the animal (Fig. 4.1D).

4.2 Characterization of *mlt-10* expression

To study the dynamics of *mlt10* expression during post-embryonic development, we used the transcriptional reporter strain *mgIs49[mlt-10p::GFP-PEST]*, used previously to characterize *mlt-10* expression dynamics at the population level [140]. We were able to follow the expression dynamics of *mlt-10* for all four larval stages and observed a clear pulse in fluorescence intensity close to each ecdysis (Fig. 4.2).

To better visualize the dynamics of *mlt-10* expression, we calculated the fluorescence intensity along the A-P axis, by averaging the fluorescence signal along the dorsal-ventral (D-V) and left-right (L-R) axis. We then created a kymograph by aligning all the A-P fluorescence profiles as a function of time (Fig. 4.3A). We found that the fluorescence signal is not homogeneously distributed along the A-P axis but, for instance, the head of the animal showed a brighter fluorescence signal, particularly during the L4-to-adult molt. Moreover, we observed the strongest fluorescence signal close to the time of each ecdysis events (dashed horizontal lines). To better analyze these features of *mlt-10* gene expression dynamics, we analyzed the level of synchronization along the A-P axis and the timing of each peak compared to the subsequent ecdysis event.

4.2.1 Homogeneity of *mlt-10* expression

To test whether the *mlt-10* expression dynamics depends on the position along the A-P axis, we quantified the average fluorescence intensity at different positions along the body of the animal. In particular, the expression dynamics at different A-P positions was determined by integrating the fluorescence intensity over a region of 5% of body length, centered at positions at 25, 50 and 75% of body length (Fig. 4.3B). Indeed, we found that oscillatory dynamics appears uniform, that is, with a phase independent of the A-P position.

To analyze more quantitatively the synchronization along the A-P axis, we divided the body of the animal in 10 regions of 5% of body length, and performed a cross-correlation analysis for each pair. Cross-correlation is a powerful tool to determine whether two signals are delayed with respect to each other. For instance,

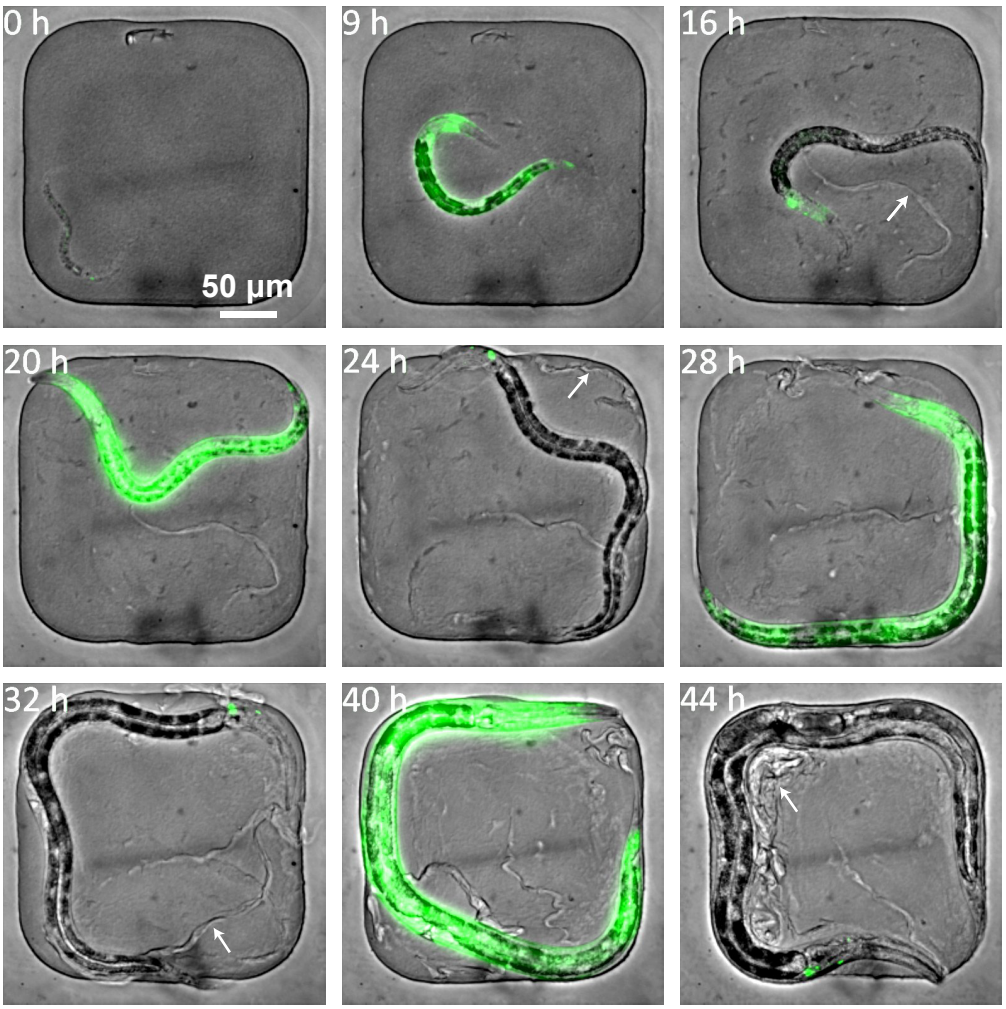

Figure 4.2: Visualization of *mlt-10* expression during the course of development. Images of a single animal at different time-points. Each image is the overlap of the transmission (grey scale) and fluorescence (green) signal. Time is indicated in hours after hatching. White arrows indicate the old cuticle that has been shed after the most recent ecdysis event.

given two timeseries belonging to different parts of the body, A and B, the cross-correlation function is defined as the convolution:

$$R(\tau) = \frac{\Big\langle \big(A(t) - \langle A \rangle\big)\big(B(t+\tau) - \langle B \rangle\big) \Big\rangle_t}{\sigma_A \sigma_B} \tag{4.4}$$

where $\langle A \rangle$, $\langle B \rangle$ represent the time average of the two signals, while σ_A, σ_B represent the standard deviation of the signals. The quantity R is then a function of the delay τ. The value τ' at which R reaches its maximum represents the characteristic delay of the two curves. Applied to our case, this delay can be interpreted as the time it takes

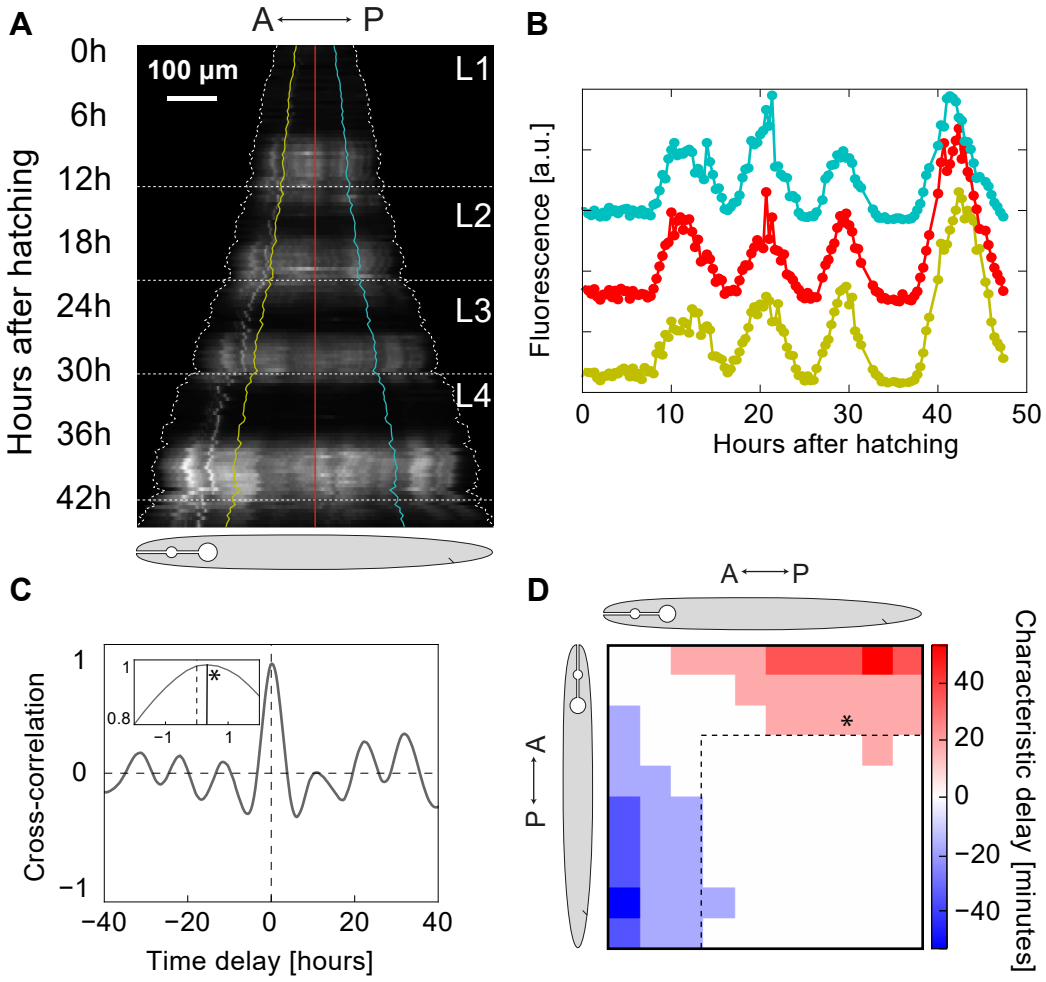

Figure 4.3: Synchronization of *mlt-10* expression in a single animal. (**A**) Kymograph of *mlt-10* expression along the A-P axis as a function of time in the *mgIs49[mlt-10p::GFP-PEST]* animal shown in Fig. 4.2. Dotted lines represent the position of head and tail, and horizontal dashed lines represent the times of each ecdysis events. Colored lines indicate the regions evaluated in Panel B. Larval stages are indicated on the right of the kymograph. (**B**) *mlt-10* expression oscillations at different A-P positions for the animal in Panel A. (**C**) Cross-correlation function for the yellow and cyan curves shown in Panel B. Inset: highlight of the curve around the zero lag time. Solid black line indicates the timing of the peak. (**D**) Timing of the highest peak of the cross-correlation function for all possible combination of A-P positions along the body of the animal shown in Panel A. Asterisk indicates the timing of the peak shown in Panel C. The region enclosed by the dashed lines indicates the body section along the A-P axis in which *mlt-10* expression is synchronized.

for the expression to move from the region A to the region B of the body. As an example, the cross-correlation curve between the regions at 25% and 75% of body length is shown in Fig. 4.3C. In this particular case, we found a characteristic delay of 20 minutes (Fig. 4.3C, inset).

When performing the cross-correlation analysis for each pair of positions along the body, we found that the posterior part of the body shows highly synchronized expression (Fig. 4.3D, white area in dashed box), and that this expression is slightly delayed compared to the anterior part of the body. The oscillations in the most posterior part of the animal are delayed up to 40 minutes with respect to the head of the animal.

4.2.2 Timing of the *mlt-10* expression oscillations

To quantify the animal-to-animal variability in *mlt-10* oscillations, we performed time-lapse imaging over 15 animals. To analyze the time series of *mlt-10* expression in the whole body, we calculated the average of the fluorescence intensity over the entire body for each time point. We found high variability both in the amplitude and the period of the oscillations, especially at late stages in development (Fig. 4.4A).

We then asked whether the times of the peaks of expression are correlated to the timing of the closest ecdysis event. Therefore, to detect the times of the four peaks, we first performed a Gaussian filter to smoothen the data. When applying a filter to a time series, each value of the filtered data is obtained by a weighted average of the original data. In our case, the weights follow a Gaussian function with a full width at half maximum $\sigma = 60$ minutes:

$$G(t') = \left\langle F(t) \cdot \frac{\exp\left[-(t-t')^2/(2\sigma^2)\right]}{\sqrt{2\pi}\sigma} \right\rangle_t \tag{4.5}$$

where $F(t)$ is the original time series, and $G(t)$ represents the filtered time series. From $G(t)$, we then computed the timing of each local maximum and compared it to the timing of the closest ecdysis event.

We observed significant animal-to-animal variability in the absolute timing of the *mlt-10* expression peak (Fig. 4.4A,B and Table 4.1). However, when the timing of the peaks were compared to the timing of the most recent ecdysis event, we found that variability was strongly reduced, suggesting that *mlt-10* expression dynamics is tightly correlated with the ecdysis events (Fig. 4.4C and Table 4.1). Therefore, while the absolute time of an ecdysis event is highly variable, its timing with respect to the *mlt-10* expression peak is much more predictable.

4.3 Characterization of *wrt-2* expression

The *mlt-10* gene is expressed in many cells. To test whether we could follow gene expression dynamics with single-cell resolution, we measured the expression level

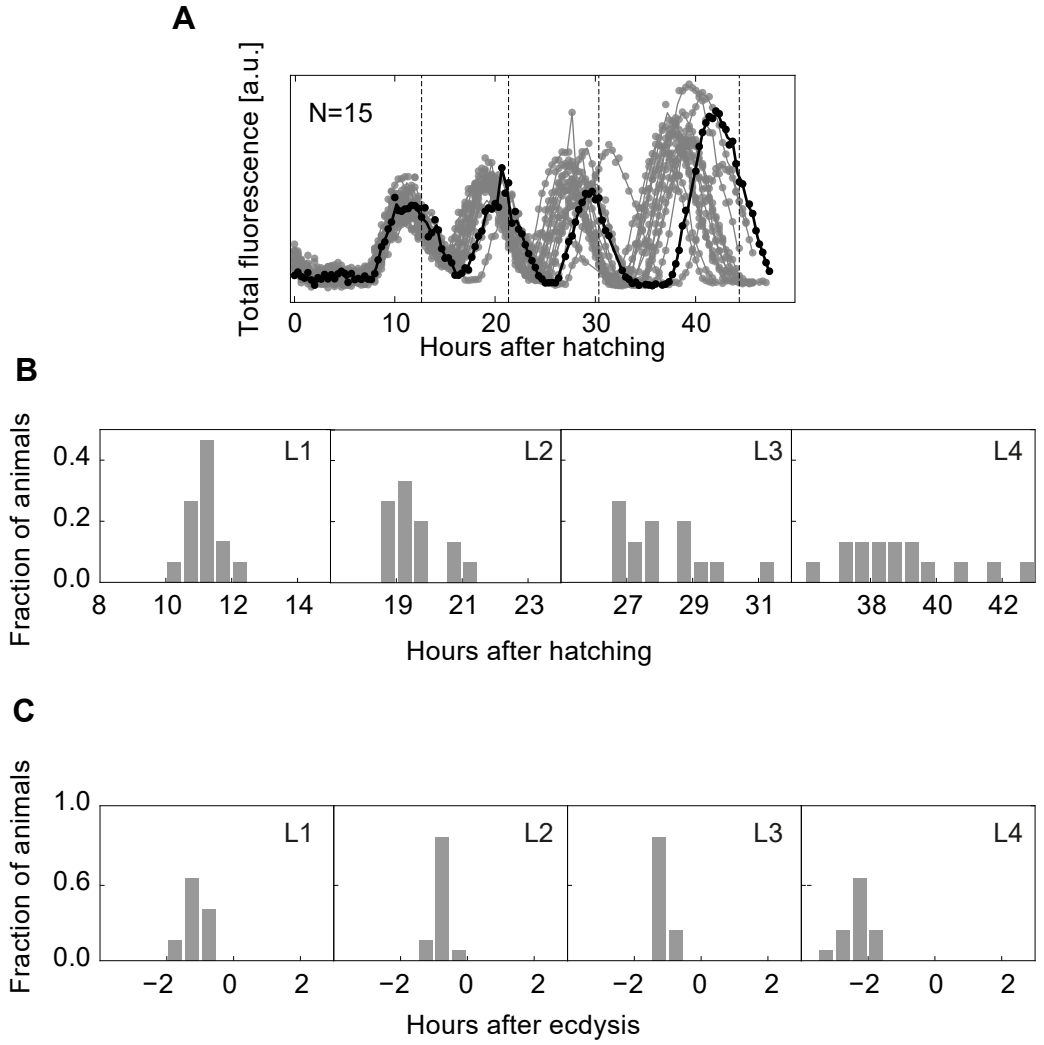

Figure 4.4: *mlt-10* expression in multiple animals. (**A**) *mlt-10* expression integrated over the entire animal as a function of time for N=15 animals. The *mlt-10* expression dynamics (black line) and time of ecdysis (dashed lines) are indicated for the animal shown in fig. 4.3. (**B,C**) Time distribution of the peaks in *mlt-10* (N=15) expression relative to (B) time of hatching and (C) time of the most recent ecdysis event.

of *wrt-2*, which is expressed exclusively in the seam cells [139]. To measure the expression level of *wrt-2*, we used the reporter strain *heIs63[wrt-2p::H2B::GFP, wrt2-p::PH::GFP]*, in which GFP is targeted both to the seam cell nucleus and membrane [141].

To analyze the *wrt-2* expression in single seam cells, we used the post-processed images to manually label the V1-V5 seam cells. As the size and shape of the nuclei changed over time, we used an image segmentation algorithm, the Otsu's method [108], on a 20 µm x 10 µm region around each cell to obtain a mask of the nucleus.

		L1	L2	L3	L4
Absolute timing [hours]	average	11.2	19.6	28.2	39.0
	standard deviation	0.5	0.8	1.3	1.8
Timing relative to ecdysis [hours]	average	-1.2	-0.8	-1.1	-2.3
	standard deviation	0.2	0.2	0.1	0.3

Table 4.1: Statistics of *mlt-10* expression peaks. Average and standard deviation of timing of *mlt-10* expression peaks (N=15).

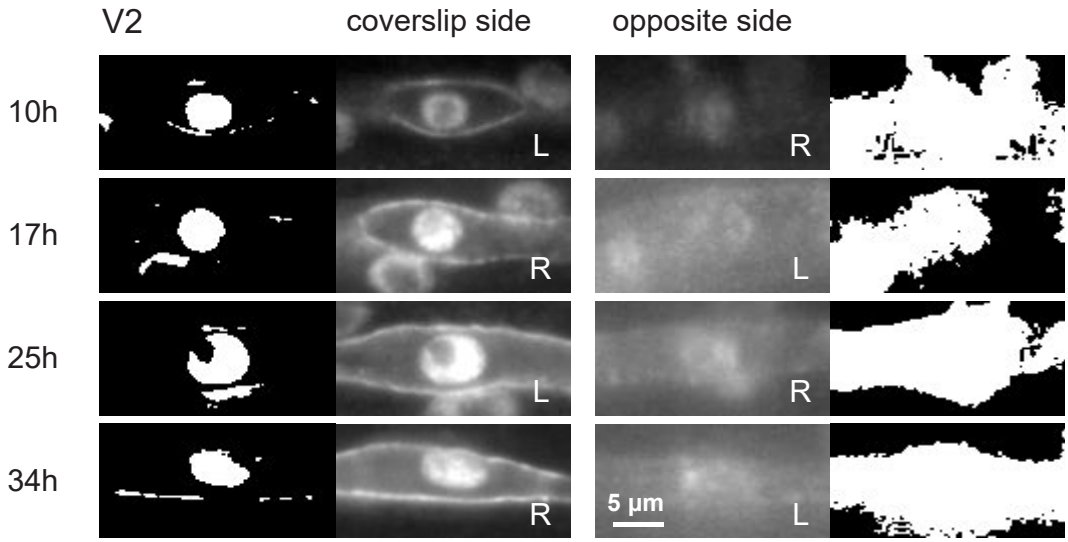

Figure 4.5: Image analysis of *wrt-2* strain. Raw images and masks obtained with the Otsu's algorithm of single seam cells in the V2 lineage extracted from the straightened images by manual labeling and automatic cropping. The images shown correspond to the time of maximum *wrt-2* expression. Time is in hours after hatching. Left columns: seam cell closest to the objective. Right Columns: corresponding seam cell on the other side of the sample. The label indicates whether the seam cell is on the right (R) or left (L) side of the animal.

We found that seam cells lying further away from the objective along the axial direction show a degraded fluorescence signal, likely due to light scattering in the animal's tissues (Fig. 4.5). Moreover, as animals sometimes flip from one side to the other, most often during the molt [142], the identity of the row of seam cells closer to the objective changes over the course of development. We tried to apply the segmentation algorithm to seam cells lying further away from the objective at

time points in which the fluorescence intensity is at its maximum levels. We found that the segmentation algorithm fails in detecting the nuclei of such cells (Fig. 4.5). Therefore, we decided to quantify fluorescence only for the seam cells on the side of the objective. To quantify the fluorescence intensity from the obtained masks, we first removed from the masks the small regions disconnected from the nucleus and computed the mean fluorescence intensity of the final mask.

4.3.1 Homogeneity of *wrt-2* expression

The expression of *wrt-2* in seam cells exhibited an oscillatory behavior (Fig. 4.6A). We found that both the period and phase of *wrt-2* oscillations agreed with previous measurements of *wrt-2* mRNA dynamics [136]. In particular, we observed four distinct peaks of expression for all the seam cell lineages analyzed (Fig. 4.6B). As for the *mlt-10* analysis, we first measured to what extent *wrt-2* expression oscillations are spatially synchronized by comparing time series from different seam cell lineages. Because we want to test whether oscillations are synchronized along the A-P axis, we combined data on seam cells on the left and right sides of the animal. Moreover, most of the seam cells undergo a symmetric division, therefore increasing the number of seam cells in the lineage. To analyze the time series, we decided to average, in each time-point, the fluorescence signal generated by all the seam cells in each lineage.

First, we correlated the time series for different seam cell lineages of 23 animals (Fig. 4.6C). The correlation coefficient for seam cells close to each other (for instance V1 and V2) was only slightly higher than the correlation coefficient for seam cells far away from each other (V1-V5 in Fig. 4.6C). To exclude that this is a V1 dependent behavior, we performed a cross-correlation analysis for all possible pairs of seam cell lineages (Fig. 4.6D). In contrast with the results for *mlt-10* expression, we did not find a clear pattern (Fig. 4.6E), suggesting that *wrt-2* expression in seam cells is synchronized across the whole body of the animal.

		L1	L2	L3	L4
Absolute timing [hours]	average	10.4	18.3	25.9	35.2
	standard deviation	0.6	0.7	1.1	1.6
Timing relative to ecdysis [hours]	average	-1.2	-1.2	-1.5	-3.0
	standard deviation	0.2	0.3	0.3	0.3

Table 4.2: Statistics of *wrt-2* expression peaks. Average and standard deviation of timing of *wrt-2* expression peaks (N=23).

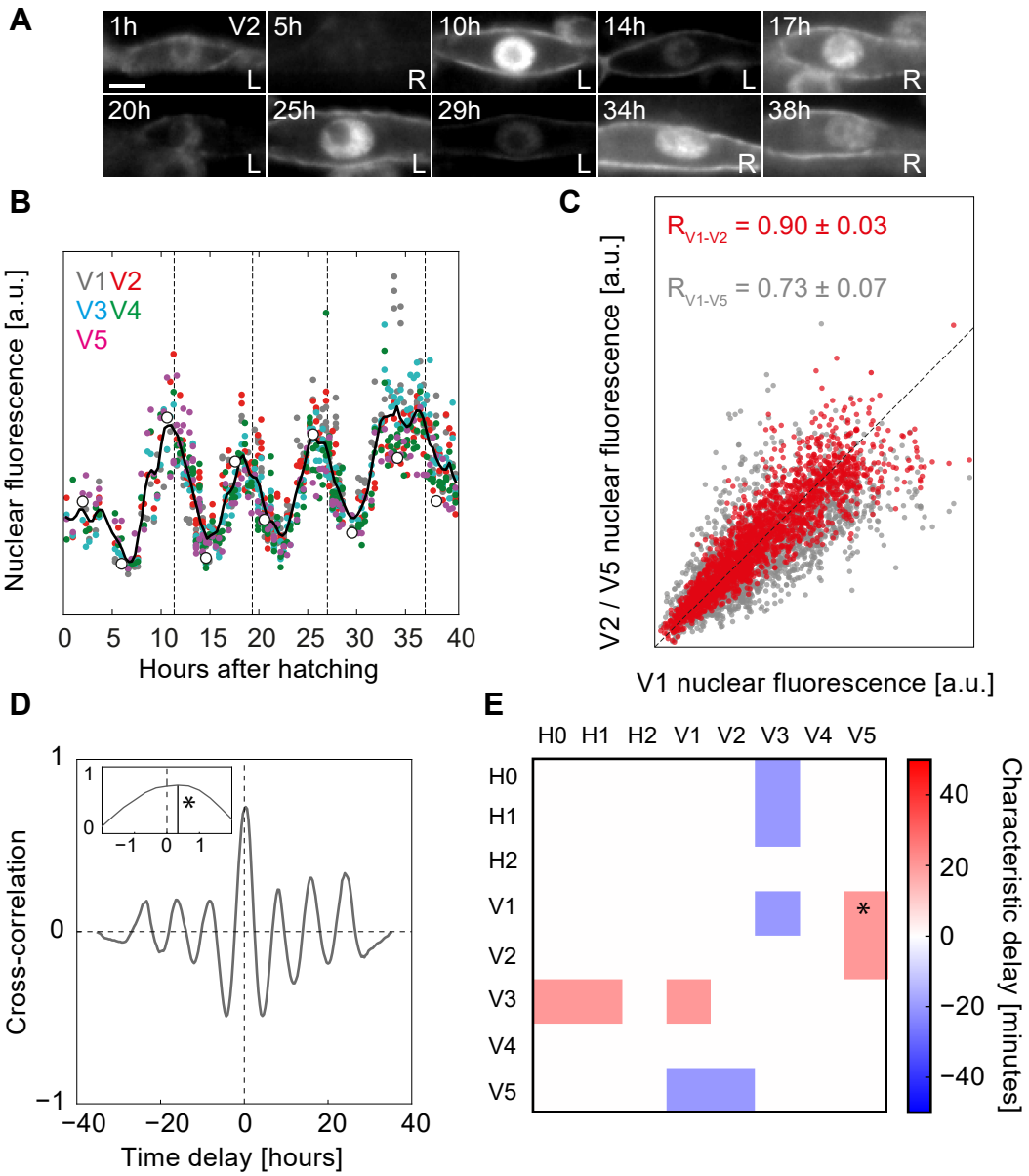

Figure 4.6: Synchronization of *wrt-2* expression. (**A**) *wrt-2* expression oscillations in the posterior-most V2 seam cell in a *heIs63[wrt-2p::H2B::GFP, wrt-2p::PH::GFP]* animal. Time is in hours after hatching. The label indicates whether the cell is the left (L) or right (R) V2 cell. Scale bar, 5 µm. (**B**) Single animal *wrt-2* expression oscillations. White markers correspond to the images in Panel A. The black line represents a sliding average with 1 hour window size over V1-V5. (**C**) Correlation in *wrt-2* expression between the V1 and V2 (red) and V5 (grey) cells. Markers and correlation coefficient *R* are for N=23 animals over all larval stages. (**D**) Cross-correlation function for the V1 and V5 time series of the animal shown in Panels (A) and (B). Inset shows the characteristic delay found for this particular pair of seam cell lineages (20 minutes). (**E**) Timing of the highest peaks in the cross-correlation function for each pair of seam cell lineages of the animal shown in Panels (A) and (B). Asterisk indicates the lag time for the (V1, V5) pair shown in Panel D.

4.3.2 Timing of *wrt-2* expression peaks

Similar to the analysis perform for *mlt-10*, we analyzed the *wrt-2* expression dynamics for multiple animals to quantify the animal-to-animal variability. To compare time series of different animals, we averaged the fluorescence intensity of all the seam cells in the same time-point. We found significant animal-to-animal variability, especially at later stages of development (Fig. 4.7A).

Therefore, we asked whether, as for *mlt-10*, variability in the timing of each peak can be explained by an overall molting cycle effect, that is, if times at which *wrt-2* expression peaks correlate with the closest ecdysis event. To detect the time of peaks of the *wrt-2* gene expression, we applied a Gaussian filter with width of 1 h as described in the previous section, and found the local maxima in proximity of each ecdysis event (Fig. 4.7A).

Similar to *mlt-10* expression oscillations, we observed that, while there existed significant animal-to-animal variability in the exact time of the *wrt-2* expression peaks (Fig. 4.7B and Table 4.2), the expression peaks were nevertheless precisely timed with respect to the ecdysis (Fig. 4.7C and Table 4.2).

4.4 Conclusions

In this chapter, we have shown that our technique allows for quantification of fluorescence intensity, even in single cells. Our technique improves previous approaches, that relied on quantification of gene expression in populations of animals, in two ways. First, we can follow the expression dynamics in animals over the full post-embryonic development with high temporal resolution. Second, instead of obtaining population average values, we can quantify the expression dynamics in single animals, making it possible for the first time to quantify the animal-to-animal variability. We applied our technique to the study of two genes that show oscillations in their expression, peaking once every larval stage. Such oscillations are speculated to provide a developmental timer to single cells in the animal. We developed a pipeline for the analysis of the data collected, which relies on multiple steps of analysis, from computational post-processing of the images to quantification of fluorescence signal.

First, we analyzed a gene, *mlt-10*, involved in the molting cycle and expressed in the whole body of the animal. We found that oscillations in the posterior part of the animal's body are slightly delayed compared to the anterior part. Moreover, when analyzing gene expression in multiple animals, we found high animal-to-animal variability in the timing of oscillation peaks. Nevertheless, we found that timing of the peaks are highly correlated with the timing of the closest ecdysis event.

Next, we focused on a second oscillatory gene, *wrt-2*, involved in normal growth and proper locomotion. While *mlt-10* is expressed in the whole body of the animal, *wrt-2* is only expressed in the seam cells. Therefore, by analyzing *wrt-2* gene expression pattern, we showed that our technique is capable of quantification of

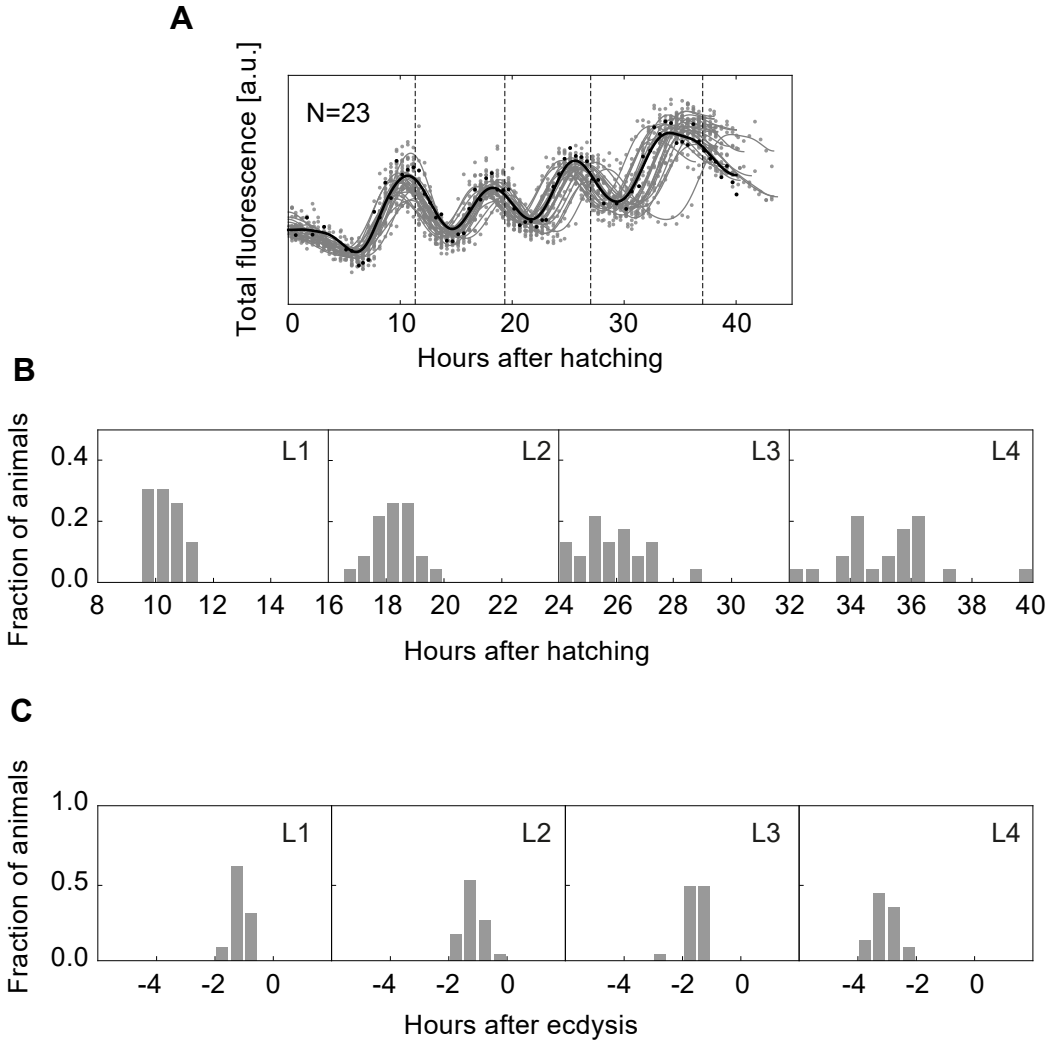

Figure 4.7: *wrt-2* expression in multiple animals. (**A**) *wrt-2* expression averaged over all the seam cells as a function of time for N=23 animals. The *wrt-2* expression dynamics (black line) and time of ecdysis (dashed lines) are indicated for the animal shown in fig. 4.6. (**B,C**) Time distribution of the peaks in *wrt-2* (N=23) expression relative to (B) time of hatching and (C) time of the most recent ecdysis event.

fluorescence intensity in single cells. We followed the same analysis performed for *mlt-10*. We found that *wrt-2* oscillations are highly synchronized along the A-P axis of the body. When analyzing multiple animals, we found that the timing of each peak is affected by high animal-to-animal variability. Nevertheless, similar to *mlt-10*, *wrt-2* expression peaks are synchronized with the closest ecdysis events. These results suggest that the times of the expression peaks of *mlt-10* and *wrt-2*, as well as the times of the ecdysis events, are affected by a variability generated by a common noise source.

Our results raise a number of fundamental questions on the nature of the gene expression oscillations. (i) What are the sources of the global variability we observed in the period of the oscillations? (ii) Is the correlation between oscillatory gene expression dynamics and ecdysis observed more generally, i.e. also for oscillatory genes that do not peak close to the molt? (iii) Are oscillations regulated at the single cell level by cell-autonomous timers, or is there a global temporal cue traveling in the whole body? The combination of standard *C. elegans* biology techniques and our time-lapse microscopy technique will be a powerful approach to answer these questions. For instance, (i) different hypothesis about the sources of noise can be tested by studying the gene expression dynamics of animals grown in our microfabricated chambers. For instance, the effect of temperature changes and food availability on the timing of the expression peaks can be studied by precisely controlling temperature over the duration of the experiment and the amount of food initially available. Moreover, (ii) cross-correlation analysis using animals carrying transcriptional reporters for multiple oscillatory genes could shed some light on the order in the timing of the peaks. Finally, (iii) our results show that *mlt-10* oscillations are slightly delayed in the posterior part of the body. Therefore, it is tempting to hypothesize a model in which a global temporal cue travels from the head to the tail of the animal. However, as the measured delay is in the order of 10-20 minutes, i.e. the temporal resolution of our experiments, to test this model, experiments at higher temporal resolution are needed. Moreover, this model would predict that expression in *lon* mutants, which have a significantly longer body, would show higher delays due to the longer spatial range that the traveling wave needs to cover. In general, the ability we demonstrated in this chapter to follow gene expression oscillations in single cells will be instrumental in addressing these questions.

5

Quantitative study of the dynamics of the AC/VU stochastic cell fate decision

This chapter is part of the following publication:
"S. Kienle*, N. Gritti*, Y. Goos and J. S. van Zon,
Quantitative analysis of a stochastic cell fate decision
during *C. elegans* development.
(in preparation)."

In the previous chapters, we applied our new microscopy technique to the study of deterministic developmental processes. However, developmental processes exist that are thought to be driven by molecular noise. A classical example of such processes are stochastic cell fate decisions, in which a group of cells are born identical and during the decision process randomly assume one fate out of a repertoire of possible fates. It is hypothesized that these cell fate decisions are driven by the amplification of stochastic molecular fluctuations by feedback loops in the underlying gene regulatory network.

Stochastic cell fate decisions have been studied by means of a molecular biology approach, which have been successful in revealing the key components and the underlying gene regulatory network. However, stochastic cell fate decision processes are strongly history-dependent. Therefore, in order to understand their driving mechanism and dynamics, a quantitative approach capable of following the process in time is needed. However, so far it has not been possible to image any stochastic cell fate decision process over its full duration.

The ability to quantify the dynamics of stochastic cell fate decisions could help answer the following fundamental questions:

- *What are the sources of noise driving stochastic cell fate decisions?* For instance, the key noise sources could be formed by stochastic variability in gene expression, cell signaling or in other biological processes. Moreover, how strong is the noise? Is it stronger compared to invariant developmental processes, in which noise needs to be strongly suppressed?

- *How are these fluctuations amplified?* In particular, do gene regulatory networks underlying stochastic cell fate decisions share common motifs optimized to amplify noise? Moreover, how robust are the underlying amplification mechanisms?

- *How is the timing of stochatsic cell fate decisions controlled?* In many cases, the cells specified in a stochastic cell fate decision are necessary for further development. Therefore, cell specification typically needs to occur within a limited time window, often on the order of few hours. How can an intrinsically stochastic process provide robust cell fate specification within the limited time allowed by development?

In order to address these questions, we applied our time-lapse microscopy technique to the study of a simple stochastic cell fate decision: the AC/VU decision. As we will describe in the next section, the genetics of this system is well understood, making it uniquely suited for our approach.

In this chapter, I will first describe in detail the current understanding of the AC/VU decision (Section 5.1). I will pay particular attention to the questions that remain unanswered and what is needed in order to fully elucidate the mechanisms underlying the AC/VU decision process. Next, I will describe the results obtained in our group and the implications that these results have on our current understanding of the AC/VU decision. In particular, we used two techniques that complement each other. First, we used single molecule fluorescence *in situ* hybridization (smFISH), a technique that allows to measure mRNA levels with single-molecule resolution, to quantitatively study the key components of the gene regulatory network involved (Section 5.2). Even though smFISH represents a great quantitative tool to study the gene expression pattern, it requires the animals to be fixed, making it impossible to quantify the dynamics of expression over the full duration of the process. Therefore, we complemented this technique by applying our time-lapse microscopy technique to the study of the dynamics of the core component involved (Section 5.3). Our results indicate that at least two independent sources of noise are responsible for the correct fate determination during the stochastic AC/VU decision. Finally, I will discuss our results and propose additional experiments that could help elucidating the mechanisms underlying the AC/VU decision (Section 5.4).

5.1 The AC/VU stochastic cell fate decision

During the development of *C. elegans* hermaphrodites, the gonad is formed on the central part of the body to give rise to the reproductive machinery of the animal, which consists of the uterus, the egg-laying apparatus and the germ line cells. Particularly important for the development of the reproductive system is the anchor cell (AC), an organizer cell with crucial roles for the formation of both the uterus and the egg-laying apparatus.

The development of the gonad in hermaphrodites is initiated by two cells, Z1 and Z4, that divide three times during the first larval stage (Fig. 5.1A,B). Each division occurs along the anteroposterior axis of the animal, with cells named according to their position along the anteroposterior (A-P) axis relative to the parent cell (e.g. Z1.a and Z1.p, Fig. 5.1A,B). As a result of these divisions, the gonad primordium at the beginning of the second larval stage is composed of 12 cells [143]. Ten of these cells undergo invariant differentiation resulting in two so-called distal tip cells (DTCs) that are positioned at the opposite sides of the gonad and are responsible for the gonad elongation, four cells that will form the spermatheca, and four cells that will become part of the uterus. The remaining two cells, called Z1.ppp and Z4.aaa, lay in the center of the gonad on the ventral side and are born approximately at the same time. Despite being initially equivalent and undifferentiated cells, during the second larval stage Z1.ppp and Z4.aaa differentiate either into a ventral uterine cell (VU) or in the anchor cell (AC). The AC is particularly important for proper vulva development during the L3 larval stage. Interestingly, the fate determination process of Z1.ppp and Z4.aaa shows stochastic animal-to-animal variability: among a population of wild-type hermaphrodites, in 50% of animals Z1.ppp becomes the AC and Z4.aaa becomes the VU cell, while in the rest of the population the fates are reversed. Depending on the outcome of the differentiation process, the two cells, together with their sister cells Z1.ppa and Z4.aap, assume one of two possible morphological configurations of the so-called somatic primordium [143] (Fig. 5.1C). Independent of the particular configuration assumed at the end of the second larval stage, the three VU cells divide two times during the third larval stage and eventually form the ventral side of the uterus (Fig. 5.1C, bottom image). For the sake of clarity, in the rest of the chapter, we will follow the notation used in [144] and refer to Z1.ppp and Z4.aaa as α cells and to their sister cells, Z1.ppa and Z4.aap, as β cells (Fig. 5.1A,B).

5.1.1 An historical overview

Because of its relative simplicity, the AC/VU decision has become an important model system for stochastic cell fate decision processes. Therefore, it has been the subject of extensive studies that I will review in this section.

The first studies focused on elucidating the time frame in which the decision is made and the number of cells necessary for a proper decision process. These first

experiments made use of cell ablation, a technique to selectively remove a cell of interest by focusing a high intensity laser beam on it. Two main conclusions were obtained. First, when either of the α cells is ablated before the formation of the somatic primordium, the remaining α cell always assumes the AC fate, suggesting that at this early stage of development cells did not commit to a fate yet [145]. However, when the AC is ablated after the somatic primordium is formed, the second α cell is not capable of becoming an AC, suggesting that at this later stage of development cells have terminally differentiated [146]. These results also suggest that the presence of both α cells is required to specify the VU fate, but the presence of one of them is sufficient to obtain an AC. Second, when both the β cells are ablated, the two α cells always differentiate in one AC and one VU, while when both α cells are ablated, β cells assume the AC fate only in small fraction of animals [147]. These results suggest that both α cells are necessary and sufficient for the proper AC/VU decision process, and that the AC and the VU fates are specified in a mutually exclusive manner, i.e. the decision process always results in one AC and one VU cell. This decision process is driven by cell-cell interactions between the two α cells.

To study the molecular nature of the cell-cell interaction, other studies focused on the analysis of the AC/VU decision process in mutant animals. In 1983, for the first time, it was recognized that the gene *lin-12* plays a major role during the AC/VU decision [148]. The LIN-12 protein is part of the Notch signaling pathway, a cell-cell interaction mechanism that is extremely conserved among many multicellular organisms: developmental processes relying on this pathway can be found in *C. elegans*, *Drosophila* and higher vertebrates up to humans [149]. In *C. elegans*, the LIN-12/Notch protein is a trans-membrane receptor protein that mediates the cell-cell interaction and is activated upon binding of a ligand molecule.

Specifically, *lin-12* has been extensively studied over the years focusing on mutant animals in which *lin-12* activity is either elevated (gain of function mutants, referred to as *lin-12(gf)*) or suppressed (loss of function, *lin-12(lf)*). Interestingly, it was found that in both *lin-12(gf)* and *lin-12(lf)* mutant animals the AC/VU fate determination was invariant. In particular, in *lin-12(gf)* mutants both α cells assumed the VU fate, while in *lin-12(lf)* mutants both α cells assumed the AC fate [148, 150]. This result suggests that *lin-12* activity is necessary and sufficient to specify the VU fate. Other experiments exploited mosaic analysis, a technique to create animals in which the two α cells have different *lin-12* activity levels. In some cases, researchers found animals in which one of the Z lineages (e.g. Z1) was *lin-12(lf)*, while the other lineage (e.g. Z4) showed wild-type *lin-12* activity (*lin-12(+)*). In these animals, consistent with the *lin-12(lf)* phenotype, the *lin-12(lf)* α cell always differentiated into an AC. Moreover, the *lin-12(+)* α cell always becomes a VU cell [147]. This result is a strong evidence of the presence of an AC-to-VU signal mediated by *lin-12* activity and that this signal is necessary in order for a cell to assume the VU fate. If this was not the case, the *lin-12(+)* α cell would have shown stochastic variability, therefore assuming the AC or VU fate with equal probability.

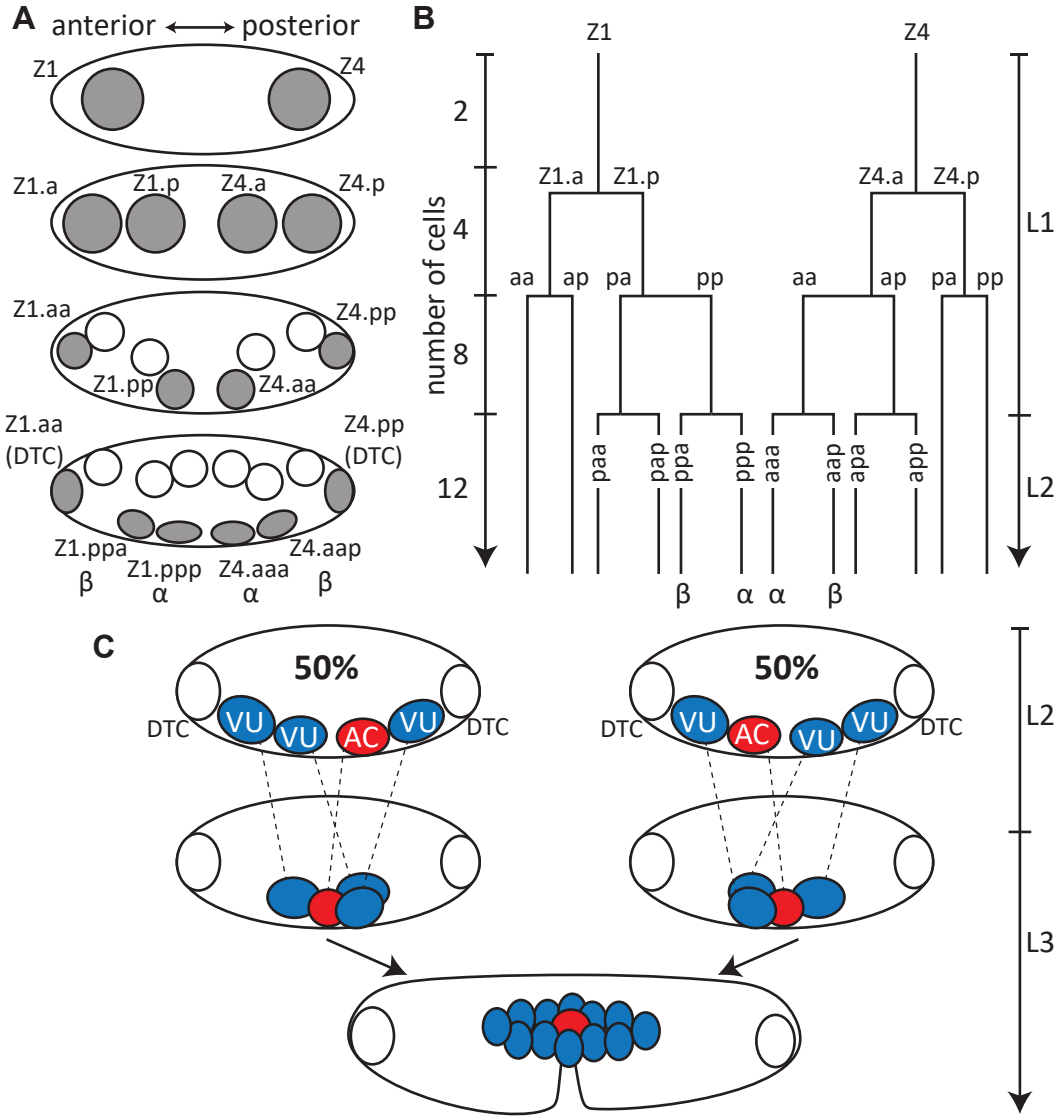

Figure 5.1: Gonad development and AC/VU decision. (**A**) Schematic of gonad development during the first two larval stages. Names are given for cells highlighted in gray. Anteroposterior direction is indicated on top of the image. α and β cells are indicated at the bottom. (**B**) Cell lineages and total number of cells in the gonad during the first two larval stages. (**C**) Gonad development during the L2 and L3 larval stages. Cells in blue represents ventral uterine cells, cells in red represent anchor cells. Depending on which cell becomes the AC, the somatic primordium assumes one of two possible configurations (left and right images, first two rows). Cell migrations are indicated by dashed lines. As the gonad develops in the L3 stage, the VU cells divide two times and rearrange in such a way that the two different initial configurations result in the same final invariant configuration (bottom image).

Even though the key role of *lin-12* was recognized, the full molecular description was still missing. In particular, the nature of the AC-to-VU signal and the regulatory network involved had not been elucidated yet and therefore became the subject of investigation. Greenwald et al. performed experiments using transcriptional and translational reporters together with antibody staining to assess the expression and protein accumulation pattern of *lin-12* and the expression pattern of *lag-2*, a gene predicted to encode a Notch ligand protein [151–153]. The animals analyzed were temporally ordered according to the relative position of the α and β cells: animals in which the somatic primordium was not formed yet were interpreted as animals at an early stage of the AC/VU decision (Fig. 5.1C, first row). On the other hand, animals in which a somatic primordium was formed were interpreted as animals in which the AC/VU decision was completed (Fig. 5.1C, second row).

First, animals were created in which the promoter of either *lag-2* or *lin-12* drove the expression of LacZ, and antibody staining against LacZ was used to detect whether the promoter of interest was expressed in the α cells. Expression patterns of *lag-2* and *lin-12* were found to change in a reciprocal manner. In particular, it was found that both *lag-2* and *lin-12* were initially expressed in both α cells. However, by the end of the AC/VU decision, *lin-12* expression became restricted to the VU cell, while *lag-2* expression became restricted to the AC [151, 152]. Moreover, LacZ antibody staining in a *lin-12(lf)* mutant showed that, while *lin-12* is initially expressed in both cells, it is not expressed in either cell during the decision process. Therefore, while *lin-12* activity is not necessary to start the *lin-12* expression right after the α cells are born, it is necessary to maintain *lin-12* expression during the AC/VU decision process. The mutually exclusive expression patterns of *lag-2* and *lin-12* suggest that *lin-12* activity in one cell downregulates *lag-2* expression in that same cell. Moreover, the results on *lin-12(lf)* mutants are a strong indication for the existence of a positive feedback loop involving *lin-12* where activated LIN-12 receptors induce expression of more *lin-12* in that same cell.

Next, using antibody staining against the green fluorescence protein (GFP) in a *lin-12* translational reporter strain, the protein accumulation pattern of LIN-12 was studied in paralyzed animals. Greenwald et al. found that, similar to the expression pattern of *lin-12*, the protein LIN-12 initially accumulates in both α cells, while by the end of the decision process it is found only in the VU cell. The similarity between the patterns of the promoter activity and the protein accumulation suggests that LIN-12 proteins are relatively unstable [153].

Even though the molecular players involved in the cell-cell interaction had been found, it was not yet known how *lin-12* activation in one cell could lead to the down-regulation of *lag-2* in that same cell. To this end, Greenwald et al. studied the protein accumulation pattern of a transcription factor called HLH-2. In particular, they studied how its spatiotemporal pattern compares to both *lag-2* and *lin-12* expression. Three categories of animals were found. First, animals in which *lag-2* and *lin-12* were expressed in both cells, but HLH-2 was not found in either. Second, animals in which *lag-2* and *lin-12* were expressed in both cells, while HLH-2 was present in

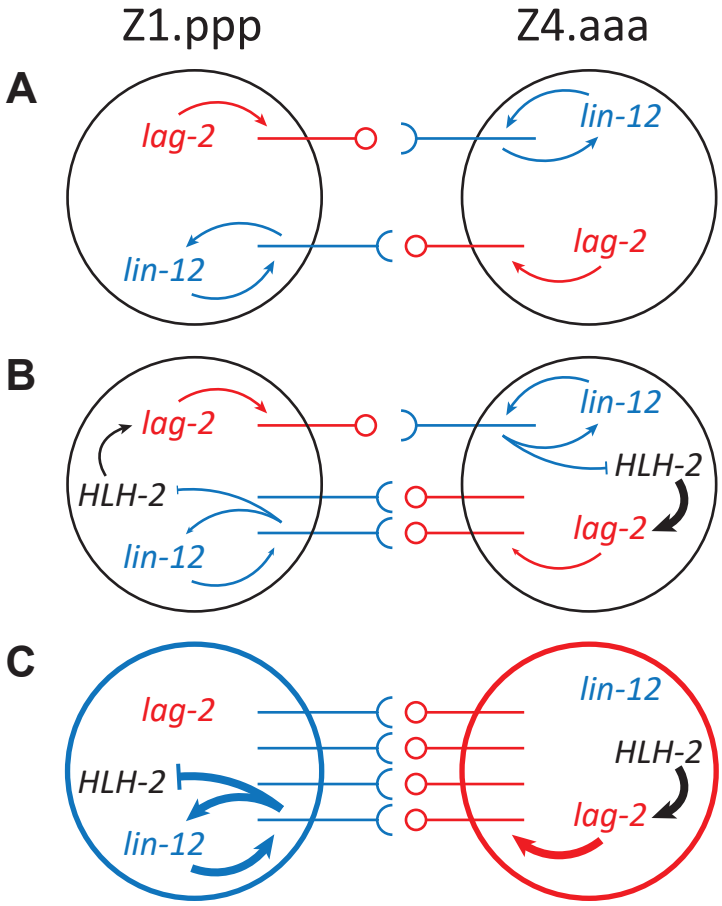

Figure 5.2: Current model of the AC/VU stochastic cell fate decisions. (**A**) α cells are born identical, i.e. both expressing *lag-2* and *lin-12* and neither producing HLH-2. (**B**) A different in HLH-2 accumulation between the two cells is the first detectable difference between the two α cells. LIN-12 is more highly activated in one of the two α cells (Z1.ppp in the figure). As a consequence, two positive feedback loops are activated. First, LIN-12 activation in Z1.ppp causes higher *lin-12* expression in the same cell. Second, LIN-12 activation in Z1.ppp downregulates HLH-2 production in the same cell, which results in lower *lag-2* expression. (**C**) The positive feedback loops result in an all-or-nothing decision in which one cell (Z1.ppp) expresses only *lin-12*, therefore assuming the VU fate, and the other cell (Z4.aaa) expresses only *lag-2*, therefore assuming the AC fate. In all the panels, thickness of the arrow lines indicates the degree of activation of that particular part of the network.

only one cell. Third, animals in which *lin-12* was expressed in one cell, while *lag-2* and HLH-2 were present in the other cell. Moreover, HLH-2::LacZ transcriptional reporter animals showed expression in both cells for the entire duration of the decision, suggesting that HLH-2 is post-transcriptionally regulated [154]. Based on the observation that *lag-2* has 11 potential HLH-2 binding sites, Greenwald et al. came to the conclusion that HLH-2 is a direct transcriptional activator for *lag-2*.

Therefore, the HLH-2 data were interpreted in a temporal manner: first, *lag-2* is equally expressed in both α cells right after division (Fig. 5.2A). Second, a variability in HLH-2 protein accumulation is the first detectable difference between the α cells (Fig. 5.2B). Third, this variability is amplified in a positive feedback loop such that the cell with more HLH-2 expresses more *lag-2*. This leads to stronger activation of *lin-12* in the neighboring cell, where it causes post-transcriptional down-regulation of HLH-2, which in turn decreases *lag-2* expression in the same cell [155]. The amplification of small stochastic fluctuations therefore results in one cell only expressing *lag-2* and the other cell only expressing *lin-12* (Fig. 5.2C).

Given that HLH-2 levels form the first detectable difference between the two α cells, it was concluded that one of the sources of noise driving the AC/VU decision was the HLH-2 accumulation. However, more sources of variability might be present that contribute to drive the AC/VU decision process. In fact, another source of noise was identified: the birth order of the α cells. Since the first common cellular ancestor of the α cells is as far as four generation earlier, the time at which they are born is different, with differences in the time of birth ranging from two minutes to two hours. By analyzing wild type animals with differential interference constrast (DIC) microscopy, it was found that this birth order highly influences the outcome of the AC/VU decision, in that the second-born cell has greater probability of becoming the AC (12 out of 13 animals) [154]. To explain this result, it was hypothesized that, in the first first-born cell, *lin-12* activation occurs earlier or at higher levels, therefore leading to suppression of HLH-2 in the same cell and a disadvantage in becoming the AC. Several hypotheses were offered to explain *lin-12* activation. For instance, LIN-12 accumulation in the first-born cell could provide higher probability of LIN-12 activation. Alternatively, LIN-12 present on the surface of the first-born cell could be activated by the LAG-2 present on the surface of other surrounding cells. Another hypothesis is that the first-born cell activates LIN-12 due to cell cycle progression, in particular as it has been shown in other systems in *C. elegans* that the passage from the S phase to the G_2 phase is necessary for LIN-12 activation [156].

5.1.2 Open questions

Thanks to the genetics experiments summarized in the previous section, the molecular mechanisms involved in the AC/VU decision have been partly elucidated and a model has been proposed that describes the possible dynamics during this stochastic cell fate decision. The current model of the AC/VU decision can be summarized as follows:

1. The α cells are born approximately at the same time, both expressing similar levels of *lag-2* and *lin-12* (Fig. 5.2A);
2. Small stochastic fluctuations in the activity of the key regulators, potentially driven by differences in the birth order of the α cells, lead to higher LIN-12 activation in one α cell, α_1, compared to the other α cell, α_2 (e.g. α_1 =Z1.ppp and α_2 =Z4.aaa in Fig. 5.2B). The difference in LIN-12 activation between the two α cells triggers two positive feedback loops;
3. First, activation of LIN-12 in α_1 maintains expression of *lin-12* in the same cell, potentially leading to more LIN-12 activation (Fig. 5.2B);
4. Second, LIN-12 activation in α_1 post-transcriptionally downregulates HLH-2 accumulation in the same cell, which in turn results in lower *lag-2* expression in α_1, resulting in lower LIN-12 activation in α_2 (Fig. 5.2B);
5. As a consequence, HLH-2 is accumulated and *lag-2* is expressed in α_2;
6. All together, these positive feedback loops cause α_1 to only express *lin-12*, therefore assuming the VU fate, and α_2 to only express *lag-2*, therefore assuming the AC fate (Fig. 5.2C).

Even though this model represents the best understanding of the AC/VU decision currently available, the following important questions remain unanswered.:

- *What are the sources of noise driving the AC/VU decision?* Birth order strongly correlates with the cell fate determination, yet an animal was found in which the first born cell assumed the AC fate even though the α cells were born forty minutes apart. Hence, another source of variability must be responsible for the cell fate determination in this class of animals. This leads naturally to the question of how cell fates are determined when the α cells are born approximately at the same time. Is a different source of noise driving the AC/VU decision in these cases? Moreover, the birth order analysis showed cases in which, even though the α cells were born only two minutes apart, the second born cell assumed the AC fate. This raises the question on what is the minimal detectable difference in the time of division that results in the second born cell assuming the AC fate.
- *How can an intrinsically stochastic mechanism ensure the specification of the two cells within the allocated time?* Both AC and VU cells are of paramount importance for the proper formation of the reproductive system of *C. elegans*. However, a limited amount of time is allocated by development for these two cells to be specified. How variable is the time needed to reach the decision? How can the amplification mechanism always ensure that a single AC and a single VU are produced within the limited amount of time? Does the time to resolve the decision depend on the initial conditions and on the strength of the fluctuations?

In order to address these questions, a quantitative description of the dynamics of the key molecular players is needed. So far, the dynamics of the process has only been reconstructed with antibody staining techniques [154]. However, this approach is limited in two crucial ways. First, antibody staining techniques are not well suited to perform a quantitative analysis of gene expression. Therefore, the relative levels of expression in single cells are not accessible. This precludes the possibility to quantitatively study the variability that an intrinsically stochastic process such as the AC/VU decision shows. Second, in order to visualize the expression levels, animals need to be fixed. Therefore, due to the strong stochastic nature of the AC/VU decision, it is difficult to infer a temporal sequence of events from fixed images.

Instead, to fully elucidate the dynamics of the process, the expression levels of the key molecular players need to be quantitatively analyzed over time in individual live animals. In this chapter, we used two different quantitative approaches. (i) We used single molecule fluorescence *in situ* hybridization (smFISH), a technique able to visualize single mRNA molecules, to quantitatively analyze the variability in the expression levels of the key molecular players. Even though smFISH represents a unique tool to quantify the variability in the gene expression levels in different animals, it requires the fixation of the animals. As a consequence, the dynamics of the AC/VU decision process is not accessible. Therefore, (ii) we applied our time-lapse microscopy technique to follow the gene expression levels of the key regulators in single live animals over the full duration of the AC/VU decision. With this approach, we aim to elucidate the dynamics of the process, and in particular we aim to identify the key events occurring during the AC/VU decision that determine the cell fate outcome.

5.2 Quantitative analysis of gene expression in fixed animals with smFISH

The experiments shown in this section are part of a joint project with Dr. Simone Kienle, a post-doctoral researcher in the group. All the smFISH experiments presented here have been performed by Dr. Simone Kienle and hence the specific approaches used to perform the experiments and analyze the data will not be discussed. However, the interpretation of the data obtained has been performed jointly. As the smFISH experiments are tightly interlinked with the time-lapse experiments presented in Section 5.3, in this section I will briefly summarized the key results from the smFISH experiments.

Single molecule fluorescence *in situ* hybridization (smFISH) is a technique to visualize single mRNA molecules. The technique relies on the design of multiple short DNA probes that are complementary to different regions of an mRNA of interest [157] (Fig. 5.3A, top). Additionally, each probe is equipped with a fluorophore that can be visualized with fluorescence microscopy techniques. Even though a single fluorophore is hardly visible, multiple probes bind to a single mRNA, which is then

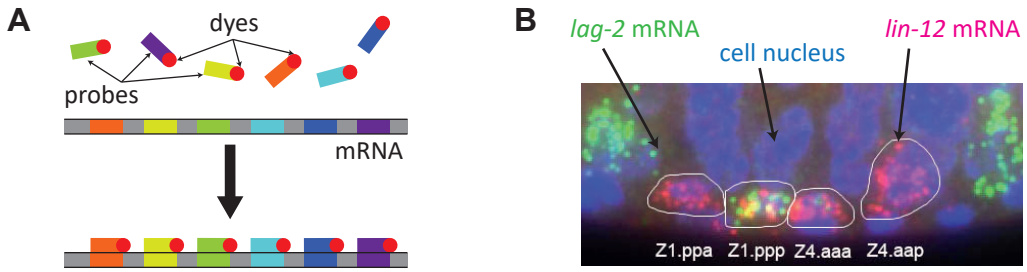

Figure 5.3: single molecule FISH working principle. (**A**) Working principle of smFISH. The probes (colored rectangles) are complementary to portions of the mRNA of interest. Red dots represent the fluorescent dyes. (**B**) Maximum projection of a fluorescent stack acquired for a single animal in which *lag-2* and *lin-12* mRNAs have been labeled with Cy5 (green dots) and Alexa (red dots) fluorescent dyes. Cell nuclei have been labeled with DAPI stain (blue regions).

labeled with as many fluorophores as the number of probes attached (Fig. 5.3A, bottom). Therefore, a single mRNA is visible as a diffraction limited spot when imaged with wide-field fluorescence microscopy. The key feature of this technique is the capability to quantitatively measure the expression pattern of genes of interests in single cells. Moreover, by labeling probes belonging to different gene transcripts with different fluorophores, it is possible to visualize mRNAs of different genes in the same cells.

5.2.1 Quantitative analysis of smFISH data

To study the expression pattern of the key regulators of the AC/VU decision, we performed smFISH experiments on multiple animals. In particular, we aimed to measure the dynamics of the expression patterns of the two main regulators, the receptor *lin-12* and the ligand *lag-2* (Fig. 5.3B). To this end, we performed two-colors smFISH by labeling *lag-2* mRNAs with Cy-5 smFISH probes and *lin-12* mRNAs with Alexa-594 smFISH probes in wild-type animals. Next, we measured the body length of each animal analyzed. Thanks to the fixed, larval stage-dependent growth rate shown in Section 2.3.2, we could then infer a temporal sequence by comparing the body length of fixed animals.

First, we quantified the absolute number of mRNA molecules in single cells as a function of body length (Fig. 5.4A,C). We observed that both *lag-2* and *lin-12* show high animal-to-animal variability in the number of mRNAs. Surprisingly, we found (i) that *lag-2* mRNAs are present also in the mother cells (black dots), which to our knowledge is a novel observation, and (ii) that *lag-2* expression in the mother cells shows high cell-to-cell variability (black dots in Fig. 5.4C, average mRNA counts and standard deviation 18±17).

Moreover, we observed that, for animals longer than 0.38 mm, a sub-population of α cells showed much higher *lag-2* expression compared to other α cells (Fig.

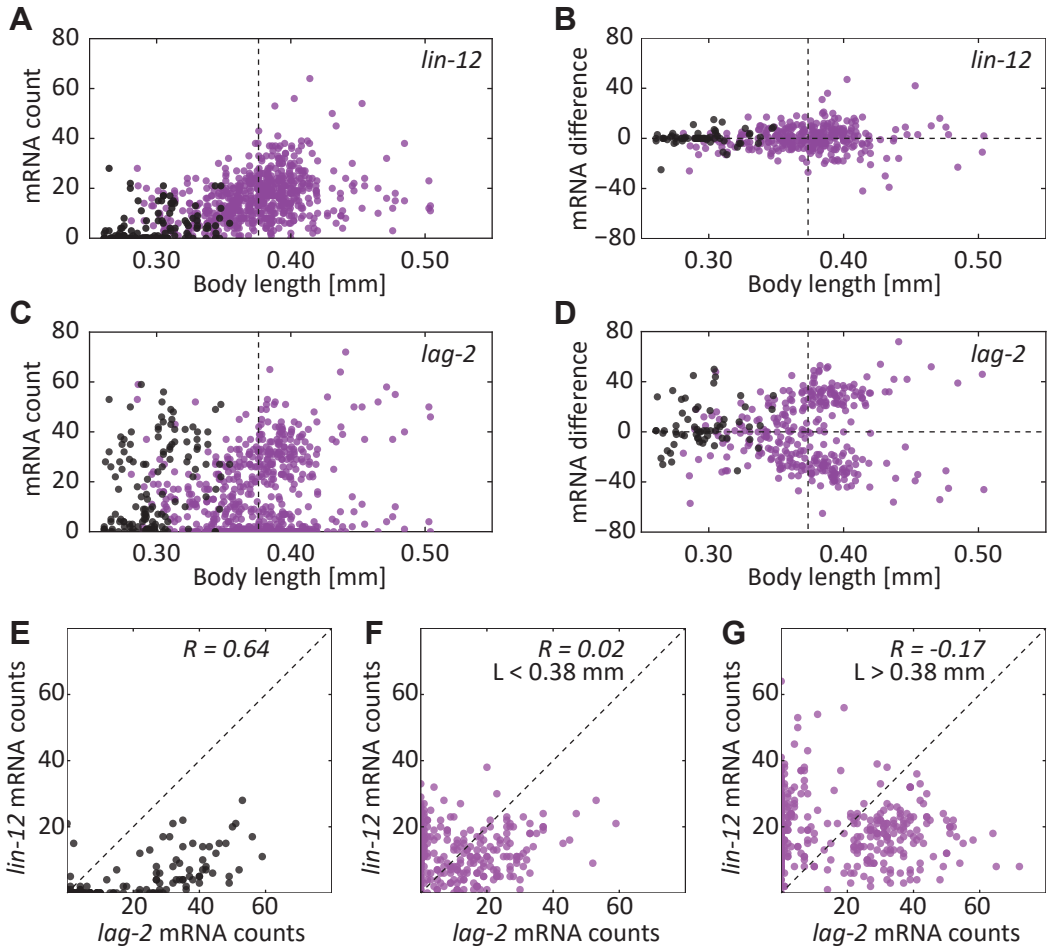

Figure 5.4: Results of the smFISH experiments on wild-type animals. (**A,C**) Number of mRNAs in Z1.pp and Z4.aa (black dots) and in the α cells (magenta dots) as a function of body length. For each cell, both *lin-12* (A) and *lag-2* (C) mRNAs are measured. The vertical dashed line represents the size threshold (0.38 mm) used to discriminate between shorter and longer animals in which both the α cells are already born. (**B,D**) Difference in mRNA levels between pairs of cells in the same animal. The difference is always computed as the mRNA level in the anterior cell minus the mRNA level in the posterior cell (e.g. Z1.ppp-Z4.aaa). The identity of the cells of interest depend on whether the α cells are born already. The identity of the cells is assessed by cell size, cell positions and gonad morphology. In case neither of the two α cells was born yet, we compared the levels between the two mother cells (black dots). Animals in which one of the two α cells is born are also represented with black dots. In this case we compared the other mother cell with the α cell that is already born. In case both mother cells divided, we compared the levels between the two α cells (magenta dots). (**E-G**) Correlation plots for the mRNA numbers of *lag-2* and *lin-12* for the mother cells (E), α cells in animals shorter than 0.38 mm (F) and α cells in animals longer than 0.38 mm (G). The correlation coefficient R is given for each plot.

5.4C, magenta dots on the right side of the vertical dashed line). That is, *lag-2* expression assumed a bimodal distribution by the end of the AC/VU decision, which is consistent with the current AC/VU decision model in which *lag-2* expression is eventually restricted to the AC. Surprisingly, we instead observed that *lin-12* is expressed in all the α cells analyzed, suggesting that both α cells in the same animal express *lin-12*, even at the end of the decision process (Fig. 5.4A, magenta dots). To further investigate the expression levels in the α cells within the same animal, we computed the difference in the mRNA levels of *lag-2* and *lin-12* between the anterior and the posterior cells. In general, we found that *lag-2* is always more highly expressed in one of the two α cells at later stages of the AC/VU decision (bodylength > 0.38 mm, Fig. 5.4D). However, α cells within the same animal showed similar levels of *lin-12* expression at all stages of the AC/VU decision (Fig. 5.4B). This result is at odds with previous observations, which reported that *lin-12* expression is eventually restricted to the α cell that will assume the VU fate.

To further investigate this discrepancy we examined the correlation between the number of receptor mRNAs and ligand mRNAs in the same cell. If, as the current model of the AC/VU decision suggests, *lin-12* activation leads to lower expression of *lag-2*, we expect a negative correlation in the expression levels of *lag-2* and *lin-12* in the same cell. That is, if one α cell shows high expression of *lag-2*, the *lin-12* expression in the same cell should be low. To test this hypothesis we correlated the number of *lag-2* mRNAs and *lin-12* mRNAs in the same cell at three different temporal stages: in the mother cells (Fig. 5.4E), in the α cells for animals at early stages in the AC/VU decision (Fig. 5.4F) and in the α cells for animals at later stages (Fig. 5.4G). To discriminate between earlier and later stages, we chose a body length threshold (0.38 mm), as in animals longer than this threshold *lag-2* is predominantly expressed in only one α cell (Fig. 5.4C,D). We did not find correlation between the levels of *lag-2* and *lin-12* in any of these temporal stages, as summarized by the small correlation coefficient (Fig. 5.4E-G).

5.2.2 smFISH experiments: conclusions and outlook

The current model of the AC/VU decision predicts that, by the end of the process, both *lag-2* and *lin-12* are expressed in only one α cell in a mutually exclusive manner. However, in this section, we have shown that *lin-12* is expressed in both α cells during the full duration of process. On the other hand, *lag-2* expression is indeed eventually restricted to only one α cell. While we do not exclude the possibility that differential expression of *lin-12* might occur at even later stages in development or that *lin-12* might be post-transcriptionally regulated, our results suggest that the expression of *lag-2* is more dynamic than the expression of *lin-12*. This result poses the question on whether *lag-2* is alone responsible for the cell-cell interaction and therefore for the decision process. In this case, LIN-12 would be a passive communication channel to relay the feedback signal formed by the *lag-2* expression levels from one cell to the other.

In this section, we have also shown that mother cells express both the genes encoding for the ligand and the receptor proteins. In particular, we found high variability in the expression of the ligand *lag-2*. As a consequence, upon division, a number of *lag-2* mRNAs are likely inherited by the α cell. This observation raises questions about the nature of the source of noise in the AC/VU decision: is it possible that the α cells are not born identical, but rather they initially have different potentials to assume the AC fate? In particular, could the α cell that inherits more *lag-2* mRNAs have an advantage in assuming the AC fate?

To address these questions, we studied the AC/VU decision in live animals over time by means of fluorescence time-lapse microscopy. With time-lapse microscopy, we can directly measure the correlation between the expression levels in the mother cells and the final cell fates. Moreover, time-lapse microscopy analysis of gene expression might help elucidate other aspects of the AC/VU decision that have so far been inaccessible. Specifically, we can study the effect of the difference in the division time on the dynamics of the process, in particular in animals in which the α cells are born approximately at the same time. Moreover, as the second-born cell has greater probability of assuming the AC fate, we can study the gene expression dynamics in those exceptional animals in which the second-born cell assumes the VU fate, hence testing whether additional sources of noise are responsible for the correct AC/VU specification in these animals.

5.3 Gene expression dynamics by fluorescence time-lapse microscopy

To quantify the expression dynamics of *lag-2*, we chose the already existing transcriptional reporter strain *arIs131 [lag-2p::2xNLS::YFP, ceh-22::GFP]*, in which the production of the yellow fluorescence protein (YFP) is controlled by the expression of the *lag-2* promoter and the YFP proteins are driven to the cell nucleus. In order to detect the position of the nuclei of cells that did not expressed *lag-2*, we crossed this strain into the strain *stIs10226 [his-72p::HIS-24::mCherry::let-858 3' UTR + unc-119(+)]*, which shows constant mCherry expression in all cell nuclei.

5.3.1 Experimental design and data analysis

In order to maximize the fluorescence signal collected from single cells, we used an high magnification and high N.A objective (60X, N.A.=1.4). To ensure that animals are always in the field of view of the camera when imaged with a 60X objective, we confined them in small chambers (190x190x10 μm^3). As we showed in Section 2.3.2, animals in these chambers grow normally only until the L3 larval stage. However, this did not represent a problem, as the AC/VU cell fate decision occurs during the L2 stage.

Because of the presence of two fluorescence signals (YFP and mCherry), the time-lapse imaging was performed using three different light sources: a red LED (transmission image), a 488 nm laser (YFP excitation) and a 561 nm laser (mCherry excitation). We used the YFP strain because no *lag-2* transcriptional reporter strains for GFP exist. With our laser we were able to excite YFP (optimal excitation at 515 nm) at 40% of its maximum. Therefore, in order to maximize the collection of the emission signal, we used the highest laser power provided by our setup (100 mW). Because of the high intensity of the laser, we needed to optimize the exposure time, the time interval between consecutive time points and the number of slices acquired in a single stack to obtain high signal-to-noise ratio and, at the same time, avoid phototoxicity. We found that, using 5 ms exposure time, 10 minutes time interval and 25 slices with 1 µm spacing, we did not affect the larval development of the animals. At the same time, these settings were sufficient to always have the cells of interest in the range of the stack, with sufficiently high signal-to-noise ratio, and enough time resolution to study the dynamics of the *lag-2* gene expression.

The total size of the images collected for a single worm added up to ~100 Gb. Therefore, we developed Python graphical user interfaces to analyze single images in the following manner:

- First, we used the transmission images to perform an average projection of each stack and collect all the resulting images in a single time-lapse video. From this collection of images, the hatching time and all ecdysis event times were visually detected and annotated.

- Next, we loaded each movie in a graphical user interface and manually annotated the position of the gonad in the image (Fig. 5.5A). We then used this position to crop a portion of the image centered on the gonad and save it in a separate `.tif` file. As these images consisted of 512x512 pixels, they occupied less space on the computer drive, making it faster to load each stack for further image analysis.

- Next, we loaded the new stacks in a user interface and manually annotated the position and the identity of each cell based on the positions of the nuclei in the whole body and relative to their positions in the previous time point (Fig. 5.5B).

- A sub-region of the image centered on the cells of interest was selected and the outline of the cell was created. As the size of the cell nuclei can change over time and between different cells, the dimension of the sub-region can be chosen by selecting the number of pixels to visualize. Here, we typically used 5µm x 5µm. The cell outline can be computed in an automated way from the YFP image with the Otsu's algorithm or manually selected in case of failure of the automated detection (Fig. 5.5C). This is typically the case when cells lose their YFP fluorescence signal or when the mCherry fluorescence marker

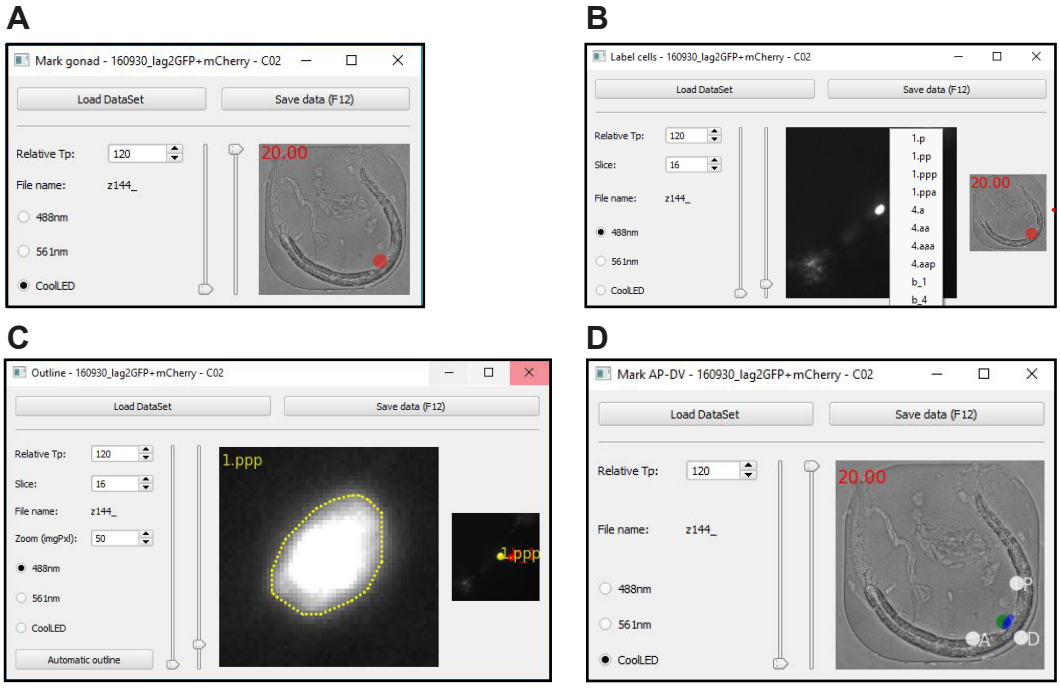

Figure 5.5: Image analysis work-flow. (**A**) User interface used to manually select the gonad region (black dot). (**B**) Manual labeling of single cells. Both fluorescence and transmission channels can be showed to help cell identification. Overview of the animal's position is shown on the right. (**C**) Cell outline detection. Automatic detection using the currently displayed fluorescence channel can be computed with the button in the bottom left corner. (**D**) Animal's orientation is annotated by the anterior (A), posterior (P) and dorsal (D) sides of the body (white dots).

is particularly dim. The YFP fluorescence intensity was quantified in single cell nuclei by averaging all the pixel values inside the cell outline.

- To visualize the dynamics of single cells, we detected the orientations of the animal's body in the image by annotating the anterior, posterior and dorsal sides of the animal around the gonad. We then oriented each gonad region such that the anterior side of the gonad is on the left, the posterior side on the right and the dorsal side on the top of the image (Fig. 5.5D). Finally, we cropped a 4µm x 4µm sub-region centered on the cell nuclei. All the frames for a single cell were collected in a `.tif` movie and saved on the computer drive.

In this way, we could reduce the ~100 Gb of raw imaging data in ~100 Kb containing only the cells involved in the AC/VU decision process (Fig. 5.6).

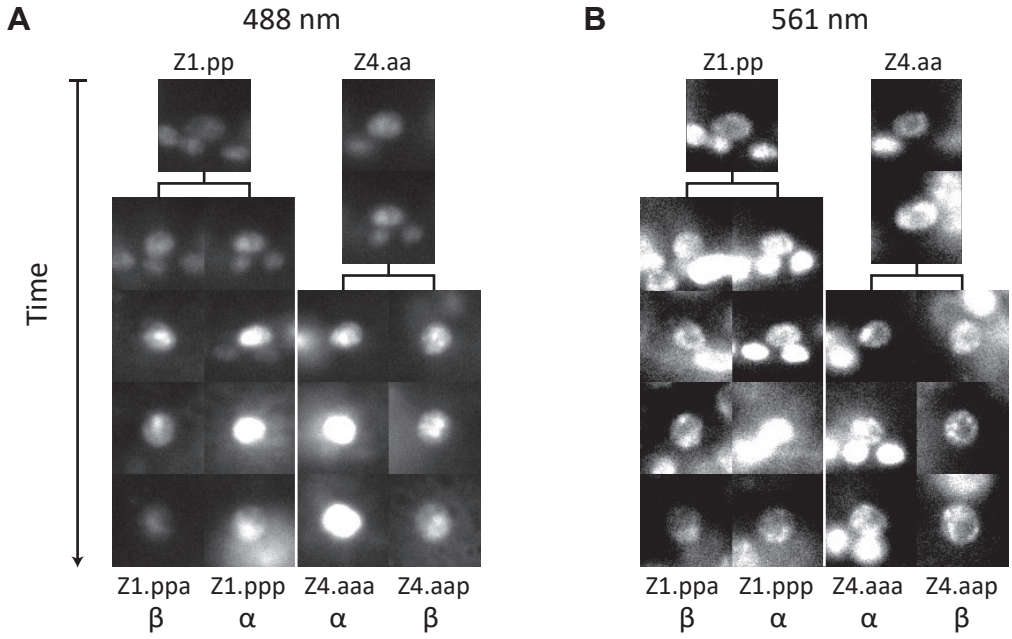

Figure 5.6: Fluorescence signal from single cell nuclei. Frames for the mother, α and β cells are shown for (A) YFP and (**B**) mCherry channel. Cell divisions are indicated by the solid lines between image rows.

5.3.2 Quantification of gene expression dynamics in single animals

Using our time-lapse microscopy technique and image processing pipeline, we were able to image the gene expression dynamics of *lag-2* in the α and β cells, as well as in the mother cells (Fig. 5.7A). We monitored the progression in the decision process in two ways. First, we measured the average fluorescence intensity in the nuclei as a function of time after the L2 ecdysis (Fig. 5.7B). Second, we measured the normalized fluorescence intensity difference $N(t)$ as a function of time (Fig. 5.7C):

$$N(t) = \frac{F_A(t) - F_P(t)}{F_A(t) + F_P(t)} \tag{5.1}$$

Here, F_A and F_P represent the fluorescence intensity in the anterior and posterior cell, respectively. Positive values of $N(t)$ represent time-points in which the anterior cell is brighter, while negative values of $N(t)$ represent time points in which the posterior cell is brighter. The quantity $N(t)$ is defined in the interval $(-1, 1)$, and it assumes values close to the boundaries (e.g. $N(t) \approx +1$ or $N(t) \approx -1$) when the fluorescence intensity is detected only in one of the two cells, i.e. when the AC/VU decision is completed. Because we are also interested in the expression dynamics of the mother cells, the identity of each cell changes when the cell division occur. For instance, the anterior cell is Z1.pp before division and Z1.ppp after division.

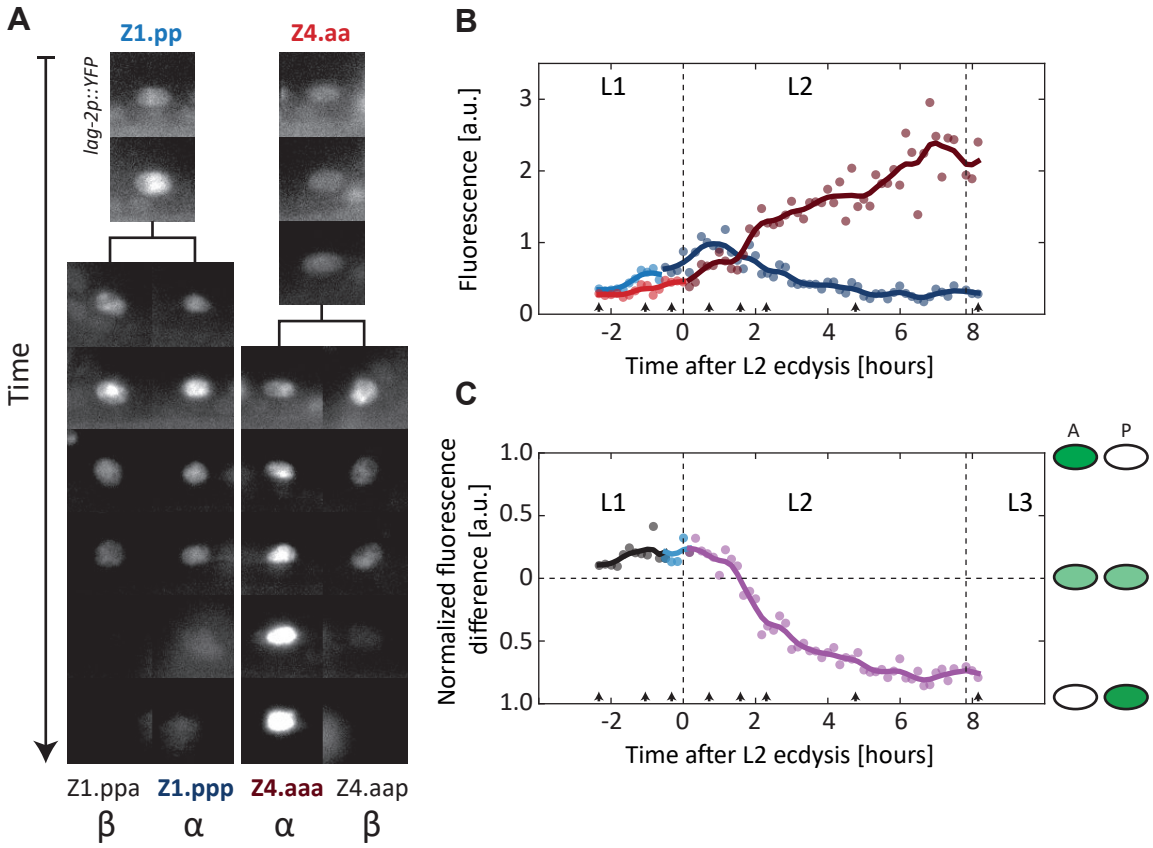

Figure 5.7: Quantification of time-lapse microscopy data. (**A**) Fluorescence images of single cells in the same worm over time. Cells in the same row belong to the same time point. Identity of cells is indicated at the first and last time points. Cell divisions are represented by solid black lines connecting the last image of the mother cell with the first images of the daughter cells. (**B**) Quantification of fluorescence intensity in Z1.pp (cyan dots), Z4.aa (orange dots), Z1.ppp (blue dots) and Z4.aaa (red dots). Time is in hours after the L2 ecdysis. Arrows indicates time-points shown in Panel (A). Solid lines represent Gaussain filter of the raw data with a width of 15 minutes. (**C**) Normalized fluorescence difference $N(t)$. Arrows indicates time points shown in Panel (A). The value for each time point is computed as the fluorescence intensity difference between the anterior and the posterior cell, divided by the sum of the two. Time is in hours after L2 ecdysis. Schematic of the fluorescence intensity in the anterior (A) and posterior (P) cells is shown on the right side of the panel for $N = +1$ (top), $N = 0$ (center) and $N = -1$ (bottom). The dynamics is divided in three qualitatively different phases. First phase: neither cells divided, therefore cells of interest are Z1.pp and Z4.aa (black dots and line). Second phase: one mother cell divided (Z1.pp in the example), fluorescence difference is computed between the new-born α cell and the other mother cell (Z1.ppp and Z4.aa in the example, cyan dots and line). Third phase: the other mother cell divided, fluorescence difference is computed between Z1.ppp and Z4.aaa (magenta dots and line). Vertical dashed lines represent the L2 and L3 ecdysis events.

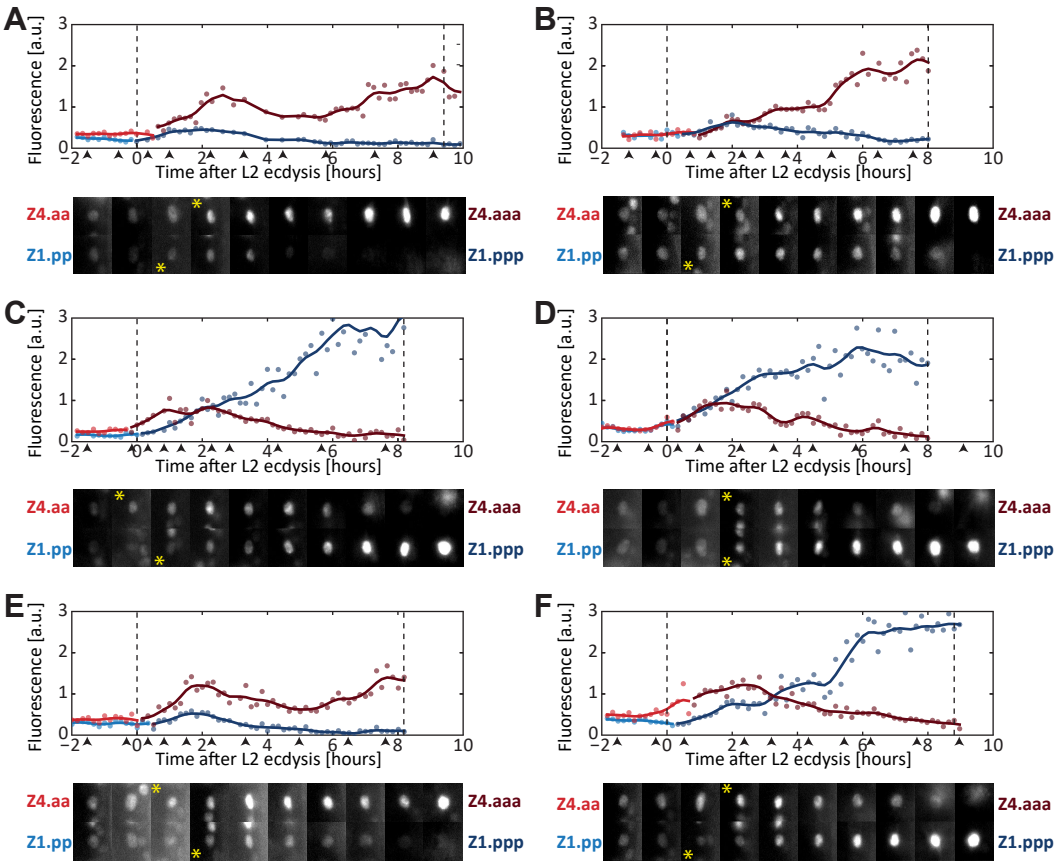

Figure 5.8: Examples of different AC/VU decision dynamics. Time traces and fluorescent images of mother cells and α cell for six animals showing different AC/VU decision dynamics. Arrowheads indicate time points shown in the images underneath. Vertical dashed lines represent times of L2 and L3 ecdysis. In the images, a yellow asterisk indicates the first time point in which the α cell is born. (**A-C**) Animals in which the second-born cell assumes the AC fate. (**D**) Animals in which cells are born at the same time. (**E-F**) Animals in which the first-born cell assumes the AC fate.

From the analysis of the smFISH data presented in the previous section, we found that *lag-2* mRNAs are already present in the mother cells. Similarly, in the time-lapse microscopy data, we observed fluorescence intensity already in the mother cells, suggesting that the *lag-2* reporter is expressed already before division. Moreover, both α and β cells show a fluorescence intensity significantly above the background level right after division. However, by the end of the L2 stage, fluorescence is always restricted to one of the α cells. At the L3 ecdysis, we always found the brighter cell in the central position of the gonad and the other cells surrounding it, which is consistent with the configuration of the somatic primordium observed previously and with the typical position of the AC at the center of the gonad [151] (schematic of the cell positions in the somatic primordium are shown in Fig. 5.1C).

Because the AC/VU decision is an intrinsically stochastic process, many animals need to be imaged in order to identify the sources of noise and to quantify its strength. Therefore, we imaged multiple animals and quantified the fluorescence intensity in the nuclei of the mother cells and the α cells. We observed high animal-to-animal variability in the dynamics of *lag-2* expression. In Fig. 5.8 six representative animals are presented.

Among animals in which the second-born α cell assumes the AC fate, the expression dynamics that results in this fate determination is highly variable. Three categories can be found. First, animals in which the second-born cell, right after division, shows higher expression than the first-born cell, and remains brighter during the full duration of the decision, eventually assuming the AC fate (Fig. 5.8A). Second, animals that show similar levels of expression between the two α cells, but in which the second-born α cell eventually becomes brighter and assumes the AC fate (Fig. 5.8B). Third, animals in which the second-born cell is initially dimmer, and only during the decision it increases its fluorescence above the other α cell and assumes the AC fate (Fig. 5.8C).

In some animals, the α cells are born at the same time, or at least within our temporal resolution (10 minutes). For example, in the animals shown in Fig. 5.8D, both α cells showed similar levels of YFP expression right after division, and only after few hours we observed differential fluorescence intensity.

Among animals in which the first-born α cell assumes the AC fate, the expression dynamics was diverse. In some cases the first-born α cell was already brighter right after division and remained brighter throughout the decision, therefore assuming the AC fate (Fig. 5.8E). In other cases the first-born α cell was initially dimmer, and only in the mid-L2 stage did the dimmer cell show an increase in fluorescence, eventually assuming the AC fate (Fig. 5.8F).

From these examples we conclude that the dynamics of *lag-2* expression during the AC/VU decision exhibits high animal-to-animal variability, even within animals with the same correlation between birth order and cell fate determination. To test the relevance of the birth order on the AC/VU decision, in the next section I will perform a quantitative study of the effect of the time between births of the α cells on the dynamics of the AC/VU decision.

5.3.3 Analysis of birth order and its effects

To analyze the effect of birth order on the AC/VU decision process, we analyzed the expression dynamics in N=42 animals. For each animal, we performed the quantitative analysis described in the previous section and extracted the normalized fluorescence difference $N(t)$. We found that in 48% of the animals (20/42), the anterior α cell (i.e. Z1.ppp) assumed the AC fate, while in 52% of the cases the posterior α cell (i.e. Z4.aaa) did (Fig. 5.9A). Therefore, each α cell has equal probability of assuming the AC or VU fate, consistent with previous results [143].

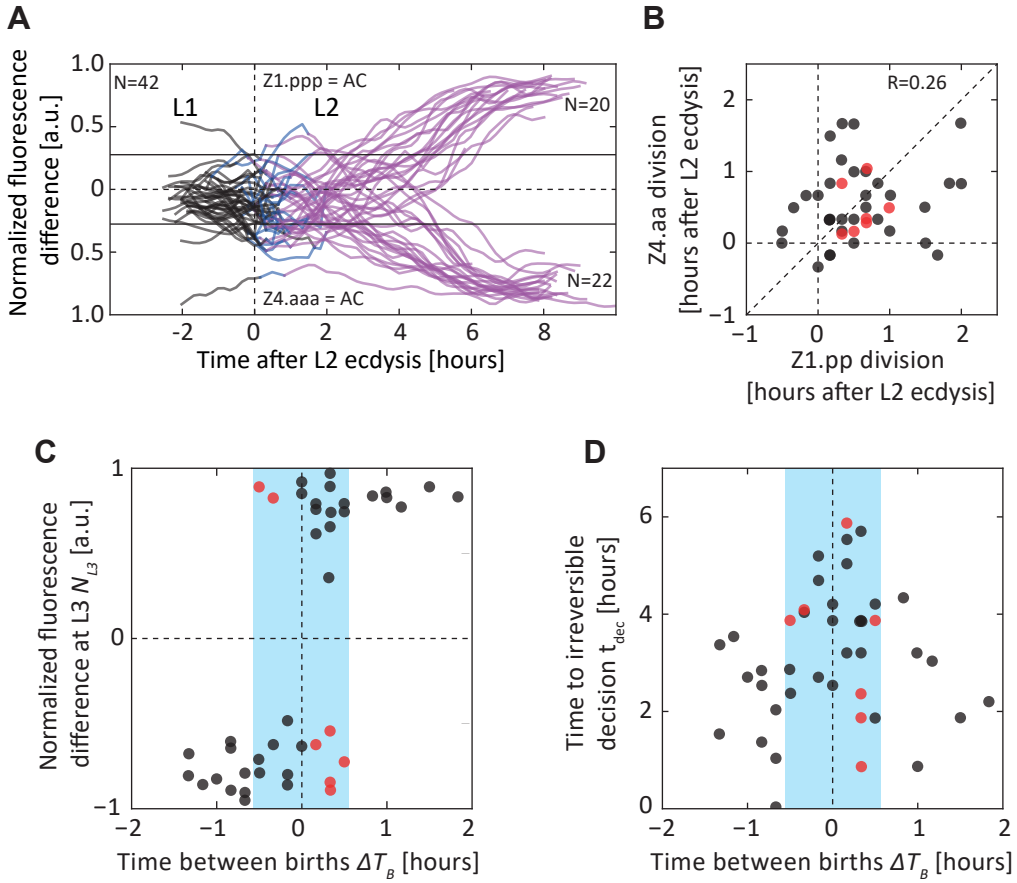

Figure 5.9: Analysis of birth order. (**A**) Normalized difference for N=42 animals. Data are shown upon filtering with a Gaussian filter with 15 minutes standard deviation. (**B**) Variability in time of division of Z1.pp and Z4.aa. Time is represented in hours after L2 ecdysis. (**C**) Normalized fluorescence difference at the L3 ecdysis as a function of the difference in time between births of the anterior and posterior α cells ΔT_B (i.e. $T_{\text{birth}}^{\text{Z1.ppp}} - T_{\text{birth}}^{\text{Z4.aaa}}$). Therefore, positive values represent animals in which Z4.aa divided before Z1.pp. (**D**) Time to irreversible decision as a function of ΔT_B. The time to irreversible decision is relative to the second division time and is computed as the last time at which the normalized difference crosses the $1/3$ or $-1/3$ threshold, represented by solid lines in Panel (A). In Panels (C) and (D), the light blue regions indicate animals in which the absolute value if the time between births $|\Delta T_B|$ is less than 30 minutes. In Panels (B), (C) and (D), red dots represent animals in which the first-born cell assumes the AC fate.

To quantify the animal-to-animal variability in the division time of the mother cells, we extracted the exact time of division relative to the L2 ecdysis. We found that both mother cell divisions occur on average right after the L2 ecdysis and showed animal-to-animal variability (0.53±0.65 hours for Z1.pp, 0.52±0.51 hours for Z4.aa). Next, we tested whether the division times of mother cells are synchronized, by comparing the division times within the same animal. We found that division

times of mother cells in the same animal weakly correlate (R=0.26) (Fig. 5.9B). Therefore, the birth order of the α is unbiased (in 18/42 animals Z1.pp divides first, in 21/42 animals Z4.aa divides first and in 3/42 animals mother cells divide within our temporal resolution).

To test whether birth order is a bias for the AC/VU decisions, we computed the difference in time between births of the anterior and posterior α cells ($\Delta T_B = T_{\text{birth}}^{\text{Z1.ppp}} - T_{\text{birth}}^{\text{Z4.aaa}}$) with the identity of the AC cell (Fig. 5.9C). To identify the AC cell, we used the value of the normalized fluorescence difference at the L3 ecdysis, N_{L3}, i.e. when the primordium is formed and the AC/VU decision is complete. A positive value of N_{L3} indicates that Z1.ppp assumed the AC fate, and a negative values of N_{L3} indicates that Z4.aaa did (Fig. 5.9A). We found that in most of the cases (32/42 animals, ~76%), the second-born α cell assumed the AC fate, while only in 7/42 cases (~17%) the AC fate was assumed by the first-born α cell. In 3/42 cases (~7%), cells divided within our temporal resolution, therefore we assumed that division happened at the same time. Moreover, we found that the first-born cell assumed the AC fate only in animals in which the absolute value of the time between births $|\Delta T_B|$ was shorter than 30 minutes (Fig. 5.9C, red dots lying in the light blue region). In 26% of the animals with $|\Delta T_B| < 30$ minutes, the first-born α cell assumed the AC fate (7/26 animals). When mother cells divided more than 30 minutes apart, the birth order predicts the cell fate decision with 100% accuracy, with the second-born α cell always assuming the AC fate (16/16 animals).

Therefore, while the birth order is the dominant noise source driving the AC/VU decision and greatly enhances the probability of the second-born cell to assume the AC fate, the probability that the first-born cell assumes the AC fate increases if the α cells are born at similar times. This raises the question whether the dynamics of the AC/VU decision depends on the time between births ΔT_B. For example, a variable that might be depending on ΔT_B is the time necessary to specify the cell fates. To test whether this is the case, we studied the time it takes for each animal to make an irreversible decision as a function of the time between births ΔT_B. In mathematics, this problem is called *last passage time*. Applied to our case, given the random variable $N(t)$ and a threshold N_{thr}, we define the time to an irreversible decision t_{dec} as:

$$t_{dec} = \begin{cases} \min\{\ t' \mid N(t) > N_{thr} \quad \forall\, t > t'\ \} & \text{if } N_{L3} > 0 \\ \min\{\ t' \mid N(t) < -N_{thr} \quad \forall\, t > t'\ \} & \text{if } N_{L3} < 0 \end{cases} \tag{5.2}$$

where N_{L3} represents the value of the normalized fluorescence intensity difference $N(t)$ at the time of the L3 ecdysis. The dependence of the definition of t_{dec} on N_{L3} is used to ensure that the proper threshold is used depending on whether Z1.ppp eventually assumes the AC fate ($N_{L3} > 0$) or Z4.aaa assumes the AC fate instead ($N_{L3} < 0$). To define the threshold N_{thr}, we chose the value of N at which one of the α cells is twice as bright as the other α cell, therefore:

$$N_{thr} = \frac{2-1}{2+1} = \frac{1}{3} \tag{5.3}$$

Moreover, the time to irreversible decision t_{dec} is measured relative to the time at which the second α cell is born.

We found that if the α cells are born at approximately the same time, the time to irreversible decision t_{dec} is on average larger than if they are born more far apart (3.6 ± 1.2 hours for $|\Delta T_B| \leq 30$ min, 2.2 ± 1.0 hours for$|\Delta T_B| > 30$ min). This could be explained with a model in which the birth order is only one of the sources of noise that are responsible for the AC/VU fate determination. Analyzing animals with $|\Delta T_B| < 30$ minutes is a way of studying AC/VU decision processes in which the strength of the predominant source of noise, birth order, is much reduced. As a consequence, in these cases the AC/VU decision must rely on other, possibly weaker, noise sources, therefore leading to a different dynamics of the cell fate specification.

In this section, we have shown that birth order is a strong bias for the AC/VU decision process. In particular, when the time between births of the α cells $|\Delta T_B|$ is higher than 30 minutes, the second-born α cell always assumes the AC fate. However, for $|\Delta T_B| < 30$ minutes, the AC/VU decision is more variable, as we observed that the AC fate was assumed by the first-born cell in ~26% of the animals. Moreover, we observed that the dynamics of *lag-2* expression in the α cells is dependent on the time between births ΔT_B, as in animals in which $|\Delta T_B| < 30$ minutes, the AC/VU mechanism takes on average a longer time to irreversibly specify the cell fates than in animals in which $|\Delta T_B| > 30$ minutes. This suggests that other sources of noise bias the AC/VU decision when α cells are born approximately at the same time. In the next section, I will perform a quantitative analysis aimed to identify such alternative noise sources.

5.3.4 Characterization of possible noise sources

Our smFISH experiments show that *lag-2* is already expressed in the mother cells, and that its expression levels are highly variable, both between different animals and between mother cells within the same animal (Section 5.2 and Fig. 5.4). In general, at the moment of division, the molecular content of a mother cell is partitioned between the two newly born daughter cells. In fact, we observed that, at the moment of division, *lag-2* mRNAs in the mother cells were partitioned over the α and β daughter cells (Fig. 5.10A). Because of the high variability in the expression levels of the mother cells, it is plausible to assume that α cells inherit different *lag-2* mRNA levels. Therefore, we wondered whether this variability could cause the two α cells to have different initial potentials of assuming the AC fate. That is, the variability in the number of *lag-2* mRNAs in the mother cells right before division might be the additional source of noise responsible for the AC/VU decision. As animals need to be fixed to perform smFISH experiments, it is not possible to answer this question from the analysis of the smFISH data. However, our time-lapse microscopy technique provides a tool to follow the expression levels in the mother cells and the consequences that it has on the AC/VU decision process. Specifically, in this section,

we want to test whether, for animals in which the α cells are born approximately at the same time, the AC fate is assumed by the α cell whose mother cell showed higher *lag-2* expression levels. To test this hypothesis, all the analysis shown in this section is performed only on the 26 animals in which the absolute value of the time between births $|\Delta T_B|$ is less than 30 minutes.

First, we quantified the fluorescence intensity of mother cells within the same animal in the *lag-2* transcriptional reporter strain (Fig. 5.10B). In particular, we quantified the fluorescence intensity in the mother cells averaged over the last hour prior to division, $\langle F_{\text{Z1.pp}} \rangle_{1h}$ and $\langle F_{\text{Z4.aa}} \rangle_{1h}$, and performed a correlation analysis between mother cells within the same animal. Similar to the variability observed on the number of *lag-2* mRNAs with smFISH, we found that both mother cells show high variability in expression levels, as measured in arbitrary units of absolute fluorescence intensity (2.7 ± 0.7 for Z1.pp and 3.6 ± 1.4 for Z4.aa). Moreover, we observed that the fluorescence intensity in mother cells within the same animal is only weakly correlated ($R = 0.25$), suggesting that the *lag-2* expression level in one mother cell do not depend on the expression level in the other mother cell.

We then tested whether such variability is a source of noise for the cell fate determination. To test this hypothesis, we computed the normalized fluorescence difference between the anterior and the posterior mother cell:

$$N_m = \langle F_{\text{Z1.pp}} \rangle_{1h} - \langle F_{\text{Z4.aa}} \rangle_{1h} \tag{5.4}$$

and correlated N_m with the normalized fluorescence difference between the two α cells at the L3 ecdysis, N_{L3} (Fig. 5.10C, black and red dots, N=26).

We found that in 50% of the animals (13/26), the mother cell of the future AC showed higher fluorescence intensity than the other mother cell. On the other hand, we found that in the other 50% of the animals, the α cell deriving from the brightest mother assumed the VU fate. This shows that the relative fluorescence intensity of the mother cells is not predictive of the cell fate determination for these animals. This is the case even for animals in which the first-born cell assumed the AC fate (Fig. 5.10B,C red dots). In fact, among these animals, we found cases in which the mother cell of the future VU cell showed higher fluorescence than the other mother cell (4/7). From this result, we conclude that the fluorescence level in the mother cells is not predictive of the final fates assumed by the α cells.

Next, we observed that, even though they are not involved in the AC/VU decision and invariantly assume the VU fate, β cells also show fluorescence intensity right after division. In particular, we observed that in many cases, α and β sister cells showed a similar fluorescence intensity dynamics right after birth, in most of the cases showing an increase in fluorescence in both cells, which eventually disappears in all the β cells, as they always assume the VU fate (Example shown in Fig. 5.11A). This observation is interesting for two distinct reasons. (i) The fact that α and β cells show similar expression dynamics right after division suggests that a common factor is regulating the expression at this stage. It is intriguing to hypothesize that the *lag-2* mRNA level inherited from the mother cell form this common factor. (ii) The fact

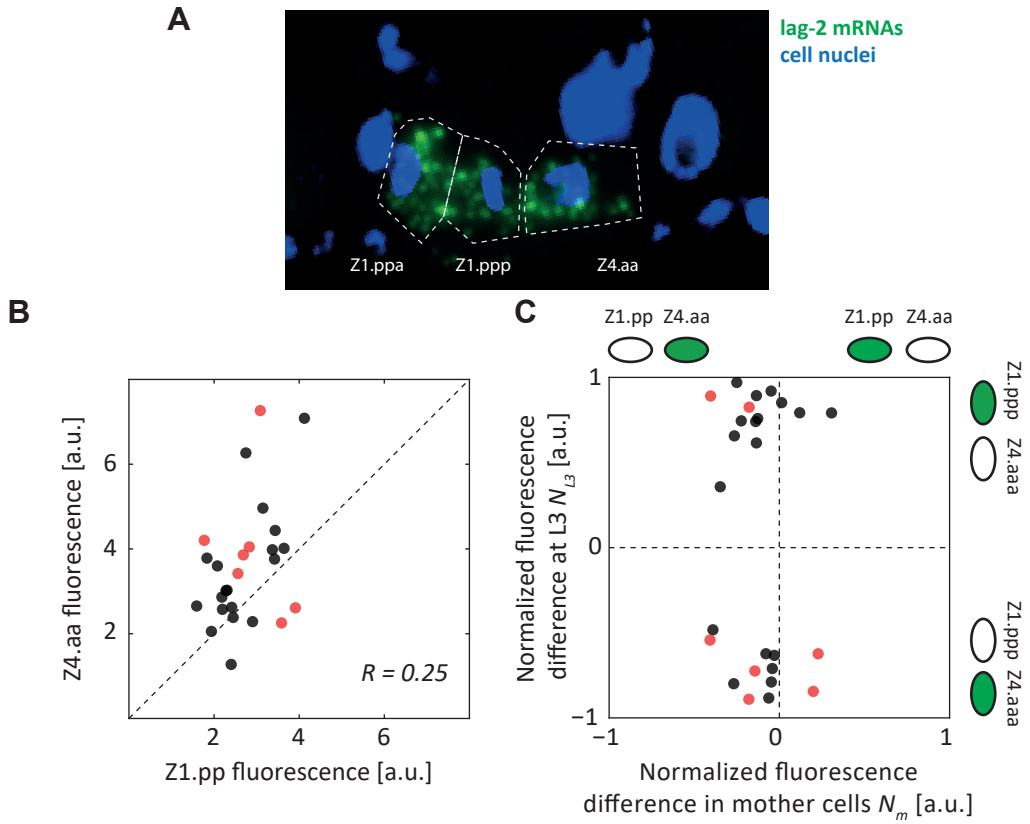

Figure 5.10: Analysis of the mother cell dynamics. (**A**) Distribution of *lag-2* mRNAs during a cell division showing cell nuclei (blue) and *lag-2* mRNAs (green). In the example, the Z1.pp cell is undergoing division. (**B**) Correlation of the fluorescence intensity in mother cells within the same animal prior to division. (**C**) Normalized fluorescence difference at the L3 ecdysis as a function of the normalized difference of the average fluorescence intensity of the mother cells. Results are shown only for animals in which the division time of the mother cells differs by less than half an hour. Schematic representations of the fluorescence in the mother and α cells is shown on the top and the right sides of the panel.

that the fluorescence increase shows cell-to-cell variability makes this a candidate for the additional source of noise responsible for the cell fate outcome when $|\Delta T_B| < 30$ minutes, i.e. when the strength of the predominant source of noise is reduced.

We therefore performed a quantitative analysis to test whether the *lag-2* expression dynamics of the α and β sister cells indeed shared some common patterns right after birth. We computed a linear fit of the time traces of both α and β cells for the hour after birth (Fig. 5.11A, green lines). We then quantified the dynamics of *lag-2* expression by measuring the rate of fluorescence increase, i.e. the slopes of the linear fit, for each α and β cell (e.g. $S_{\text{Z1.ppp}}$ and $S_{\text{Z1.ppa}}$). Then, we performed a correlation analysis to quantify to what extent the *lag-2* expression in the first hour after birth is similar in α and β sister cells (Fig. 5.11B).

According to the current model of the AC/VU decision, in which the β cells

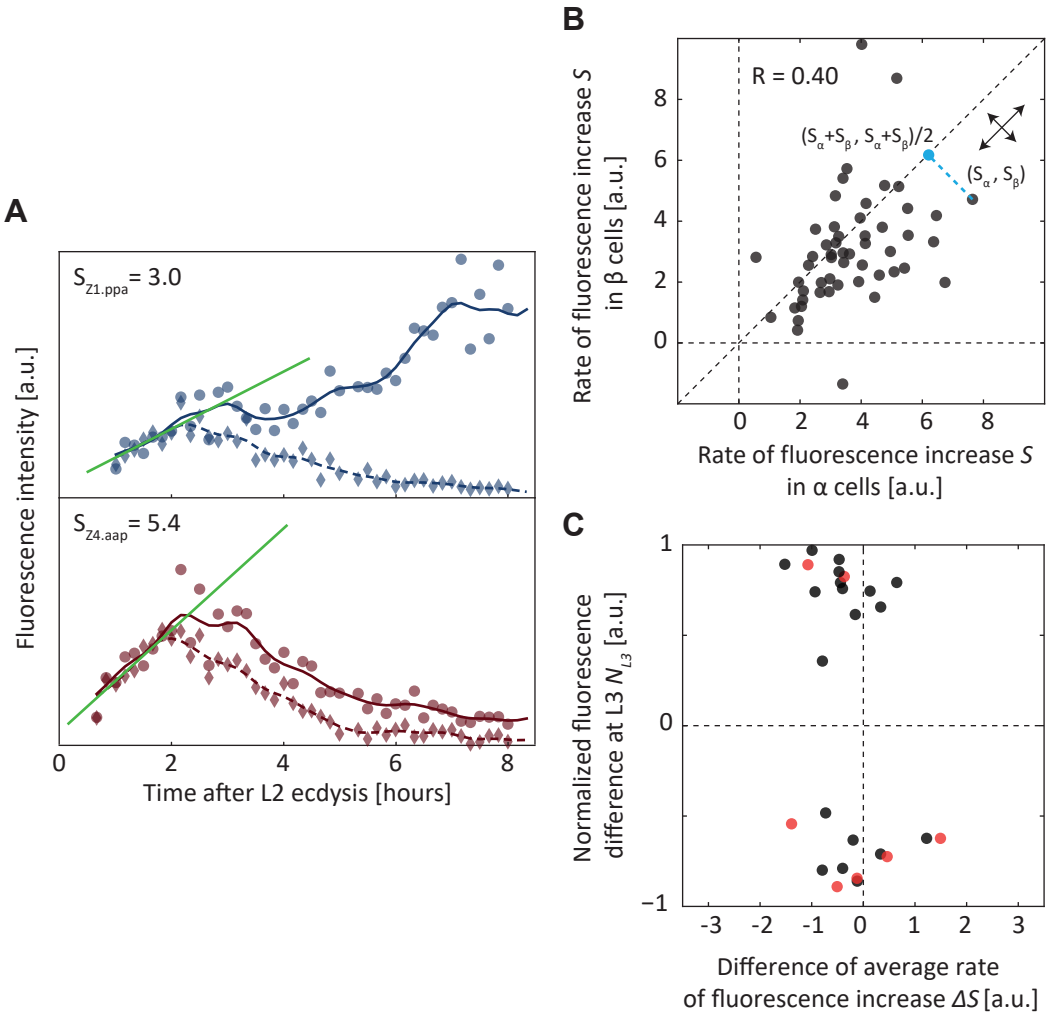

Figure 5.11: Analysis of the sister cell dynamics. (**A**) Example of a comparison between the dynamics of β and α sister cells. In the two panels, the fluorescence intensity is shown for the anterior (top) and posterior (bottom) α and β cells in the same animal. Raw data are indicated with circles (α cells) and diamonds (β cells). A Gaussian filter of the data is represented with solid (α cells) and dashed (β cells) lines. A linear fit of the fluorescence intensity of the β cells for the first hour after birth is indicated by green solid lines. From the linear fit, the rate of fluorescence increase of the β cells is extrapolated ($S_{Z1.ppa}$ and $S_{Z4.aap}$). (**B**) Correlation of the rate of fluorescence increase S between α and β sister cells in all the animals (N=26). The projection of a single point along the diagonal is shown (cyan dashed line and cyan dot). Orthogonal arrows indicate the directions of the spread of the points due to extrinsic (parallel to the diagonal) and intrinsic (perpendicular to the diagonal) noise. (**C**) Normalized fluorescence difference between the α cells at the L3 ecdysis (N_{L3}) as a function of the difference in the average rate of fluorescence increase in the α and β cells (ΔS) in the same animal. Red dots represent animals in which the first-born cell assumes the AC fate.

do not play any role in the AC/VU decision process, we expected to find very low values in the rate of fluorescence increase of the β cells S_β, even when the rate of fluorescence increase of the α cells S_α was high. However, with only one exception, we always found positive values of S_β for all the animals. Moreover, we found high variability in the values of both S_α and S_β. Inspired by the the quantitative analysis performed by Elowitz et al. [15], we interpreted our data in terms of intrinsic and extrinsic variability. In particular, we found considerable variability upon projection of all the data points along the diagonal. That is, we found high extrinsic variability (Example of a single projection is shown in Fig. 5.11B by the cyan dashed line and dot).

Extrinsic variability is described as the variability due to a common source of noise affecting both sister cells equally. Hence, we decided to test whether the variation along the diagonal can predict the cell fate outcome. To this end, we computed the average of the rate of fluorescence increase between the two anterior sister cells:

$$S_{ant} = \frac{S_{\text{Z1.ppp}} + S_{\text{Z1.ppa}}}{2} \tag{5.5}$$

and between the two posterior sister cells:

$$S_{post} = \frac{S_{\text{Z4.aaa}} + S_{\text{Z4.aap}}}{2} \tag{5.6}$$

in the same animal. Next, we computed the difference in average rate of fluorescence increase between the anterior and posterior sister cells:

$$\Delta S = S_{ant} - S_{post} \tag{5.7}$$

and performed a correlation analysis of ΔS with the normalized fluorescence difference at the L3 ecdysis N_{L3} (Fig. 5.11C).

We found that the difference in average rate of fluorescence increase of the α and β sister cells is not predictive of the cell fate determination. Even in animals in which the first-born cell assumes the AC fate, ΔS did not correlate with the final fate determination (red dots). In fact, against our hypothesis, in 4/7 animals the α cell showing an higher average rate of fluorescence increase eventually assumed the VU fate.

5.4 Conclusions

In this chapter, we studied a simple stochastic cell fate decision, the AC/VU decision, using two complementary techniques: smFISH and time-lapse microscopy. smFISH is an ideal tool to quantify the gene expression levels in single cells by counting the number of mRNAs. While with this technique it is possible to quantify the animal-to-animal variability in gene expression, it requires fixation of the animals. Therefore, it is not possible with this technique to follow single animals over time. However,

because of the strong stochastic nature of the AC/VU decision, the ability to follow the process in time is necessary to elucidate its dynamics. Thus, we complemented this technique using our new time-lapse microscopy approach. Specifically, we used a transcriptional reporter strain in which the promoter activity of the core component of the underlying gene regulatory network can be quantified with fluorescence microscopy. We then followed its expression over time and quantified the correlation between events happening at early stages of the AC/VU decision and the final outcome of the process. In this way, we aimed to determine the sources of variability that are responsible for the cell fate determination.

The AC/VU cell fate decision relies on the cell-cell interaction between two cells (here called α cells) to always produce one anchor cell (AC) and one ventral uterine cell (VU) in a mutually exclusive manner. This cell fate determination is mediated by the Notch signaling pathway, which relies on the expressions of the receptor *lin-12* and the ligand *lag-2*. With smFISH we found that (i) *lag-2* is also expressed by the mothers of the α cells, and that its expression levels are highly variable and (ii) the expression levels of *lag-2* and *lin-12* show different dynamics during the AC/VU decision. In particular, at the end of the decision process, *lag-2* is only expressed in the AC, while *lin-12* is still expressed in both α cells.

We then applied our new time-lapse microscopy approach to study the dynamics of expression of *lag-2* in multiple animals, because our smFISH results show that *lin-12* expression is less dynamic, i.e. is not restricted to a single α cell at any point of the AC/VU decision. We confirmed that, as previously shown, the birth order of the α cells strongly biases the cell fates, as in most of the animals analyzed the second-born α cell assumes the AC fate. However, birth order does not fully determine the outcome of the AC/VU decision, especially when the α cells are born approximately at the same time. In fact we observed that, among the animals in which the time between birth of the α cells is less than 30 minutes, the first-born cell assumes the AC fate in ~26% of animals. Moreover, by quantifying the time required to irreversibly determine the cell fates, we found that the decision process takes longer if the α cells are born at similar times.

The observation that the birth order does not fully correlate with the final outcome suggests that an additional source of noise biases the decision when the α cells are born at similar times. Our smFISH results show that some mother cells highly express *lag-2*, while other cells have lower *lag-2* expression. That is, *lag-2* expression in the mother cells shows high variability, even within the same animal. Upon division, a number of *lag-2* mRNAs are inherited by the α cells. Therefore the initial number of *lag-2* mRNAs in the α cells is also variable. This could represent the predominant source of noise responsible for the cell fate specification if the α cells are born at similar times.

We tested our hypothesis by correlating the expression dynamics in the mother cells with the final outcome of the process. We found that the *lag-2* expression levels measured by the YFP reporter strain in the mother cells did not correlate with the outcome. Next, we observed that for the next hour after birth, the fluorescence

intensity in the α cells correlates with that in their sister cells (here called β cells). In particular, we found that both α and β cells often show a fluorescence increase for the first hour after birth. This suggests that a common source of noise, possibly inherited from the mother cell, drives the expression dynamics of both cells right after division. We observed high variability in the rate of fluorescence increase right after birth. Therefore, we tested whether this variability is a quantity that correlates with the cell fate outcome. However, we did not find a correlation between the rate of increase right after birth and the final outcome.

Even though we did not find a correlation between the fluorescence intensity at early stages of the AC/VU decision and the cell fate outcome, our results are not conclusive and follow-up experiments will help identify the additional source of noise responsible for the cell fate determination in animals in which α cells are born at similar times. The most promising approach that will be tested in the future is the analysis of the AC/VU decision in mutant animals in which the activity of the core components of the gene regulatory network is affected. In particular, two questions can be answered. (i) How is the correlation between birth order and cell fate outcome affected in mutants in which the activity of a core component is elevated or suppressed? (ii) How is the *lag-2* dynamics affected by such mutations? Mutant strains already exist in which the activity of LIN-12 is either elevated or suppressed. Moreover, strains exist in which the *lin-12* gene is deleted or multiple copies of the same gene are inserted. Therefore, *lin-12* represents the most obvious choice as for the core component of the network to be perturbed. However, also the activities of other core components of the network, such as HLH-2 and *lag-2*, can be modified. For instance, RNA interference by bacterial feeding could be used to modify the activity of such components of the network and observe how the dynamics of the AC/VU decision process is perturbed.

Bibliography

[1] J. Hromkovič, *Design and Analysis of Randomized Algorithms. Introduction to Design Paradigms. Texts in Theoretical Computer Science, An EATCS Series*, 2005.

[2] J. M. Rist, *Epicurus: an introduction*, CUP Archive, 1972.

[3] L. E. Orgel, *The origin of life, a review of facts and speculations*, Trends in biochemical sciences **23**, 491 (1998).

[4] K. A. Maher and D. J. Stevenson, *Impact frustration of the origin of life*, (1988).

[5] R. Darwin Charles, *On the origin of species by means of natural selection, or the preservation of favoured races in the struggle for life*, Murray, London (1859).

[6] M. C. Weiss, F. L. Sousa, N. Mrnjavac, S. Neukirchen, M. Roettger, S. Nelson-Sathi, and W. F. Martin, *The physiology and habitat of the last universal common ancestor*, Nature Microbiology **1**, 16116 (2016).

[7] K. J. Locey and J. T. Lennon, *Scaling laws predict global microbial diversity*, Proceedings of the National Academy of Sciences , 201521291 (2016).

[8] C. Mora, D. P. Tittensor, S. Adl, A. G. Simpson, and B. Worm, *How many species are there on Earth and in the ocean?*, PLoS Biol **9**, e1001127 (2011).

[9] O. T. Avery, C. M. MacLeod, and M. McCarty, *Studies on the chemical nature of the substance inducing transformation of pneumococcal types induction of transformation by a desoxyribonucleic acid fraction isolated from pneumococcus type III*, The Journal of experimental medicine **79**, 137 (1944).

[10] J. D. Watson et al., *Molecular structure of nucleic acids*, Nature **171**, 737 (1953).

[11] F. Crick et al., *Central dogma of molecular biology*, Nature **227**, 561 (1970).

[12] A. Novick and M. Weiner, *Enzyme induction as an all-or-none phenomenon*, Proceedings of the National Academy of Sciences of the United States of America **43**, 553 (1957).

[13] M. Ko, H. Nakauchi, and N. Takahashi, *The dose dependence of glucocorticoid-inducible gene expression results from changes in the number of transcriptionally active templates.*, The EMBO Journal **9**, 2835 (1990).

[14] A. Arkin, J. Ross, and H. H. McAdams, *Stochastic kinetic analysis of developmental pathway bifurcation in phage λ-infected Escherichia coli cells*, Genetics **149**, 1633 (1998).

[15] M. B. Elowitz, A. J. Levine, E. D. Siggia, and P. S. Swain, *Stochastic gene expression in a single cell*, Science **297**, 1183 (2002).

[16] M. B. Elowitz and S. Leibler, *A synthetic oscillatory network of transcriptional regulators*, Nature **403**, 335 (2000).

[17] J. M. Raser and E. K. O'Shea, *Control of stochasticity in eukaryotic gene expression*, Science **304**, 1811 (2004).

[18] I. Golding, J. Paulsson, S. M. Zawilski, and E. C. Cox, *Real-time kinetics of gene activity in individual bacteria*, Cell **123**, 1025 (2005).

[19] A. Raj, C. S. Peskin, D. Tranchina, D. Y. Vargas, and S. Tyagi, *Stochastic mRNA synthesis in mammalian cells*, PLoS Biol **4**, e309 (2006).

[20] J. M. Pedraza and J. Paulsson, *Effects of molecular memory and bursting on fluctuations in gene expression*, Science **319**, 339 (2008).

[21] D. Volfson, J. Marciniak, W. J. Blake, N. Ostroff, L. S. Tsimring, and J. Hasty, *Origins of extrinsic variability in eukaryotic gene expression*, Nature **439**, 861 (2006).

[22] E. M. Ozbudak, M. Thattai, I. Kurtser, A. D. Grossman, and A. Van Oudenaarden, *Regulation of noise in the expression of a single gene*, Nature genetics **31**, 69 (2002).

[23] M. Ptashne and A. G. Switch, *Phage Lambda and Higher Organisms*, Cell & Blackwell Scientific, Cambridge, MA (1992).

[24] G. M. Süel, J. Garcia-Ojalvo, L. M. Liberman, and M. B. Elowitz, *An excitable gene regulatory circuit induces transient cellular differentiation*, Nature **440**, 545 (2006).

[25] J.-W. Veening, W. K. Smits, and O. P. Kuipers, *Bistability, epigenetics, and bet-hedging in bacteria*, Annu. Rev. Microbiol. **62**, 193 (2008).

[26] D. Schultz, P. G. Wolynes, E. B. Jacob, and J. N. Onuchic, *Deciding fate in adverse times: sporulation and competence in Bacillus subtilis*, Proceedings of the National Academy of Sciences **106**, 21027 (2009).

[27] R. S. Galhardo, P. J. Hastings, and S. M. Rosenberg, *Mutation as a stress response and the regulation of evolvability*, Critical reviews in biochemistry and molecular biology **42**, 399 (2007).

[28] G. M. Süel, R. P. Kulkarni, J. Dworkin, J. Garcia-Ojalvo, and M. B. Elowitz, *Tunability and noise dependence in differentiation dynamics*, Science **315**, 1716 (2007).

[29] H. Maamar, A. Raj, and D. Dubnau, *Noise in gene expression determines cell fate in Bacillus subtilis*, Science **317**, 526 (2007).

[30] T. D. Spector, F. Cicuttini, J. Baker, J. Loughlin, and D. Hart, *Genetic influences on osteoarthritis in women: a twin study*, Bmj **312**, 940 (1996).

[31] A. M. Arias and P. Hayward, *Filtering transcriptional noise during development: concepts and mechanisms*, Nature Reviews Genetics **7**, 34 (2006).

[32] A. Raj, S. A. Rifkin, E. Andersen, and A. van Oudenaarden, *Variability in gene expression underlies incomplete penetrance*, Nature **463**, 913 (2010).

[33] A. Roorda and D. R. Williams, *The arrangement of the three cone classes in the living human eye*, Nature **397**, 520 (1999).

[34] T. Gregor, D. W. Tank, E. F. Wieschaus, and W. Bialek, *Probing the limits to positional information*, Cell **130**, 153 (2007).

[35] D. Romaschoff, *Die Mutation Alae divergentes beiDrosophila funebris*, 1925.

[36] N. Timoféeff-Ressovsky, *Über den Einfluss des Genotypus auf das phänotypen Auftreten eines einzelnes Gens*, Journal für Psychologie und Neurologie **31**, 305 (1925).

[37] R. J. Johnston Jr and C. Desplan, *Stochastic mechanisms of cell fate specification that yield random or robust outcomes*, Annual review of cell and developmental biology **26**, 689 (2010).

[38] J. Nathans, *The evolution and physiology of human color vision: insights from molecular genetic studies of visual pigments*, Neuron **24**, 299 (1999).

[39] R. Vassar, J. Ngai, and R. Axel, *Spatial segregation of odorant receptor expression in the mammalian olfactory epithelium*, Cell **74**, 309 (1993).

[40] R. J. Johnston and C. Desplan, *Stochastic neuronal cell fate choices*, Current opinion in neurobiology **18**, 20 (2008).

[41] S. Brenner, *The genetics of Caenorhabditis elegans*, Genetics **77**, 71 (1974).

[42] S. Consortium et al., *Genome sequence of the nematode C. elegans: A platform for investigating biology*, Science **282**, 2012 (1998).

[43] J. Sulston, H. R. Horvitz, and J. Kimble, *APPENDIX 3 Cell Lineage*, Cold Spring Harbor Monograph Archive **17**, 457 (1988).

[44] J.-B. Pénigault and M.-A. Félix, *Evolution of a system sensitive to stochastic noise: P3. p cell fate in Caenorhabditis*, Developmental biology **357**, 419 (2011).

[45] E. R. Troemel, A. Sagasti, and C. I. Bargmann, *Lateral signaling mediated by axon contact and calcium entry regulates asymmetric odorant receptor expression in C. elegans*, Cell **99**, 387 (1999).

[46] J. Sulston and J. Hodgkin, *Methods, p 587–606*, The nematode Caenorhabditis elegans. Cold Spring Harbor Laboratory Press, Cold Spring Harbor, NY (1988).

[47] C. A. Giurumescu and A. D. Chisholm, *Cell identification and cell lineage analysis*, Methods in cell biology **106**, 325 (2011).

[48] S. Shaham, *WormBook: Methods in Cell Biology (January 02, 2006), WormBook, ed. The C. elegans Research Community, WormBook, doi/10.1895/wormbook. 1.49. 1*.

[49] F. K. Balagaddé, L. You, C. L. Hansen, F. H. Arnold, and S. R. Quake, *Long-term monitoring of bacteria undergoing programmed population control in a microchemostat*, Science **309**, 137 (2005).

[50] A. Groisman, C. Lobo, H. Cho, J. K. Campbell, Y. S. Dufour, A. M. Stevens, and A. Levchenko, *A microfluidic chemostat for experiments with bacterial and yeast cells*, Nature methods **2**, 685 (2005).

[51] E. Leclerc, Y. Sakai, and T. Fujii, *Cell culture in 3-dimensional microfluidic structure of PDMS (polydimethylsiloxane)*, Biomedical microdevices **5**, 109 (2003).

[52] D. C. Duffy, J. C. McDonald, O. J. Schueller, and G. M. Whitesides, *Rapid prototyping of microfluidic systems in poly (dimethylsiloxane)*, Analytical chemistry **70**, 4974 (1998).

[53] A. San-Miguel and H. Lu, *Microfluidics as a tool for C. elegans research*, (2005).

[54] M. F. Yanik, C. B. Rohde, and C. Pardo-Martin, *Technologies for micromanipulating, imaging, and phenotyping small invertebrates and vertebrates*, Annual review of biomedical engineering **13**, 185 (2011).

[55] S. E. Hulme, S. S. Shevkoplyas, J. Apfeld, W. Fontana, and G. M. Whitesides, *A microfabricated array of clamps for immobilizing and imaging C. elegans*, Lab on a Chip **7**, 1515 (2007).

[56] K. Chung, M. M. Crane, and H. Lu, *Automated on-chip rapid microscopy, phenotyping and sorting of C. elegans*, Nature methods **5**, 637 (2008).

[57] M. A. Unger, H.-P. Chou, T. Thorsen, A. Scherer, and S. R. Quake, *Monolithic microfabricated valves and pumps by multilayer soft lithography*, Science **288**, 113 (2000).

[58] J. Krajniak and H. Lu, *Long-term high-resolution imaging and culture of C. elegans in chip-gel hybrid microfluidic device for developmental studies*, Lab on a Chip **10**, 1862 (2010).

[59] K. Chung, M. Zhan, J. Srinivasan, P. W. Sternberg, E. Gong, F. C. Schroeder, and H. Lu, *Microfluidic chamber arrays for whole-organism behavior-based chemical screening*, Lab on a Chip **11**, 3689 (2011).

[60] M. Zimmer, J. M. Gray, N. Pokala, A. J. Chang, D. S. Karow, M. A. Marletta, M. L. Hudson, D. B. Morton, N. Chronis, and C. I. Bargmann, *Neurons detect increases and decreases in oxygen levels using distinct guanylate cyclases*, Neuron **61**, 865 (2009).

[61] M. M. Crane, K. Chung, and H. Lu, *Computer-enhanced high-throughput genetic screens of C. elegans in a microfluidic system*, Lab on a Chip **9**, 38 (2009).

[62] A. Ben-Yakar and F. Bourgeois, *Ultrafast laser nanosurgery in microfluidics for genome-wide screenings*, Current opinion in biotechnology **20**, 100 (2009).

[63] C.-C. J. Yu, D. M. Raizen, and C. Fang-Yen, *Multi-well imaging of development and behavior in Caenorhabditis elegans*, Journal of neuroscience methods **223**, 35 (2014).

[64] S. Uppaluri and C. P. Brangwynne, *A size threshold governs Caenorhabditis elegans developmental progression*, in *Proc. R. Soc. B*, volume 282, page 20151283, The Royal Society, 2015.

[65] J.-A. Conchello and J. W. Lichtman, *Optical sectioning microscopy*, Nature methods **2**, 920 (2005).

[66] E. G. Reynaud, U. Kržič, K. Greger, and E. H. Stelzer, *Light sheet-based fluorescence microscopy: More dimensions, more photons, and less photodamage*, HFSP journal **2**, 266 (2008).

[67] J. Mertz, *Optical sectioning microscopy with planar or structured illumination*, Nature methods **8**, 811 (2011).

[68] P. J. Keller, *Imaging morphogenesis: technological advances and biological insights*, Science **340**, 1234168 (2013).

[69] P. J. Keller, A. D. Schmidt, A. Santella, K. Khairy, Z. Bao, J. Wittbrodt, and E. H. Stelzer, *Fast, high-contrast imaging of animal development with scanned light sheet-based structured-illumination microscopy*, Nature methods **7**, 637 (2010).

[70] J. Huisken and D. Y. Stainier, *Selective plane illumination microscopy techniques in developmental biology*, Development **136**, 1963 (2009).

[71] J. Capoulade, M. Wachsmuth, L. Hufnagel, and M. Knop, *Quantitative fluorescence imaging of protein diffusion and interaction in living cells*, Nature biotechnology **29**, 835 (2011).

[72] U. Krzic, S. Gunther, T. E. Saunders, S. J. Streichan, and L. Hufnagel, *Multiview light-sheet microscope for rapid in toto imaging*, Nature methods **9**, 730 (2012).

[73] Y. Wu et al., *Spatially isotropic four-dimensional imaging with dual-view plane illumination microscopy*, Nature biotechnology **31**, 1032 (2013).

[74] R. Prevedel et al., *Simultaneous whole-animal 3D imaging of neuronal activity using light-field microscopy*, Nature methods **11**, 727 (2014).

[75] P. Rupprecht, R. Prevedel, F. Groessl, W. E. Haubensak, and A. Vaziri, *Optimizing and extending light-sculpting microscopy for fast functional imaging in neuroscience*, Biomedical optics express **6**, 353 (2015).

[76] T. Schrödel, R. Prevedel, K. Aumayr, M. Zimmer, and A. Vaziri, *Brain-wide 3D imaging of neuronal activity in Caenorhabditis elegans with sculpted light*, Nature methods **10**, 1013 (2013).

[77] R. Prevedel et al., *Fast volumetric calcium imaging across multiple cortical layers using sculpted light*, Nature Methods (2016).

[78] R. A. Kerr, *Imaging the activity of neurons and muscles*, (2006).

[79] A. Kocabas, C.-H. Shen, Z. V. Guo, and S. Ramanathan, *Controlling interneuron activity in Caenorhabditis elegans to evoke chemotactic behaviour*, Nature **490**, 273 (2012).

[80] S. Faumont et al., *An image-free opto-mechanical system for creating virtual environments and imaging neuronal activity in freely moving Caenorhabditis elegans*, PLoS One **6**, e24666 (2011).

[81] S. E. Hulme, S. S. Shevkoplyas, A. P. McGuigan, J. Apfeld, W. Fontana, and G. M. Whitesides, *Lifespan-on-a-chip: microfluidic chambers for performing lifelong observation of C. elegans*, Lab on a Chip **10**, 589 (2010).

[82] N. Chronis, M. Zimmer, and C. I. Bargmann, *Microfluidics for in vivo imaging of neuronal and behavioral activity in Caenorhabditis elegans*, Nature methods **4**, 727 (2007).

[83] F. Zeng, C. B. Rohde, and M. F. Yanik, *Sub-cellular precision on-chip small-animal immobilization, multi-photon imaging and femtosecond-laser manipulation*, Lab on a Chip **8**, 653 (2008).

[84] C. L. Gilleland, C. B. Rohde, F. Zeng, and M. F. Yanik, *Microfluidic immobilization of physiologically active Caenorhabditis elegans*, Nature protocols **5**, 1888 (2010).

[85] C. B. Rohde and M. F. Yanik, *Subcellular in vivo time-lapse imaging and optical manipulation of Caenorhabditis elegans in standard multiwell plates*, Nature communications **2**, 271 (2011).

[86] E. Kim, L. Sun, C. V. Gabel, and C. Fang-Yen, *Long-term imaging of Caenorhabditis elegans using nanoparticle-mediated immobilization*, PloS one **8**, e53419 (2013).

[87] H. Hwang, J. Krajniak, Y. Matsunaga, G. M. Benian, and H. Lu, *On-demand optical immobilization of Caenorhabditis elegans for high-resolution imaging and microinjection*, Lab on a Chip **14**, 3498 (2014).

[88] C. I. Bargmann, *Chemosensation in C. elegans*, (2006).

[89] A. J. Bretscher, K. E. Busch, and M. de Bono, *A carbon dioxide avoidance behavior is integrated with responses to ambient oxygen and food in Caenorhabditis elegans*, Proceedings of the National Academy of Sciences **105**, 8044 (2008).

[90] M. Chalfie, J. E. Sulston, J. G. White, E. Southgate, J. N. Thomson, and S. Brenner, *The neural circuit for touch sensitivity in Caenorhabditis elegans*, The Journal of neuroscience **5**, 956 (1985).

[91] E. A. Hallem and P. W. Sternberg, *Acute carbon dioxide avoidance in Caenorhabditis elegans*, Proceedings of the National Academy of Sciences **105**, 8038 (2008).

[92] J. Clausell-Tormos et al., *Droplet-based microfluidic platforms for the encapsulation and screening of mammalian cells and multicellular organisms*, Chemistry & biology **15**, 427 (2008).

[93] W. Shi, J. Qin, N. Ye, and B. Lin, *Droplet-based microfluidic system for individual Caenorhabditis elegans assay*, Lab on a Chip **8**, 1432 (2008).

[94] H. Bringmann, *Agarose hydrogel microcompartments for imaging sleep- and wake-like behavior and nervous system development in Caenorhabditis elegans larvae*, Journal of neuroscience methods **201**, 78 (2011).

[95] J. L. Drury and D. J. Mooney, *Hydrogels for tissue engineering: scaffold design variables and applications*, Biomaterials **24**, 4337 (2003).

[96] I. Wong, S. Atsumi, W.-C. Huang, T.-Y. Wu, T. Hanai, M.-L. Lam, P. Tang, J. Yang, J. C. Liao, and C.-M. Ho, *An agar gel membrane-PDMS hybrid microfluidic device for long term single cell dynamic study*, Lab on a Chip **10**, 2710 (2010).

[97] S. Takeuchi, W. R. DiLuzio, D. B. Weibel, and G. M. Whitesides, *Controlling the shape of filamentous cells of Escherichia coli*, Nano letters **5**, 1819 (2005).

[98] J. R. Moffitt, J. B. Lee, and P. Cluzel, *The single-cell chemostat: an agarose-based, microfluidic device for high-throughput, single-cell studies of bacteria and bacterial communities*, Lab on a chip **12**, 1487 (2012).

[99] W.-J. Chi, Y.-K. Chang, and S.-K. Hong, *Agar degradation by microorganisms and agar-degrading enzymes*, Applied microbiology and biotechnology **94**, 917 (2012).

[100] J. R. Tse and A. J. Engler, *Preparation of hydrogel substrates with tunable mechanical properties*, Current protocols in cell biology , 10 (2010).

[101] R. J. Pelham and Y.-l. Wang, *Cell locomotion and focal adhesions are regulated by substrate flexibility*, Proceedings of the National Academy of Sciences **94**, 13661 (1997).

[102] J. D. Mih, A. S. Sharif, F. Liu, A. Marinkovic, M. M. Symer, and D. J. Tschumperlin, *A multiwell platform for studying stiffness-dependent cell biology*, PloS one **6**, e19929 (2011).

[103] Y. Tanaka, K. Fukao, and Y. Miyamoto, *Fracture energy of gels*, The European Physical Journal E **3**, 395 (2000).

[104] P. Nghe, S. Boulineau, S. Gude, P. Recouvreux, J. S. van Zon, and S. J. Tans, *Microfabricated polyacrylamide devices for the controlled culture of growing cells and developing organisms*, PloS one **8**, e75537 (2013).

[105] N. MicroChem, *Su-8, Negative Tone Photoresist Formulations 50-100, 4 pages, Feb. 2002*.

[106] A. Ward, J. Liu, Z. Feng, and X. S. Xu, *Light-sensitive neurons and channels mediate phototaxis in C. elegans*, Nature neuroscience **11**, 916 (2008).

[107] P. Sarder and A. Nehorai, *Deconvolution methods for 3-D fluorescence microscopy images*, IEEE Signal Processing Magazine **23**, 32 (2006).

[108] M. Sezgin et al., *Survey over image thresholding techniques and quantitative performance evaluation*, Journal of Electronic imaging **13**, 146 (2004).

[109] L. Byerly, R. Cassada, and R. Russell, *The life cycle of the nematode Caenorhabditis elegans: I. Wild-type growth and reproduction*, Developmental biology **51**, 23 (1976).

[110] A. J. Schindler, L. R. Baugh, and D. R. Sherwood, *Identification of late larval stage developmental checkpoints in Caenorhabditis elegans regulated by insulin/IGF and steroid hormone signaling pathways*, PLoS Genet **10**, e1004426 (2014).

[111] A. J. Schindler and D. R. Sherwood, *Should I stay or should I go? Identification of novel nutritionally regulated developmental checkpoints in C. elegans*, in *Worm*, volume 3, page e979658, Taylor & Francis, 2014.

[112] C. M. Croce and G. A. Calin, *miRNAs, cancer, and stem cell division*, Cell **122**, 6 (2005).

[113] T. Xie and A. C. Spradling, *decapentaplegic is essential for the maintenance and division of germline stem cells in the Drosophila ovary*, Cell **94**, 251 (1998).

[114] X. Song, C.-H. Zhu, C. Doan, and T. Xie, *Germline stem cells anchored by adherens junctions in the Drosophila ovary niches*, Science **296**, 1855 (2002).

[115] J. Beckmann, S. Scheitza, P. Wernet, J. C. Fischer, and B. Giebel, *Asymmetric cell division within the human hematopoietic stem and progenitor cell compartment: identification of asymmetrically segregating proteins*, Blood **109**, 5494 (2007).

[116] T. G. Nystul and A. C. Spradling, *Breaking out of the mold: diversity within adult stem cells and their niches*, Current opinion in genetics & development **16**, 463 (2006).

[117] S. J. Morrison and A. C. Spradling, *Stem cells and niches: mechanisms that promote stem cell maintenance throughout life*, Cell **132**, 598 (2008).

[118] D. Hirsh, D. Oppenheim, and M. Klass, *Development of the reproductive system of Caenorhabditis elegans*, Developmental biology **49**, 200 (1976).

[119] E. J. A. Hubbard and D. Greenstein, *Introduction to the germ line*, (2005).

[120] P. M. Joshi, M. R. Riddle, N. J. Djabrayan, and J. H. Rothman, *Caenorhabditis elegans as a model for stem cell biology*, Developmental Dynamics **239**, 1539 (2010).

[121] G. Shemer and B. Podbilewicz, *Fusomorphogenesis: cell fusion in organ formation*, Developmental Dynamics **218**, 30 (2000).

[122] J. E. Sulston and H. R. Horvitz, *Post-embryonic cell lineages of the nematode, Caenorhabditis elegans*, Developmental biology **56**, 110 (1977).

[123] E. G. Moss, *Heterochronic genes and the nature of developmental time*, Current Biology **17**, R425 (2007).

[124] X. Huang, E. Tian, Y. Xu, and H. Zhang, *The C. elegans engrailed homolog ceh-16 regulates the self-renewal expansion division of stem cell-like seam cells*, Developmental biology **333**, 337 (2009).

[125] T. Kanamori, T. Inoue, T. Sakamoto, K. Gengyo-Ando, M. Tsujimoto, S. Mitani, H. Sawa, J. Aoki, and H. Arai, *β-Catenin asymmetry is regulated by PLA1 and retrograde traffic in C. elegans stem cell divisions*, The EMBO journal **27**, 1647 (2008).

[126] C. S. Thummel, *Flies on steroids-Drosophila metamorphosis and the mechanisms of steroid hormone action*, Trends in Genetics **12**, 306 (1996).

[127] J. C. Dunlap, *Molecular bases for circadian clocks*, Cell **96**, 271 (1999).

[128] J. Bass and J. S. Takahashi, *Circadian integration of metabolism and energetics*, Science **330**, 1349 (2010).

[129] O. Pourquié, *The segmentation clock: converting embryonic time into spatial pattern*, Science **301**, 328 (2003).

[130] G. C. Monsalve and A. R. Frand, *Toward a unified model of developmental timing: A molting approach*, in *Worm*, volume 1, pages 221–230, Taylor & Francis, 2012.

[131] V. Ambros and H. Horvitz, *Heterochronic mutants of the nematode*, Science **226**, 409 (1984).

[132] A. E. Rougvie and E. G. Moss, *Developmental transitions in C. elegans larval stages*, Curr Top Dev Biol **105**, 153 (2013).

[133] M. Jeon, H. F. Gardner, E. A. Miller, J. Deshler, and A. E. Rougvie, *Similarity of the C. elegans developmental timing protein LIN-42 to circadian rhythm proteins*, Science **286**, 1141 (1999).

[134] G. C. Monsalve, C. Van Buskirk, and A. R. Frand, *LIN-42/PERIOD controls cyclical and developmental progression of C. elegans molts*, Current Biology **21**, 2033 (2011).

[135] J. E. Abrahante, E. A. Miller, and A. E. Rougvie, *Identification of heterochronic mutants in Caenorhabditis elegans: temporal misexpression of a collagen:: green fluorescent protein fusion gene*, Genetics **149**, 1335 (1998).

[136] G.-J. Hendriks, D. Gaidatzis, F. Aeschimann, and H. Großhans, *Extensive oscillatory gene expression during C. elegans larval development*, Molecular cell **53**, 380 (2014).

[137] D. hyun Kim, D. Grün, and A. van Oudenaarden, *Dampening of expression oscillations by synchronous regulation of a microRNA and its target*, Nature genetics **45**, 1337 (2013).

[138] V. S. Meli, B. Osuna, G. Ruvkun, and A. R. Frand, *MLT-10 defines a family of DUF644 and proline-rich repeat proteins involved in the molting cycle of Caenorhabditis elegans*, Molecular biology of the cell **21**, 1648 (2010).

[139] G. Aspöck, H. Kagoshima, G. Niklaus, and T. R. Bürglin, *Caenorhabditis elegans has scores of hedgehogrelated genes: sequence and expression analysis*, Genome research **9**, 909 (1999).

[140] A. R. Frand, S. Russel, and G. Ruvkun, *Functional genomic analysis of C. elegans molting*, PLoS Biol **3**, e312 (2005).

[141] M. Wildwater, N. Sander, G. de Vreede, and S. van den Heuvel, *Cell shape and Wnt signaling redundantly control the division axis of C. elegans epithelial stem cells*, Development **138**, 4375 (2011).

[142] R. Singh and J. Sulston, *Some observations on moulting in Caenorhabditis elegans*, Nematologica **24**, 63 (1978).

[143] J. Kimble and D. Hirsh, *The postembryonic cell lineages of the hermaphrodite and male gonads in Caenorhabditis elegans*, Developmental biology **70**, 396 (1979).

[144] M. D. Sallee, T. Aydin, and I. Greenwald, *Influences of LIN-12/Notch and POP-1/TCF on the Robustness of Ventral Uterine Cell Fate Specification in Caenorhabditis elegans Gonadogenesis*, G3: Genes| Genomes| Genetics **5**, 2775 (2015).

[145] G. Seydoux, T. Schedl, and I. Greenwald, *Cell-cell interactions prevent a potential inductive interaction between soma and germline in C. elegans*, Cell **61**, 939 (1990).

[146] J. Kimble, *Alterations in cell lineage following laser ablation of cells in the somatic gonad of Caenorhabditis elegans*, Developmental biology **87**, 286 (1981).

[147] G. Seydoux and I. Greenwald, *Cell autonomy of lin-12 function in a cell fate decision in C. elegans*, Cell **57**, 1237 (1989).

[148] I. S. Greenwald, P. W. Sternberg, and H. R. Horvitz, *The lin-12 locus specifies cell fates in Caenorhabditis elegans*, Cell **34**, 435 (1983).

[149] R. Kopan and M. X. G. Ilagan, *The canonical Notch signaling pathway: unfolding the activation mechanism*, Cell **137**, 216 (2009).

[150] I. Greenwald and G. Seydoux, *Analysis of gain-of-function mutations of the lin-12 gene of Caenorhabditis elegans*, (1990).

[151] H. A. Wilkinson, K. Fitzgerald, and I. Greenwald, *Reciprocal changes in expression of the receptor lin-12 and its ligand lag-2 prior to commitment in a C. elegans cell fate decision*, Cell **79**, 1187 (1994).

[152] H. A. Wilkinson and I. Greenwald, *Spatial and temporal patterns of lin-12 expression during C. elegans hermaphrodite development.*, Genetics **141**, 513 (1995).

[153] D. Levitan and I. Greenwald, *LIN-12 protein expression and localization during vulval development in C. elegans*, Development **125**, 3101 (1998).

[154] X. Karp and I. Greenwald, *Post-transcriptional regulation of the E/Daughterless ortholog HLH-2, negative feedback, and birth order bias during the AC/VU decision in C. elegans*, Genes & development **17**, 3100 (2003).

[155] X. Karp and I. Greenwald, *Multiple roles for the E/Daughterless ortholog HLH-2 during C. elegans gonadogenesis*, Developmental biology **272**, 460 (2004).

[156] V. Ambros, *Cell cycle-dependent sequencing of cell fate decisions in Caenorhabditis elegans vulva precursor cells*, Development **126**, 1947 (1999).

[157] A. Raj and S. Tyagi, *Detection of individual endogenous RNA transcripts in situ using multiple singly labeled probes*, Methods in enzymology **472**, 365 (2010).

Summary

The development of multi-cellular organisms is an incredibly complex sequence of tightly coordinated events that starts from a single fertilized cell and ends in an adult organism capable of reproduction. All individuals within the same species are remarkably similar, and mistakes rarely occur during their development. An active research area of developmental biology is devoted to understanding what are the underlying molecular mechanisms that generate such robustness.

However, stochastic molecular fluctuations, often called *noise*, are omnipresent in biology. Random diffusion of molecules and the probabilistic nature of chemical reactions cause all the fundamental biological processes, such as gene expression, to be intrinsically stochastic. Recently, it has been shown, for instance in bacteria, that such fluctuations can ultimately impact the behavior of an entire cell. As a consequence, genetically identical cells exhibit strongly variable responses to external inputs, even when subject to identical environmental conditions. Noise is also present in developmental processes of multi-cellular organisms. Recently, several examples demonstrated how developmental processes are affected by noise. In some of these cases, developmental processes are adapted to suppress noise, for example in the embryonic cell fate patterning of the fruit fly *Drosophila melanogaster*. In contrast, other examples exist in which development is thought to be driven by molecular noise, for instance during stochastic cell fate decisions.

The existence of noise in development raises a number of fundamental questions: (i) What are the different sources of noise that impact development? What are the relative strengths of such noise sources? (ii) How is noise suppressed in developmental processes to achieve a robust outcome? (iii) Do developmental processes exist that are driven by molecular noise? If so, how are small molecular fluctuations amplified to impact the behavior of entire cells in developing organisms?

While a molecular biology approach has been highly successful in revealing the key molecular players involved in development, a more quantitative approach is needed to study their variability on the single-cell level. Moreover, to study a process as highly dynamic as development, an approach is needed to follow developmental processes over time. To this end, one needs to follow developing organisms with enough spatial and temporal resolution to detect the dynamics of the process at the

single-cell level. However, many of the model systems for studying development, such as fruit flies, zebrafish and mice, have a large body size and a relatively slow development. Therefore, in these model organisms experiments able to follow their development with single-cell resolution are currently extremely challenging, if not impossible.

In this thesis, we use the nematode *Caenorhanditis elegans* to study the role of noise in development. *C. elegans* is an ideal model system for developmental studies, because of its short life cycle, simple genetics and simple body plan. *C. elegans* also represents a unique model system to study the role of noise in development, for two main reasons. First, *C. elegans* development is largely invariant, meaning that almost all cells divide and differentiate in a stereotypical manner. Hence, *C. elegans* development is extremely robust, making it an ideal model system to study how molecular noise is efficiently suppressed during development. In this thesis, we did not directly examine mechanisms of noise suppression, but, as a starting point, we characterized the levels of variability in two developmental processes that show an invariant outcome. Second, a number of stochastic cell fate decisions occur during *C. elegans* development. Therefore, it also represents an ideal model system to study how small and continuous fluctuations are translated into digital cell fate decisions impacting the entire cell. In this thesis, we address this question by studying one specific stochastic cell fate decision, the so-called AC/VU decision. As an essential requirement to perform these studies, we developed a new time-lapse microscopy technique able to follow the full post-embryonic development of *C. elegans* in multiple animals in parallel with high temporal resolution and single-cell spatial resolution, something that was so far not possible.

In Chapter 2, I describe in detail our novel time-lapse microscopy approach, which relies on (i) confining *C. elegans* larvae in microfabricated chambers with enough food to sustain development and enough space to freely move, (ii) a microscopy setup optimized for fast image acquisition and (iii) image analysis to extract the dynamics of developmental processes at the whole organism level as well as at the single-cell level. In particular, I first describe in detail the design and the protocols used to create the microfabricated chambers. Next, I focus on the design and the performances of the imaging setup. Finally, I prove that *C. elegans* larvae develop normally in our microfabricated chambers. To this end, I characterized development of multiple animals, confined in chambers of different dimensions, by quantifying three markers of developmental progression: growth rate, body elongation and larval stage duration. Importantly, the data on *C. elegans* growth might form a starting point for future studies aimed to elucidate the effect of food availability and diet on development.

In Chapter 3, I test the capability of our setup to follow the dynamics of single cells in animals developing in the microfabricated chambers. In particular, I performed lineage analysis of seam cells, a model system for stem cell-like behavior, in multiple animals over the full post-embryonic development. To this end, I used fluorescence time-lapse microscopy of animals in which seam cell nuclei are

fluorescently labeled. First, I performed a quantitative analysis of the time of division of all the seam cells in multiple wild-type animals. I found that some seam cells divide on average before others, suggesting that lineage-dependent temporal cues are responsible for the temporal regulation of seam cell divisions. Next, I measured the variability in timing of seam cell divisions in this developmental process that otherwise has an invariant outcome. Moreover, I repeated the lineaging analysis in mutant animals in which the seam cells do not follow the stereotypical division pattern. In this case, I show that cell division mistakes occur more often in specific seam cell lineages and at particular stages, suggesting that stage- and lineage-specific mechanisms are responsible for the correct execution of the seam cell divisions. In general, the ability to perform full lineage analysis in multiple animals will be used in the future to elucidate the temporal cues and the mechanisms responsible for correct seam cell divisions.

In Chapter 4, I demonstrate the capability of our setup to quantify the dynamics of gene expression, down to the single-cell level. To this end, I measured the variability in the expression levels of two genes that have been previously shown to oscillate over the course of development. *C. elegans* development is divided in four larval stages, punctuated by molts, during which a new skin is synthesized and the old skin is shed. Genes that oscillate during development show four distinct peaks, once every larval stage. Using fluorescence time-lapse microscopy in transcriptional reporter strains, I quantified the oscillation dynamics of one gene that is expressed in the whole body of the animal and another gene that is exclusively expressed in the seam cell nuclei. For both genes, I found that the timing of the peaks of expression show significant animal-to-animal variability. However, the peak times were found to be strongly correlated with the time of the closest molt, suggesting that the times of the peaks of expression as well as the times of the molts are all impacted by noise generated by a common source. In the future, our technique will likely contribute to understanding the mechanisms that generate these oscillations.

In Chapter 5, I apply our approach to the study of a model system for stochastic cell fate decisions: the AC/VU decision. During the AC/VU decision two cells, referred to as α cells, are born identical but differentiate in a mutually exclusive manner into one *anchor cell* (AC) and one *ventral uterine* (VU) cell. Interestingly, the outcome of the decision process is variable, in that each α cell has equal probability of assuming the AC or VU fate. The hypothesis is that initial fluctuations at the molecular level are responsible to drive the decision process, making the AC/VU decision an ideal model system to study how continuous fluctuations are translated into discrete cell fates. Even though the molecular mechanisms of the system have been extensively studied, using our time-lapse microscopy approach we can now follow the dynamics of the process for the first time. Therefore, our approach has the potential to gain significant new insights into the mechanism underlying the AC/VU decision. In this chapter, we aimed to elucidate the sources of noise responsible for the cell fate determination. In particular, we examined two possible sources of noise: the birth order of the α cells and the stochastic expression of *lag-2*, one of

the key components of the underlying gene regulatory network. First, we studied the variability in the time of birth of the α cells. We confirmed that, as previously shown, birth order strongly correlates with the outcome, in that the second-born α cell has greater probability of assuming the AC fate. However, we found that if the α cells are born at similar times, occasionally the first-born cell assumes the AC fate. Therefore additional sources of noise must become more important when the α cells are born at similar times. We explored whether the stochastic expression of *lag-2* before the time of births of the α cells, i.e. in their mother cells, could form this additional source of noise and, hence, bias the decision when the α cells are born at similar times. However, we found that this is not the case, leaving the identity of the additional sources of noise an open question. In the future, we will use our technique to further elucidate the dynamics of the AC/VU decision and to identify such additional sources of noise.

Samenvatting

De ontwikkeling van meercellige organismen is een ongelooflijk complexe serie van nauw gecoördineerde gebeurtenissen die begint bij een enkele bevruchtte cel en eindigt bij een volwassen organisme dat in staat is tot reproductie. Alle individuen binnen dezelfde soort zijn opvallend eenvormig en fouten komen nauwelijks voor tijdens de ontwikkeling. Een actief onderzoeksveld binnen de ontwikkelingsbiologie is gewijd aan het begrijpen van de onderliggende moleculaire mechanisme die deze robuustheid genereren.

Echter, stochastische moleculaire fluctuaties, vaak *ruis* genoemd, zijn alomtegenwoordig in de biologie. Willekeurige diffusie van moleculen en de probabilistische aard van chemische reacties veroorzaken dat alle fundamentele biologische processen, zoals genexpressie, intrinsiek stochastisch zijn. Onlangs is aangetoond, bijvoorbeeld in bacteriën, dat zulke fluctuaties uiteindelijk het gedrag van de gehele cel kunnen beïnvloeden. Hierdoor kunnen genetisch identieke cellen sterk variërende reacties vertonen op externe signalen, zelfs wanneer deze zich in identieke omgevingscondities bevinden. Ruis is ook aanwezig in het ontwikkelingsproces van meercellige organismen. Onlangs hebben verschillende voorbeelden getoond hoe ontwikkelingsprocessen beïnvloed worden door ruis. In sommige van deze gevallen worden de ontwikkelingsprocessen aangepast om ruis te onderdrukken, bijvoorbeeld bij het ontstaan van ruimtelijke patronen van verschillende celtypen in embryo's van de fruitvlieg *Drosophila melanogaster*. Tegelijkertijd bestaan er ook andere voorbeelden waarbij men denkt dat ontwikkeling juist gedreven wordt door moleculaire ruis, zoals bijvoorbeeld tijdens celtype-beslissingen die een stochastische uitkomst hebben.

Het bestaan van ruis in ontwikkeling roept verschillende fundamentele vragen op: (i) Wat zijn de verschillende bronnen van de ruis die invloed hebben op de ontwikkeling? Wat zijn de relatieve sterkten van zulke ruisbronnen? (ii) Hoe wordt ruis onderdrukt in een ontwikkelingsproces om een robuust resultaat te verkrijgen? (iii) Bestaan er ontwikkelingsprocessen die gedreven worden door moleculaire ruis? Zo ja, hoe worden kleine moleculaire fluctuaties zo versterkt dat zij het gedrag van de gehele cel binnen een zich ontwikkelend organisme kunnen beïnvloeden?

Ondanks dat de aanpak van de moleculaire biologie zeer succesvol is in het openbaren van de moleculaire hoofdrolspelers die betrokken zijn bij de ontwikkeling,

is een meer kwantitatieve aanpak nodig om de rol van variabiliteit op het niveau van individuele cellen te onderzoeken. Bovendien, om een proces te bestuderen dat zo dynamisch is als ontwikkeling is een aanpak nodig om ontwikkelingsprocessen in tijd te kunnen volgen. Om die reden moet men organismen tijdens de ontwikkeling met genoeg ruimtelijke en tijdsresolutie kunnen volgen om de dynamica van het proces op cel-niveau cellen te kunnen vastleggen. Echter, de meeste modelsystemen die worden gebruikt voor de studie van ontwikkeling, zoals fruitvliegen, zebravissen, en muizen, hebben een grote lichaamsomvang en een relatief langzame ontwikkeling. Om die reden zijn experimenten die het gedrag van enkele cellen tijdens de ontwikkeling van deze modelorganismen volgen uitermate uitdagend, zo niet onmogelijk.

In dit proefschrift gebruiken wij de nematode worm *Caenorhabditis elegans* om de rol van ruis in ontwikkeling te bestuderen. *C. elegans* is een ideaal model system voor ontwikkelingsstudies, door de korte levenscyclus, de simpele genetica en de eenvoudige lichaamsbouw. *C. elegans* vormt ook een uniek model systeem om de rol van ruis in ontwikkeling te bestuderen, om twee redenen. Ten eerste is de ontwikkeling van *C. elegans* grotendeels invariant, wat wil zeggen dat vrijwel alle cellen delen en differentiëren op een stereotype wijze. Dit betekent dat de ontwikkeling van *C. elegans* buitengewoon robuust is en maakt het daarom tot een ideaal modelsysteem om te onderzoeken hoe moleculaire ruis efficiënt onderdrukt wordt tijdens ontwikkeling. In dit proefschrift hebben wij niet direct de mechanismen van ruisonderdrukking onderzocht, maar hebben wij, als uitgangspunt, de hoeveelheid variabiliteit gekarakteriseerd in twee ontwikkelingsprocessen die een verder invariante uitkomst hebben. Ten tweede kent de ontwikkeling van C. elegans een klein aantal celtype-beslissingen die willekeurig zijn. Dit maakt *C. elegans* ook een ideaal modelsysteem om te onderzoeken hoe tijdens deze stochastic celtype-beslissingen kleine en continue fluctuaties worden omgezet in een discrete celtype-beslissing die de gehele cel beïnvloedt. In dit proefschrift proberen wij deze vraag te beantwoorden door een specifieke stochastische celtype-beslissing te onderzoeken, de zogenaamde AC/VU beslissing. Als een essentiële vereiste voor dit soort onderzoek, hebben wij een nieuwe 'time-lapse' microscopietechniek ontwikkelt, die het mogelijk maakt om de volledige post-embryonale ontwikkeling van C. elegans te kunnen volgen in meerdere dieren tegelijkertijd, met hoge temporale resolutie en met single-cel resolutie, iets wat tot nu toe niet mogelijk was.

In Hoofdstuk 2 geef ik een gedetailleerde beschrijving van onze nieuwe time-lapse microscopietechniek, die gebaseerd is op (i) het vastzetten van C. elegans larven in gemicrofabriceerde kamertjes die voldoende voedsel bevatten om de hele ontwikkeling te doorlopen en genoeg ruimte om vrijelijk te kunnen bewegen, (ii) een microscopieopstelling die geoptimaliseerd is voor snelle beeldopname en (iii) beeldanalyse-technieken om de dynamica van het ontwikkelingsproces op het niveau van zowel het gehele organisme als op het niveau van enkele cellen uit de microscopiedata te distilleren. Ik beschrijf eerst in detail het ontwerp en de protocollen die gebruikt zijn voor de microfabricage van de kamertjes. Vervolgens beschrijf ik het ontwerp en de prestaties van de microscopieopstelling. Tenslotte laat

ik zien dat *C. elegans* larven zich normaal ontwikkelen in onze gemicrofabriceerde kamertjes. Specifiek heb ik de ontwikkeling gekarakteriseerd van meerdere larven, die groeiden in kamertje van verschillende afmetingen, door de drie kenmerken van de voortgang van de ontwikkelings te kwantificeren, namelijk de groeisnelheid, lichaamslengte en duur van de opeenvolgende larvale stadia. Wij laten zien dat deze meting aan groei van *C. elegans* een startpunt kunnen vormen voor toekomstig onderzoek naar het effect van de beschikbaarheid van voedsel en van dieet op ontwikkeling.

In Hoofdstuk 3 beproef ik de geschiktheid van onze microscopieopstelling om de dynamica van enkele cellen te volgen in dieren die zich ontwikkelen in de gemicrofabriceerde kamertjes. In het bijzonder heb ik een stamboom-analyse uitgevoerd van de celdelingen van de zogenaamde 'zoom-cellen', een modelsysteem voor stamcel-achtig gedrag, in meerdere dieren en over de gehele post-embryonale ontwikkeling. Hiervoor heb ik fluorescentie time-lapse microscopie gebruikt bij dieren waarvan de celkernen van zoom-cellen fluorescent waren gemerkt. Ten eerste, heb ik een kwantitatieve analyse uitgevoerd van de tijd van zoom-celdeling in meerdere wild-type larven. Ik heb daarbij ontdekt dat sommige zoom-cellen gemiddeld vroeger delen dan anderen, wat suggereert dat stamboom-afhankelijke signalen verantwoordelijk zijn voor de temporale regulatie van zoom-celdelingen. Vervolgens heb ik de variabiliteit in het precieze tijdstip van zoom-celdeling gemeten in dit ontwikkelingsproces dat verder een invariante uitkomst heeft. Bovendien heb ik de stamboom-analyse herhaald met mutanten waarin de zoom-cellen niet het stereotype delingspatroon volgen. In dit geval, laat ik zien dat fouten in celdelingen vaker voorkomen in specifieke zoom-celstambomen en tijdens specifieke larvale stadia, wat suggereert dat stadium- en stamboom-specifieke mechanismen verantwoordelijk zijn voor de correct uitvoering van zoom-celdelingen. In het algemeen zal de mogelijkheid om complete stamboom-analyse van celdingen in meerdere dieren uit te voeren in de toekomst kunnen worden gebruikt om de signalen en mechanismen in kaart te brengen die voor zoom-celdingen verantwoordelijk zijn.

In Hoofdstuk 4 laat ik zien dat onze microscopieopstelling in staat is de dynamica van genexpressie te kwantificeren, tot op het niveau van afzonderlijke cellen. Hiervoor heb ik de variabiliteit gemeten in de expressieniveaus van twee verschillende genen, waarvan eerder is aangetoond dat deze tijdens de ontwikkeling oscilleren. De ontwikkeling van C. elegans is onderverdeeld in vier larvale stadia, die worden onderbroken door een vervellingsproces, waarbij een nieuwe huid wordt aangemaakt en de oude huid wordt afgeworpen. De genen die tijdens de ontwikkeling oscillaties vertonen laten in het algemeen vier duidelijk te onderscheiden pieken zien, één tijdens ieder larvaal stadium. Door gebruik te maken van fluorescerentie time-lapse microscopie aan dieren die een kunstmatig signaal voor genexpressie bevatten, heb ik de oscillatiedynamica gekwantificeerd van één gen dat in het gehele lichaam tot expressie en een ander gen dat exclusief tot expressie komt in de kern van zoom-cellen. Voor beide genen heb ik gevonden dat het tijdstip waarop de expressie piekt sterk gecorreleerd is met de tijd van de dichtstbij liggende vervelling, wat suggereert

dat zowel de tijdstippen van de expressiepieken als van de vervellingen worden beïnvloedt door ruis uit een gemeenschappelijke bron. In de toekomst zal onze techniek waarschijnlijk kunnen bijdragen aan het begrijpen van de mechanismen die deze oscillaties voortbrengen.

In Hoofdstuk 5 pas ik onze aanpak toe op een modelsysteem voor stochastische cel-typebeslissingen: de AC/VU beslissing. Tijdens de AC/VU beslissing worden twee cellen, die α cellen worden genoemd, geboren als identieke cellen, maar differentiëert één in een *anchor cel* (AC) en de andere in een *ventral uterine* (VU) cel. Opvallend genoeg is de uitkomst van dit beslissingsproces variabel, in de zin dat iedere α cel een gelijke kans heeft om het AC- of VU-type aan te nemen. De hypothese is dat dit beslissingsproces wordt gedreven door initiële fluctuaties op moleculair niveau, wat de AC/VU beslissing een ideaal modelsysteem maakt om te bestuderen hoe continue fluctuaties worden omgezet in een discrete celtype beslissing. Ook al zijn de moleculaire mechanismen die aan dit systeem ten grondslag liggen reeds uitvoerig bestudeerd, door gebruik te maken van onze time-lapse microscopietechniek kunnen wij nu voor het eerst ook de dynamica van dit proces volgen. Om die reden maakt onze nieuwe aanpak het mogelijk om significante nieuwe inzichten te verkrijgen in de mechanismen die ten grondslag liggen aan de AC/VU beslissing. In dit hoofdstuk pogen wij op te helderen welke ruisbronnen verantwoordelijk zijn voor de bepaling van het uiteindelijke celtype. Wij onderzochten met name twee potentiële ruisbronnen: de volgorde waarin de α cellen worden geboren en de stochastische expressie van *lag-2*, één van voornaamste componenten van het onderliggende genregulatienetwerk. Ten eerste, hebben wij de variabiliteit bestudeerd in de precieze tijd waarop de α cellen worden geboren. Wij bevestigen een eerdere observatie dat de geboortevolgorde sterk gecorreleerd is met de uitkomst van het proces, in de zin dat de α cel die als tweede wordt geboren een grotere kans heeft om het AC-type aan te nemen. Echter, wij vonden ook dat als de α cellen op ongeveer gelijke tijden worden geboren, de eerstgeboren cel soms het AC-type aanneemt. Dit betekent dat aanvullende ruisbronnen belangrijk worden wanneer de α cellen in de tijd dicht op elkaar geboren worden. Wij onderzochten of de stochastische expressie van *lag-2* die wij waarnemen voor de geboorte van de α cellen, d.w.z. in hun moedercellen, deze extra bron van ruis zou kunnen zijn en hiermee de beslissing kan sturen wanneer de α cellen op gelijke tijden worden geboren. Echter, wij vonden dat dit niet het geval was. Hiermee, blijft de identiteit van de aanvullende ruisbronnen een open vraag blijft. In de toekomst zullen wij onze techniek gebruiken om de dynamica van de AC/VU beslissing verder op te helderen met het doel de aanvullende ruisbronnen te identificeren.

Acknowledgments

Here we are, at the most important part of any PhD thesis, and by far the most read Chapter. If you are reading this section of the thesis, it means that your contribution was essential for me to arrive at this point in my life. I could not be here today defending this work without your support.

First of all, I would like to thank the person that made this project happen and that believed I could contribute significantly to it: Jeroen. I am sure it was a leap of faith for you to hire a theoretical physicists that never entered a lab, never used a pipette before, and never performed microscopy experiments, to work on a purely experimental and biological project. I am glad you chose to trust me, and I am deeply grateful for all the patience you had and all the skills you taught me in this four years. One lesson above all: "Always show your enthusiasm: nobody else will ever be more enthusiastic about your research than you are". And indeed you give the best example of that every day, by turning several lunch topics into *interesting developmental biology questions*, including but not limited to i) how robust is the temporal regulation of the defecation cycle in *C. elegans*? ii) do the sizes of all the peripheral appendices in the human body correlate with each other? iii) are water bears cuter than dumpy worms? iv) can we outsource the manual data analysis of time-lapse images to non scientific people? In other words, can we turn our relatives into slaves? Thank you for these four years, I will remember them as a great learning experience!

Next, I would like to thank all the Quantitative Developmental Biology group. Simone, I am grateful I could work on this project with you, and face together all the ups and downs. I wish you all the best for your next steps and I hope we will keep in touch! Olga, thanks for being a great colleague and a close friend. Keep your enthusiasm for traveling and exploring! Who knows, maybe at some point we will arrange another awesome trip, even though I should go with "people of my age" :). Thanks Rayan for your cheerful mood! And remember: should you have any Python-related question, ask your Python mentor, not random PhD students (=Mario). Yvonne, your work is invaluable and I admire the efforts you put in it. I know I was not the perfect lab user, but I swear that my lab-coat has been used sometimes. Guizela, I am deeply impressed by all the achievements you have reached in these

years, first during your Master project and now on this challenging organoids project. Thanks for all the useful scientific inputs you had. Thanks also to all the other members of the group, Jason, Joleen and Jessica, and to the former members Kim and Eleonora. Your inputs and scientific discussions have significantly contributed to the work described in this thesis. May the worms and the organoids live long!

There are two colleagues, friends and trusted persons that accompanied me step by step through the final phase of my PhD: my great paranymphs. Mario, we had so much fun together that I don't even know where to start from, and indeed I won't mention anything specific. Instead, I am looking forward to return the favor by sharing many of these memories during your defense party and make fun of you in public :D. Thank you for being a true friend, I hope we will keep in touch! And I hope you will have the brilliant scientific career you deserve. Giulia, during this last year we lived together you have been my sister (often), my mom (sometimes) and my daughter (rarely). In one word, my family. Thank you for the random conversations, for the philosophical ones, for the late alcoholic nights, for the surprise party....thank you for everything! I wish you and Judith a wonderful future together! Wherever I will end up next, my home will always be open for you two. Just remember to pair your socks please <3

Thanks to the legendary office 0.08, a refuge for whoever in AMOLF wanted to have a break from the heavy working routines. Tomek, even though we did not overlap much, I had enough time to appreciate your encyclopedic knowledge. Jeanette, also known as "the Dude", thank you for being so spontaneous and full of energy. You were the boss of the office, without any doubt. Celine, we spent most of the time together in the office. Thanks for putting up with me in my bad days, especially when I was fighting with my code and screaming in italian at the screen, and thanks for making the office a welcoming and warm environment. And of course for supporting my last fight: to quit smoking! I leave knowing that office 0.08 is in good hands. Even if for a short time, Sebastian has been in office 0.08 too. Thank you for the "original" discussions and research ideas. It was a honor being your paranymphs. Yao, your calm mood greatly benefits the productivity of our office, so it's also thank to you that I completed my PhD thesis! Finally, the new member of the office, Jessica, I am sure you will enjoy the atmosphere in 0.08 and AMOLF.

There are so many more people that made and still make AMOLF, Amsterdam and even the Netherlands my new "home". Sara, we started this adventure together and I wish you all the best for your future. Alessandro "il patato", always willing to listen, share productive opinions and help. Thanks for the karaoke and dancing nights! Giorgos, it was great spending time with you in Patagonia, and even more awesome to be your paranymph! I wish you a successful scientific career my friend! Georges, even though I will never reach your levels, I wish my age allowed me to party again as we did in the old days. Agata, thanks for your always honest opinions and for sharing the awesome polish Vodka! Good luck with your last year in San Sebast...Amsterdam. Jacopo, thanks for the small conversations over a cigarette, no matter what weather and season. Federica, thank you for always being positive

and for your cheerful mood! Mathijs, just 3 words: slow down man! And so many more current and former AMOLFERS: Leonie "Quagmire", Yuval Fellaini, Lorenzo, Moritz, Marco "cicianebbia", Dr. Kai Harmen, Felicio, Bart, Michele, Martijn, Joris, Lutz, Stephan, Felipe, David, Aditya, Maga, Katja, Nùria, Noreen, Fatemeh, Anders, Oleg, Stephen, Parisa, Tzeni, Johannes, Galja, Katharina.....you are so many!!! Thank you to all of you (and to whoever I forgot to mention here) for all the parties and all the fun time we had together! Oh yes, thanks for the great scientific discussion too.

Four and a half years ago, when I started my PhD in Jeroen's group, I was one of the few Italians at AMOLF, definitely the only Italian in the bio groups. Nowadays, approximately ~10% of AMOLF (and ARCNL) is Italian. Thanks for being an amazing community, always willing to help each other, always proud of our origins and always ready to make fun of our peculiar italian costumes (and accent). Thank you for the endless discussions on the Dutch food and weather, for always saving some space in the luggage to carry regional products whenever going back to visit your families and, most of all, for always being willing to share them!

Then there are all the people that supported me from Italy. Grazie ai miei amici di vecchia data Carlo, Ale, Ste Pario, Andre, Ste Soffie e Giada. È un onore essere vostri amici da così tanto tempo, grazie di avermi fatto sentire ancora a casa ogni volta che sono tornato in Italia! Grazie a Nadia, Romano, Matteo, Michela, Fabio e il piccolo Tommy per avermi accolto ogni volta come se non me ne fossi mai andato.

Infine, un grazie enorme ai miei genitori. Mamma e papà, grazie dell'immenso supporto che non mi avete mai fatto mancare in questi 30 anni. Senza di voi, senza i vostri consigli, le vostre ramanzine e perché no, le rare litigate furibonde, non sarei la persona che sono ora. Anche se lo so che dentro di voi io sono ancora "il mio ometto" e "il mio bambino". Per questo e per molto altro, un immenso GRAZIE!